Edge Radial Electric Field Studies Via Charge Exchange Recombination Spectroscopy on the Alcator C-Mod Tokamak

by

Rachael Marie McDermott

B. S. Physics (2003)
Saint Louis University

Submitted to the Department of Nuclear Science and Engineering
in partial fulfillment of the requirements for the degree of

Doctor of Philosophy

at the

MASSACHUSETTS INSTITUTE OF TECHNOLOGY

May 2009

Author .....
Department of Nuclear Science and Engineering
May, 28 2009

Certified by .....
Bruce Lipschultz
Senior Research Scientist
Thesis Supervisor

Certified by .....
Prof. Ian H. Hutchinson
Nuclear Science & Engineering Department Head
Thesis Reader

Accepted by .....
Prof. Jacquelyn C. Yanch
Professor of Nuclear Science & Engineering
Chair, Department Committee on Graduate Students

Edge Radial Electric Field Studies Via Charge Exchange Recombination Spectroscopy on the Alcator C-Mod Tokamak

by

Rachael Marie McDermott

Submitted to the Department of Nuclear Science and Engineering
on May, 28 2009, in partial fulfillment of the
requirements for the degree of
Doctor of Philosophy

Abstract

It is commonly accepted that **ExB** velocity shear is responsible for the suppression of edge turbulence, which reduces the losses of both energy and particles across magnetic field lines and results in the formation of edge transport barriers and high-confinement mode (H-mode) in tokamak plasmas. However, the self consistent evolution of the radial electric field profile (E_r), pedestal shape and improvement in plasma confinement is not well understood. A better understanding of pedestal physics and the interplay between E_r, turbulence suppression and pedestal formation should enable better control of edge transport and improve core confinement. A new, high-resolution, charge exchange recombination spectroscopy (CXRS) diagnostic has been installed on Alcator C-Mod to provide measurements of the B^{5+} population in the pedestal region. This diagnostic is capable of measuring the boron temperature, density, and poloidal and toroidal velocity with 3mm radial resolution and 5ms temporal resolution. These profiles, coupled with knowledge of the toroidal and poloidal magnetic fields, enable the determination of the edge radial electric field through the radial force balance equation. The new CXRS diagnostic has provided the first spatially resolved calculations of the radial electric field in the C-Mod edge and has made possible signifiant contributions to the study of pedestal physics.

Detailed measurements of the boron population have been made in a variety of plasma regimes. The measured rotation profiles connect the SOL and core measurements and are consistent with both. The CXRS boron temperature profiles are observed to agree well with the Thomson Scattering electron temperature profiles in both shape and magnitude over a wide range of collisionalities. In H-mode plasmas both the boron temperature and density profiles form clear pedestals, similar to what is observed in the electron channel. The edge toroidal rotation increases in the co-current direction at the onset of H-mode confinement and the poloidal rotation in the pedestal region increases in the electron diamagnetic direction forming a narrow peak (3-4mm) just inside of the LCFS.

In Ohmic L-mode plasmas E_r is positive near the last closed flux surface (LCFS) and becomes more negative with distance into the plasma. In H-mode plasmas E_r is

positive in the core, but forms a deep negative well, relative to its L-mode values, just inside of the LCFS. These results are qualitatively consistent with the observations made on other machines. However, the C-Mod H-mode E_r wells are unprecedented in depth (up to 300kV/m) and the narrow E_r well widths (5mm), as compared to results from other tokamaks, suggest a scaling with machine size.

The measured E_r well widths have been compared to theoretical scalings for the edge pedestal and no significant correlation was observed with any of the predictions. In fact, very little variation of the E_r well width is observed in general. However, the depth of the E_r well, or alternatively the magnitude of the E_r shear (constant width), shows a strong correlation with improved plasma energy confinement. It also correlates well with the edge electron temperature and pressure pedestal heights (and gradients). It is not, however, very sensitive to variation in the edge electron density pedestal height. These results are an indication that the energy and particle transport have different relationships to E_r, with energy transport more directly linked. The radial electric field results from ELM-free H-mode and I-mode plasmas support this interpretation.

Thesis Supervisor: Bruce Lipschultz
Title: Senior Research Scientist

Thesis Supervisor: Prof. Ian H. Hutchinson
Title: Nuclear Science & Engineering Department Head

Acknowledgments

This thesis is the culmination of my years in graduate school, working as a research assistant on the Alcator C-Mod tokamak at the Plasma Science Fusion Center at MIT. I have enjoyed thoroughly my time at C-Mod and have benefitted immensely, both personally and professionally, from my interactions with the researchers and staff at the PSFC, the professors in the Nuclear Science and Engineering department, and my fellow graduate students. I am especially indebted to my advisor, Bruce Lipschultz, for his incredible patience, hard work, and dedication. He has been a constant source of encouragement and support and I am continually awed by his generosity with both his time and his knowledge. Further, I am forever grateful for the many lessons he has bestowed on me over the years. He has taught me nearly all I know about being an experimentalist as well as to appreciate good chocolate and good beer - though in this last I am still a novice. I have been very fortunate to be his student, and even more so to be his friend.

I would also like to extend my appreciation to the researchers and professors who have contributed to this research and to my education through their time, intellect, and their teachings: Doctors Paul Bonoli, Peter Catto, Darin Ernst, Catherine Fiore, Jeffery Freidberg, Robert Granetz, Martin Greenwald, Amanda Hubbard, Jerry Hughes, Ian Hutchinson, Jim Irby, Brian LaBombard, Bruce Lipschultz, Earl Marmar, Ron Parker Miklos Porkolab, Abhay Ram, John Rice, Steve Scott, Jim Terry, Dennis Whyte, Steve Wolfe, Steve Wukitch, and Stuart Zweben.

There are a number of people who deserve special recognition for their contributions to this work. These include Alex Ince-Cushman, Jerry Hughes, Kenneth Marr, Matt Reinke, and John Rice all of whom have most generously contributed data that were used in this thesis. Also, I am indebted to Prof. Ian Hutchinson for his careful reading of this thesis and his unerring guidance over the years, to Prof. Dennis Whyte who has taught me so much and who inspires with his energy and enthusiasm, to Doctors Jerry Hughes and John Rice for their insight, interest in my work, and their friendship, to Prof. Peter Catto for the many fruitful discussions, patient

explanations, and tireless efforts to explain the nuances of theory to this poor experimentalist, and to Dr. Andrei Simakov for his help in making comparisons between experiment and theory possible. Lastly, I owe a special thank you to Kenneth Marr for his time, hard work, and many contributions to the CXRS diagnostic.

I must also thank Bob Granetz and Dexter Beals for maintaining and operating the diagnostic neutral beam. Without them this thesis would not have been possible. In addition, the ICRF group, notably Steve Wukitch and Yijun Lin deserve special recognition as do the C-Mod physics operators: Bob Granetz, Prof. Ian Hutchinson, Jim Irby, Earl Marmar, Prof. Ron Parker, Bill Rowan, Joe Snipes, and Steve Wolfe. The PSFC and Nuclear Science and Engineering department administration and staff are an amazing and dedicated group of people who have helped me tremendously. These people include: Andy Pfeifer, Bob Childs, Charles Cauley, Clare Egan, Corrine Fogg, Dave Arsenault, Dave Belloffato, Don Nelson, Dragana Zubcevic, Ed Fitzgerald, Edgar Rollins, Eric Anderson, Felix Kreisel, Frank Shefton, Gary Dekow, Heather Geddry, Henry Bergler, Henry Savelli, Jason Thomas, Jessica Coco, Joe Bosco, Josh Stillerman, Lee Keating, Mark Iverson, Mark London, Maria Silveira, Matt Fulton, Nancy Masley, Patrick Scully, Paul Lienard, Paul Rivenberg, Peter Brenton, Richard Murray, Ron Rosati, Rui Vieira, Sam Pierson, Tim Davis, Tom Fredian, Tommy Toland, Valerie Censabella, William Burke, William Byford, and William Parkin.

I would also like to acknowledge all of my fellow graduate students who have shared with me all of the triumphs and tribulations of the last six years and in so doing have made my time at C-Mod more gratifying, more memorable, and at times more bearable: Aaron Bader, Igor Bespamyatnov, Brock Bose, Istvan Ciegler, Alex Ince-Cushman, Arturo Dominguez, Eric Edlund, Jennifer Ellsworth, Marco Ferrara, Craig Gerardi, Tim Graves, Zachary Hartwig, Nathan Howard, Ishtak Karim, Jinseok Ko, Liang Lin, John Liptac, Scott Mahar, Kenneth Marr, Eugenio Ortiz, Yuri Podpaly, Matthew Reinke, Andrea Schmidt, Jason Sears, Noah Smick, Kelly Smith, Vincent Tang, Gregory Wallace, Jamie Yang and Howard Yuh. To Alex Ince-Cushman, Eugenio Ortiz, Matt Reinke, and Jamie Yang thank you for the gift of your friendship, for the years full of laughter and fun, and for always being there when I

needed you.

Finally, I would like to express my gratitude to my family. I am grateful to my parents, Jim and Judy McDermott, and my sister, Jessica, for their unconditional love and support and their wholehearted confidence in me and what I can achieve, also to my aunt, Sheila McDermott, and grandmother, Barbara McDermott, for always leaving their door open when I needed a quiet place and always sending me back with food, and especially to my grandparents, John and Alice Susko, who didn't live to see me graduate, but were always my biggest fans.

Contents

1 Introduction **19**

1.1 Alcator C-Mod Tokamak 21

1.1.1 C-Mod Diagnostics 26

1.2 Plasma Operating Regimes 28

1.2.1 EDA H-modes 28

1.2.2 Edge localized mode (ELM) free H-modes 29

1.2.3 Improved L-mode (I-modes) 31

1.3 Thesis Goals and Outline 34

2 Tokamak Edge Radial Electric Fields: Theory and Experiment **37**

2.1 Early Theories 37

2.2 ExB turbulence suppression 40

2.3 Two-Step Theories 44

2.3.1 Poloidal Spin-up Theories 45

2.3.2 Pressure Gradient Theories 49

2.4 Pedestal Structure Models 53

2.5 Neoclassical Theory 55

2.6 Experimental Results from Other Tokamaks 57

2.6.1 DIII-D 58

2.6.2 ASDEX and ASDEX Upgrade 61

2.6.3 JET 62

2.6.4 JFT-2M 63

2.6.5 Alcator C-Mod 64

3 The Edge Charge Exchange Recombination Spectroscopy Diagnostic on Alcator C-Mod **67**

3.1 CXRS as a Plasma Diagnostic 68

3.2 The C-Mod Edge CXRS Diagnostic 73

3.2.1 In-vessel Components 73

3.2.2 External Components 78

3.3 Calibrations 82

3.3.1 In-Vessel Calibrations 83

3.3.2 External Calibrations 86

3.4 The Diagnostic Neutral Beam 90

3.5 Data Analysis 99

3.5.1 The Zeeman Effect on Charge Exchange Spectra 102

3.5.2 Cross Section Effects on Charge Exchange Spectra 108

3.5.3 Uncertainties in CXRS Measurements 110

4 CXRS Measurements of Pedestal Structure and Behavior **115**

4.1 Alignment of Temperature Profiles 116

4.1.1 Position of the LCFS 122

4.2 CXRS Results in Ohmic L-mode Plasmas 124

4.3 CXRS Results in ELM-free H-mode Plasmas 129

4.4 CXRS Results in EDA H-mode Plasmas 134

4.5 CXRS Results in I-mode Plasmas 141

5 Edge Radial Electric Field Structure on Alcator C-Mod **147**

5.1 Calculation of the Radial Electric Field 148

5.2 E_r in Ohmic L-mode Plasmas 149

5.3 E_r in H-mode Plasmas 151

5.3.1 E_r in ELM-free H-modes 152

5.3.2 E_r in EDA H-Modes 156

5.4 E_r in I-mode Plasmas 160

6 Scalings of the H-mode E_r Well and Comparisons to Theory **163**

6.1 Scaling of E_r Well Width 163

6.2 Scaling of E_r Well Depth 167

6.3 Comparison to Neoclassical Theory 170

6.4 Comparison to Main Ions 173

6.5 Alignment of E_r with Edge Electron Pedestals 177

7 Summary and Directions for Future Work **181**

7.1 High Resolution Pedestal Measurements 182

7.2 Impurity Ion Pedestal Characteristics 182

7.3 Structure of the Edge Radial Electric Field and Comparisons to Theory 185

7.4 Connections to Confinement and Transport 187

List of Figures

1-1 The Alcator C-Mod Tokamak 22

1-2 Top view of the Alcator C-Mod tokamak 23

1-3 Cross-section of the Alcator C-Mod tokamak 24

1-4 EDA H-mode plasma characteristics 29

1-5 ELM-free H-mode plasma characteristics 30

1-6 I-mode plasma characteristics 32

1-7 T_e and n_e in L-, I-, and H-mode plasmas 33

2-1 Turbulence decorrelation by velocity shear 42

2-2 S-curve bifurcation diagram 51

3-1 Example layout for a CXRS diagnostic 68

3-2 In-vessel CXRS periscopes 73

3-3 Lines of sight of the beam poloidal periscope 75

3-4 Mid-plane locations of the CXRS periscope's lines of sight 76

3-5 Lines of sight of the toroidal periscope 77

3-6 CXRS spectrometer and camera 79

3-7 Internal design of the CXRS spectrometers 80

3-8 CXRS spectra imaged using multiple entrance slits 81

3-9 Inner wall calibration table 84

3-10 Brightness calibration method for the poloidal periscopes 85

3-11 Filter function calibration data 87

3-12 Fit to neon calibration lines 88

3-13 Layout of the C-Mod DNB 91

3-14 Geometry of DNB 93
3-15 Stopping cross-sections for DNB attenuation on neutrals 94
3-16 DNB attenuation by neutral gas 96
3-17 Total stopping cross-section for a hydrogen beam in a deuterium plasma 97
3-18 DNB attenuation into C-Mod plasmas 97
3-19 Effective emission rate for CX into the λ=4944.67A n=7-6 spectral line 98
3-20 Active CXRS spectra 100
3-21 Energy level splitting due to the Zeeman effect 103
3-22 Parameterization of the Zeeman splitting by polarization components 106
3-23 Geometry for cross-section effect calculation 109
3-24 Cross-section effects on C-Mod CXRS spectra 110

4-1 C-Mod CXRS velocity sign convention 116
4-2 Estimation of the T_i based on measured T_e and T_B profiles 120
4-3 Power balance determined position of LCFS in an EDA H-mode . . . 124
4-4 Ohmic BVI toroidal velocity profiles 125
4-5 Ohmic B^{5+} poloidal velocity profiles 127
4-6 Ohmic L-mode boron temperature and density profiles 128
4-7 CXRS profiles in reversed field, LSN, ELM-free H-mode 130
4-8 CXRS and TS temperature profiles in an ELM-free H-mode 131
4-9 Inverse gradient scale lengths in ELM-free H-modes 132
4-10 Pedestal evolution in forward field, USN, ELM-free H-mode 133
4-11 CXRS profiles in an EDA H-mode plasma 135
4-12 Pedestal evolution during L-H transitions 138
4-13 Toroidal rotation versus plasma stored energy 139
4-14 Pedestal poloidal velocity versus pedestal T_e 140
4-15 T_e and T_B profiles in EDA H-modes 140
4-16 CXRS results in I-mode plasmas 142
4-17 Pedestal evolution in L-I and I-H transitions 144
4-18 Toroidal velocity precursor to I-H transitions 145

4-19 Radial profiles of toroidal velocity precursor to I-H transitions 146

5-1 E_r profiles in Ohmic L-mode discharges 150
5-2 Evolution of E_r and E_r shear in ELM-free H-modes 153
5-3 Contributions to E_r in ELM-free H-modes 155
5-4 E_r and E_r shear in EDA H-modes 157
5-5 Contributions to E_r in EDA H-modes 158
5-6 Full plasma E_r profile 160
5-7 E_r and E_r shear in I-mode plasmas 161

6-1 Scaling of E_r well width with theoretical predictions 165
6-2 Width of H-mode E_r well as a function of machine size 167
6-3 Depth of E_r well versus plasma confinement (H89) 169
6-4 Depth of the E_r well versus edge pedestal parameters 171
6-5 Plasma collisionality in different plasma regimes 173
6-6 Comparison of EDA E_r profile to neoclassical theory 174
6-7 Main ion diamagnetic contribution to E_r 176
6-8 Main ion velocity perpendicular to the total magnetic field 176
6-9 Radial alignment of E_r profiles with electron pedestal parameters . . 179

List of Tables

2.1 Theoretical scalings of E_r well width 65

3.1 Neutralization Efficiency for Beam Energy Components 92

3.2 Beam energy component contributions to CXRS emission 99

Chapter 1

Introduction

Over the last quarter century the fusion community has made significant progress toward making magnetic confinement fusion a physically and economically viable energy resource. Advances in physics understanding and reactor engineering have enabled the design of ITER; a fusion experiment which will demonstrate the feasibility of commercial fusion energy by creating the first self-sustaining fusion plasma on earth. In order to reach its operational goals, it is thought that ITER must operate in a plasma regime called high confinement mode, or H-mode, which is characterized by a factor of two improvement in plasma energy confinement over the more easily obtained low confinement mode, or L-mode. However, despite intensive study by both the theoretical and experimental fusion communities, the actual mechanism by which the transition from L-mode to H-mode takes place remains unclear.

The onset of an H-mode is characterized by a sharp decrease in edge fluctuations and the formation of edge transport barriers (pedestals) in both the ion and electron temperature and density profiles. These barriers lead to significant increases in core confinement as a result of temperature and density profile stiffness. It is commonly accepted that **ExB** velocity shear is responsible for the suppression of edge turbulence, which reduces the losses of both energy and particles across magnetic field lines and results in the formation of the edge transport barriers and H-mode confinement[1, 2]. However, the self consistent evolution of the radial electric field profile, pedestal shape, and improvement in plasma confinement are not well understood.

Experimentally, it is clear that core plasma confinement is directly connected to, if not controlled by, the edge pedestal[3, 4, 5]. Plasma rotation and velocity shear are known to play an important role in the transition from L-mode to H-mode with the plasma spin up at the transition propagating from the plasma edge to the core[6, 7]. The source of this seemingly spontaneous rotation is unknown, though it may be connected to scrape off layer (SOL) flows, which couple across the last closed flux surface (LCFS)[8]. This spontaneous edge rotation may be responsible for the formation of shear in the radial electric field profile, thus initiating the suppression of turbulence and enabling the transition to H-mode. Measurements of flows and radial electric field behavior in the pedestal region may help answer these questions and provide the missing link between the SOL and core observations. A better understanding of the role the radial electric field plays in pedestal physics should enable better control of edge transport and improve core plasma confinement.

On Alcator C-Mod a new pedestal charge exchange recombination spectroscopy (CXRS) diagnostic has been installed, which provides measurements of pedestal parameters (flows, temperatures, densities) and radial electric field structure and behavior with millimeter radial resolution and 5 millisecond temporal resolution. The radial electric field is determined through the radial force balance equation

$$E_r = \frac{1}{n_i Z_i e}\frac{\partial p_i}{\partial r} - v_{\theta,i}B_\phi + v_{\phi,i}B_\theta \tag{1.1}$$

where the subscript, i denotes species, Z, n, and p are the charge, density, and pressure, $v_{\theta,\phi}$ and $B_{\theta,\phi}$ are velocity and magnetic field in the poloidal and toroidal directions. CXRS measurements, coupled with knowledge of the magnetic fields, provide all of the information necessary to determine E_r from equation 1.1. Details of the new CXRS system will be given in chapter 3.

These C-Mod pedestal E_r measurements are made in a unique and relevant parameter regime and can thus bring new information and understanding to the fusion community. Most C-Mod discharges are free from any externally applied torque and operate at ITER-like magnetic fields (~5T) and plasma pressures (1MPa). Ad-

ditionally, at high density, the C-Mod pedestal has ITER-like opacity to neutrals and thermally equilibrated electrons and ions, conditions currently unique to C-Mod. This thesis employs the results from the new CXRS system to probe the relationships between the radial electric field, L-H transitions and plasma confinement.

1.1 Alcator C-Mod Tokamak

Alcator C-Mod is a high-field, compact toroidal device, located at the Plasma Science Fusion Center (PSFC) at MIT. C-Mod has been at the forefront of the US fusion research program for over a decade and is uniquely suited for studying ITER relevant plasmas due to the similarities between the two devices. C-Mod, shown in Fig. 1-1 is a relatively small device compared to other tokamaks. It has a major radius of 0.67m and minor radius of 0.22m. Although ITER will be nine times larger than C-Mod they share many similar characteristics such as toroidal magnetic field strength, plasma density and pressure, aspect ratio, plasma shape, and divertor geometry.

C-Mod typically runs with core densities between 1 and $5\times10^{20}m^{-3}$ and with plasma pressures up to 1.8 atm. Core plasma temperatures are of order a few keV and the plasma current is typically between 0.6 and 1.2 MA; although plasma currents as low as 0.4MA and as high as 2MA can be achieved. The standard operating magnetic field is 5.4T at the magnetic axis, but C-Mod is capable of operating anywhere between 2 and 8T. The heating scheme on C-Mod is ion cyclotron resonant frequency (ICRF) heating, typically at 78 to 80 MHz. This frequency is resonant with the cyclotron frequency of the ions at a magnetic field of 5.3T, which places the bulk of the input power on axis for a standard C-Mod shot. It is also possible to provide adequate heating for alternate magnetic fields strengths by switching to alternate frequencies such as 50 or 70MHz.

All of the data presented in this thesis are from the C-Mod 2007 and 2008 run campaigns. During these campaigns there were two dipole ICRF antennas at D and E port, and one four strap antenna at J-port, see Fig. 1-2 for port geometry. These antennae together were capable of coupling up to 6MW of power into the plasma. In

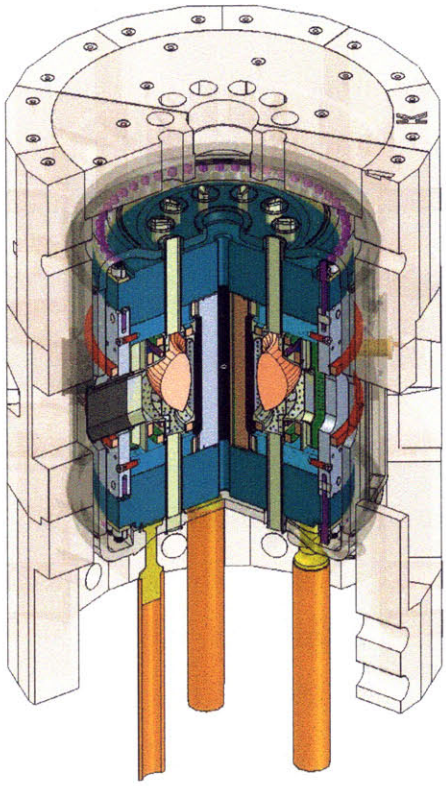

Figure 1-1: The Alcator C-Mod tokamak

addition to the ICRF antennae there was also a single lower hybrid (LH) current drive antenna installed at C-port, which coupled up to 1MW of power into the plasma at 4.6GHZ. Neither of these systems act as a particle or momentum source.

There are no neutral heating beams on C-Mod. Instead there is a diagnostic neutral beam (DNB) located at F-port. The beam has a predominantly radial trajectory with only a slight 6.4 degree toroidal angle and is horizontally injected into the plasma at mid-plane (Z=0), see Fig. 1-3. It is capable of producing a 7A, 50keV, hydrogen beam for a total of 1.5s, either steady or modulated. Due to the low beam current, radial injection angle and the high level of beam attenuation into C-Mod's high density plasmas, the DNB is not a significant source of either momentum or particles. More detailed information on the DNB is provided in 3.

In Fig. 1-3 the horizontal cross-section of the Alcator C-Mod tokamak is displayed with a typical C-Mod plasma shape outlined in red. C-Mod is a diverted tokamak; it is designed to operate with a null or x-point in its magnetic field topology. The

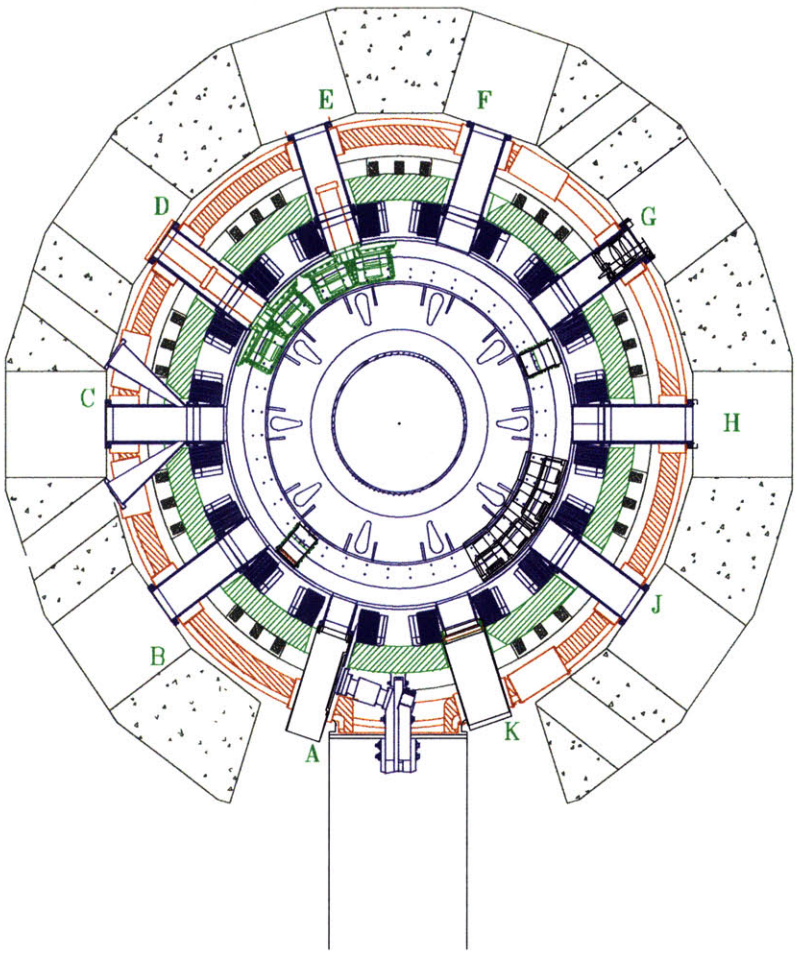

Figure 1-2: Top view of the Alcator C-Mod tokamak

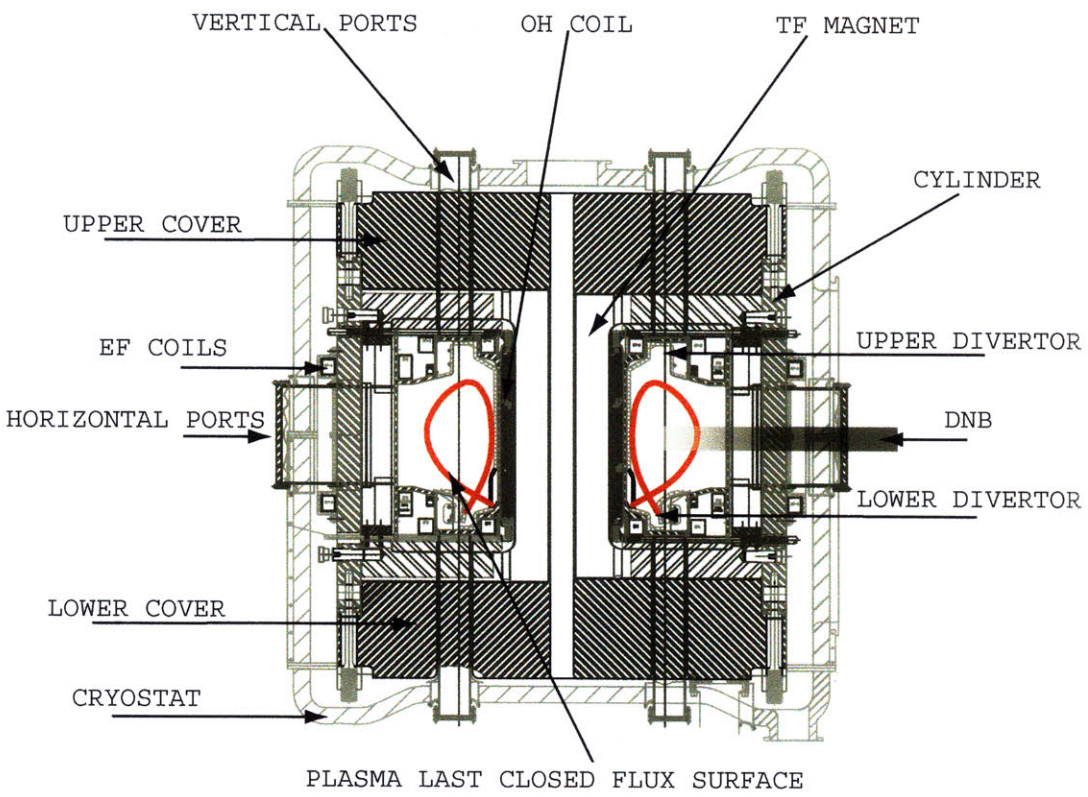

Figure 1-3: Horizontal cross-section of the Alcator C-Mod tokamak showing the size and positions of the tokamak support structure and geometry. A typical plasma shape is shown in red.

magnetic flux surface with the null point is referred to as the last closed flux surface (LCFS) or separatrix. Magnetic surfaces inside of the LCFS are "closed", meaning they end on themselves, and surfaces outside the LCFS are "open", meaning they terminate on walls or other plasma facing components. The region of plasma that exists on open field lines, outside the LCFS, is referred to as the scrape off layer (SOL). To create magnetic topologies that have a null point (or null points), the plasma is shaped using EF coils see figure 1-3, resulting in an elongated 'D' shaped plasma rather than a circular cross-section plasma.

When the null point in the magnetic field is positioned by the lower divertor the plasma shape is referred to as lower single null (LSN). When the null point is positioned by the upper divertor, the plasma shape is referred to as upper single null (USN), and when there are two null points in the field, one by each divertor, then the plasma shape is said to be in double null (DN). The divertors are designed to place

the strike points of the LCFS and open magnetic flux surfaces, on surfaces that can handle high heat fluxes and are positioned in such a way as to minimize the amount of impurities that work their way into the plasma. On C-Mod most of the plasma facing components, located at the inner wall, limiters, and the divertor plates, are covered primarily in molybdenum tiles, which have a melting point of 2617 degrees celsius. C-Mod plasmas can also be run in a limiter configuration, limited typically on the inner-wall, not making use of either the upper or lower divertor. In fact, the start up shape for all C-Mod plasmas is inner-wall limited.

Often the magnetic field topology of a discharge is referenced by the direction of particle drifts in the plasma, such as the $B \times \nabla B$ drift direction, rather than by the physical location of the X-point, as in USN or LSN. The reason for this is that the drift direction provides more information about the magnetic field than the magnetic topology. In the presence of a magnetic field that has a gradient perpendicular to the field direction, as is the case in a tokamak, a charged particle feels a force that is perpendicular to both the field and the gradient. This particle velocity as a result of this force is given by

$$\mathbf{v}_{B\times\nabla B} = \frac{1}{2}\frac{m_j}{e_j B}\frac{\mathbf{B}\times\nabla B}{B^2}{v_\perp}^2, \tag{1.2}$$

where B is the magnetic field, m_j is the mass and e_j the charge for particle j, and $\mathrm{v}_\perp$ is the perpendicular velocity of the particle. Note, that the $B \times \nabla B$ drift direction is different for ions and electrons. Experimentally, it has been found that discharges with the X-point in the direction of the ion $B \times \nabla B$ drift require less input power to initiate an L-H transition than do discharges with the X-point in the direction of the electron $B \times \nabla B$ drift. For this reason, the ion drift direction is considered the "favorable" $B \times \nabla B$ direction and the electron the "unfavorable". In standard C-Mod discharges (forward field) the magnetic field is in the clockwise direction from a top down view of the machine. Thus when operating in forward field, LSN discharges are in the favorable $B \times \nabla B$ direction and USN unfavorable. This switches when the direction of the magnetic field is reversed (the plasma current direction is always

reversed with the toroidal field in C-Mod).

There are two other plasma particle drifts that are relevant to this thesis, the diamagnetic drift and the **ExB** drift. The diamagnetic drift is the particle motion that results from the force of the plasma pressure and is given by

$$\mathbf{v}_{\nabla p} = \frac{\mathbf{B} \times \nabla p}{e_j n B^2}. \tag{1.3}$$

Here, B is the magnetic field, e_j is the charge on the particle and p and n are the plasma pressure and density. Again, note that the drift is dependent upon the sign of the charge, meaning the ion and electron directions are opposite. These directions also switch when the magnetic field is reversed. In forward field, on the low field side of the tokamak, the electron diamagnetic direction is vertically upward and the ion diamagnetic direction is downward. The diamagnetic directions are often used when describing the direction of observed flows in a plasma. Lastly, a charged particle in a magnetic field will feel an additional force when there exists an electric field (E) perpendicular to B. This force results in the **ExB** velocity drift and it is the shear in this quantity that is believed to be responsible for breaking up turbulent eddies and improving plasma confinement[2, 9]. Therefore, this drift is very important to this thesis, and a detailed discussion of its relationship to turbulence and plasma confinement will be given in chapter 2. The drift is given by

$$\mathbf{v}_{ExB} = \frac{\mathbf{E} \times \mathbf{B}}{B^2} \tag{1.4}$$

and is charge independent.

1.1.1 C-Mod Diagnostics

C-Mod has a fairly comprehensive suite of plasma diagnostics[10], only a subset of which are relevant to this thesis. A summary of the diagnostic systems, the data from which was used in this work, is given here. The main diagnostic tools for measuring the electron density and temperature in the plasma are the Thomson scattering (TS) systems of which there are two: an edge system covering from r/a of 0.8 to r/a of 1.05

and a core system, which covers from r/a of 0 to 0.8. The edge TS system provides T_e and n_e profiles covering the pedestal region with millimeter spatial resolution and a time resolution of 20ms. For more information on the C-Mod TS systems one should refer to reference[11]. The average Z_{eff} in the plasma is obtained through a comparison of the visible bremsstrahlung emission ($\propto n_e^2 Z_{eff}/\sqrt{T_e}$) with Thomson scattering electron density and temperature information.

Edge neutral pressures are measured at several toroidal points throughout the tokamak using standard pressure gauges. These diagnostics provide data on a 5-10 milli-second time scale and have an accuracy 0.1mtorr. Magnetics measurements, employing voltage loops, flux loops, and Rogowski coils enable the reconstruction of the magnetic equilibrium through the EFIT code [12]. EFIT uses the data to find a best fit solution to the Grad-Shafranov equation for the C-Mod tokamak geometry. The outputs of the EFIT code include magnetic flux surfaces on an R-z grid, the poloidal magnetic field, plasma current and q profiles. EFIT is run for every shot on a standard 20ms time base. However, if desired, it can be run on a faster time base. It is also possible to run kinetic EFIT analysis of plasma discharges, which uses the measured plasma density and temperature profiles to calculate a self-consistent magnetic equilibrium as a function of time. However, this is difficult to do and is not performed routinely for C-Mod discharges.

In addition to the CXRS systems, impurity ion temperature, density and velocity measurements are also provided by core viewing soft X-ray diagnostics, such as Hirex Jr.[13] and Hirex SR[14], which diagnose mainly argon and molybdenum. These profiles typically have a temporal resolution of 20ms, and extend from the plasma core out to r/a between 0.7 and 0.85 depending on signal level. C-Mod also has a number of fluctuations diagnostics including reflectometry, phase contrast imaging (PCI), D-alpha, gas puff imaging (GPI) and magnetics. These systems together monitor the magnetic and density turbulence fluctuations in both the core, edge, and SOL regions of the plasma. More information on these systems can be found in reference [10].

1.2 Plasma Operating Regimes

There are several distinct operational regimes that are observed on the Alcator C-Mod tokamak. These include the L-mode and a number of different types of high confinement regimes. Of these regimes, there are two types of H-modes that are routinely run on C-Mod, the EDA (enhanced D-alpha) H-mode [15, 16] and the ELM (edge localized mode) free H-mode[5]. It is also possible to run ELMy H-modes on C-Mod. However, no data from this type of discharge will be used in this thesis and so the details of this operating regime will not be discussed. In addition to H-modes a new operational regime, the improved L-mode (I-mode), has recently been developed on C-Mod. The I-mode has H-mode like energy confinement coupled with L-mode like particle confinement and will be described in detail in this thesis.

1.2.1 EDA H-modes

Enhanced D-alpha (EDA) H-modes are one of the most common types of H-modes run on C-Mod. They are quiescent H-modes without ELMs, characterized by increased particle transport through the edge relative to ELM-free H-modes. This increase in edge transport can be observed through the increase in D_α emission during the H-mode period as shown in Fig. 1-4a. The enhanced particle transport is associated with a quasi-coherent mode (QCM) observed on the density and magnetics fluctuations at frequencies between 80 and 150kHz. The QCM develops shortly after the formation of the edge pedestals, is localized to the electron density pedestal and is likely the result of a resistive ballooning instability. It is believed to be the density pedestal release mechanism that prevents impurities from accumulating in the core and increasing the radiated power. The increased particle transport allows for steady state H-mode operation with constant radiated power, density, temperature, and confinement. Fig. 1-4 shows the steady state nature of these parameters for a typical EDA H-mode. The QCM, and thus EDA H-modes, are only observed in high collisionality plasmas, typically $\nu^* > 1$ at the top of the pedestal, where ν^* is calculated according to

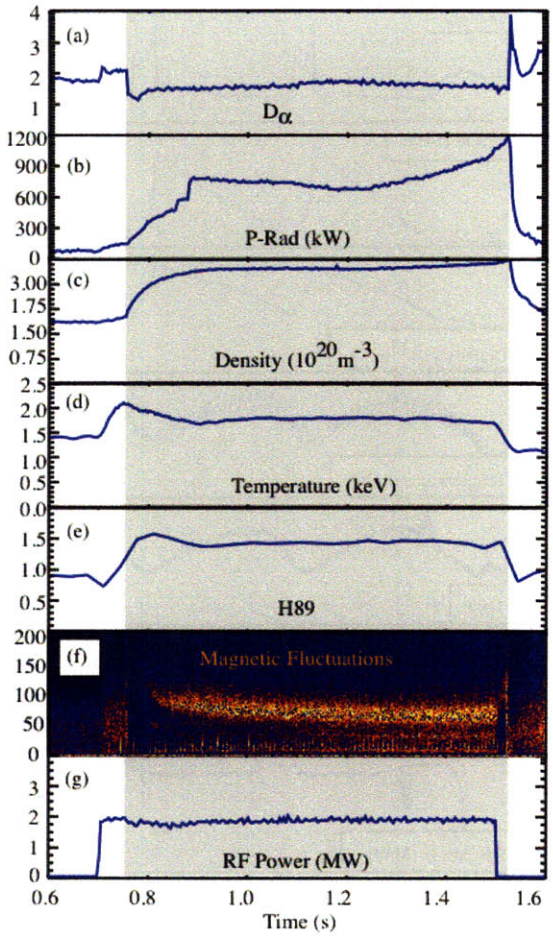

Figure 1-4: Characteristics of a C-Mod EDA H-mode (Shot=1080321020) (a)D_α (b) radiated power (c) line averaged density (d) electron temperature (e) plasma confinement factor H89, (f) magnetic fluctuations, (g) input ICRF power

$$\nu^* = \frac{qR\nu_{ei}}{\epsilon^{\frac{3}{2}} v_{th,e}}. \tag{1.5}$$

Here, q is the local safety factor, R the major radius, ν_{ei} is the electron ion collision frequency, ϵ is the inverse aspect ratio, and $v_{th,e}$ is electron thermal velocity.

1.2.2 Edge localized mode (ELM) free H-modes

ELM-free H-modes are inherently transient, characterized by a strong particle transport barrier. This barrier results in impurity accumulation during the H-mode, which eventually causes its radiative collapse. Both the plasma and impurity density increase monotonically during ELM-free H-modes, while T_e, T_i, and energy confine-

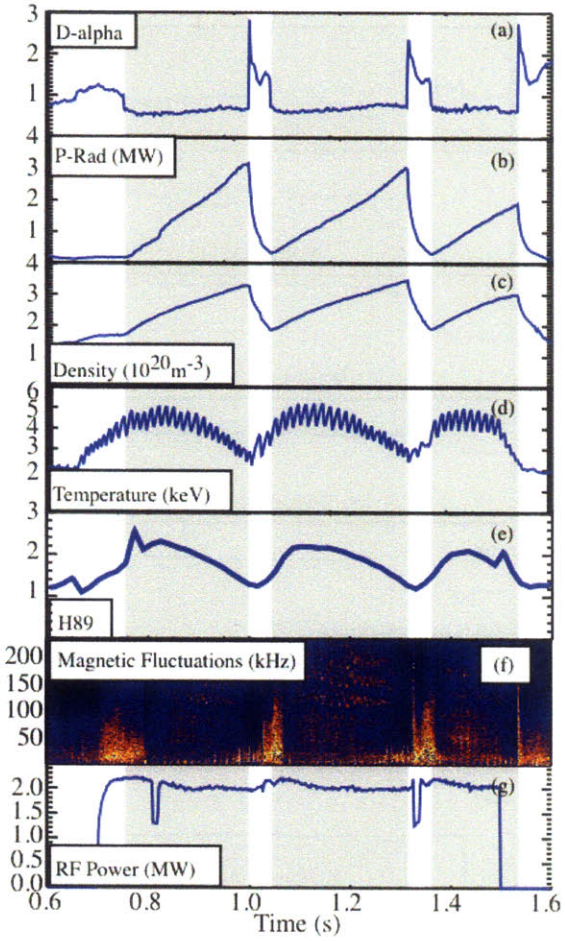

Figure 1-5: Characteristics of a C-Mod ELM-free H-mode (Shot = 1070726015) (a)D_α (b) radiated power (c) line averaged density (d) electron temperature (e) plasma confinement factor H89, (f) magnetic fluctuations, (g) input ICRF power

ment peak early and then degrade as a result of the increasing radiated power. These characteristics are shown in Fig. 1-5. Edge L-mode density and magnetic fluctuations are sharply suppressed at the onset of ELM-free H-modes, while the residual fluctuations during the H-mode are largely incoherent [Fig. 1-5(f)]. The best ELM-free H-modes can have energy confinement in the beginning of the H-mode up to 30% higher than the best EDA H-modes and much higher particle confinement. However, as the radiated power approaches the input power, the plasma energy confinement and temperature pedestal both decline[17, 18].

1.2.3 Improved L-mode (I-modes)

Standard L- to H- transitions on Alcator C-Mod occur on a sub-millisecond time scale. This is too fast for the current CXRS system to capture any of the transition dynamics. However, C-Mod discharges with the X-point in the unfavorable ion $B \times \nabla B$ drift direction with input power just below the H-mode threshold can exhibit slower evolution prior to L-H transitions. The slow evolution enables insight into the H-mode physics through examination of the plasma evolution preceding the transition. The slowly evolving plasma phase is not a new phenomenon, it has been observed previously on both C-Mod[3, 19] and ASDEX Upgrade[20], but always as a transient event. Recent experiments on C-Mod have developed this transient period into an operational regime that can persist for many energy confinement times[21].

This regime is characterized by an L-mode-like edge particle barrier, but an H-mode-like energy barrier and has been termed an 'improved L-mode', or 'I-mode'. In I-mode the plasma density increases modestly coincident with the application of ICRF power, but does not increase further or approach its H-mode values. The plasma temperature, however, approaches and maintains close to its full H-mode value during the I-mode period. These features can be seen in the core plasma traces shown in Fig. 1-6. The key differences between L-, I-, and H-mode plasmas are illustrated in Fig. 1-7, which displays the edge electron temperature and density pedestals in these regimes. Here, the I-mode electron temperature pedestal approaches a full H-mode pedestal, while the electron density pedestal remains significantly closer to its L-mode levels. Similar behavior is observed in the corresponding B^{5+} temperature and density pedestal profiles.

The I-mode evolves smoothly from L-mode plasmas after the application of ICRF heating. There is no apparent bifurcation or clear transition point. Although the I-mode appears to be an intermediate state between L-mode and H-mode, the transition from I-mode to H-mode remains an apparent bifurcation, only after which an H-mode density pedestal forms. During I-mode, H-mode like plasma confinement (H98 = 0.8) is maintained concomitant with H-mode like plasma temperatures, Fig. 1-6(e).

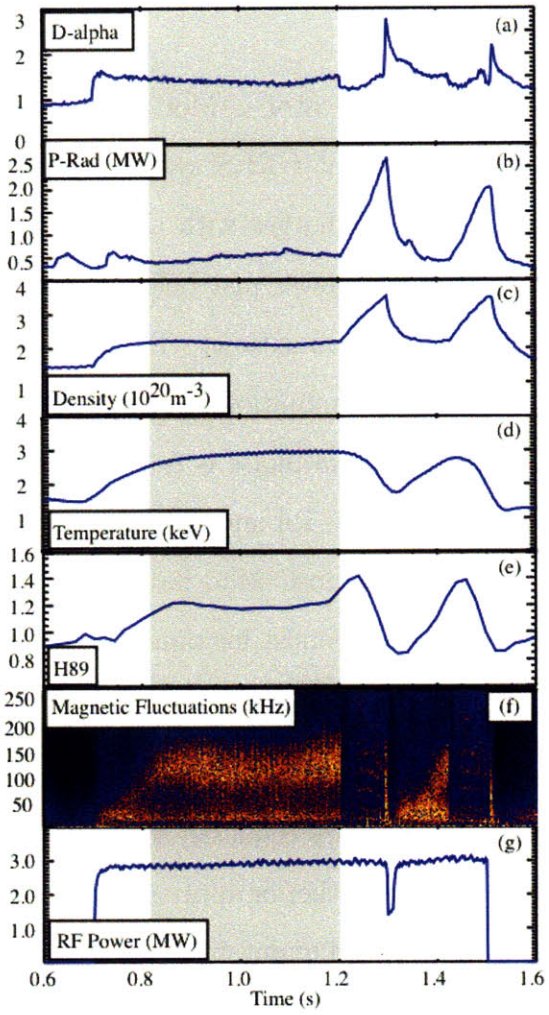

Figure 1-6: Characteristics of a C-Mod I-mode plasma (Shot = 1080416021). The grey highlighted region indicates the I-mode portion of the discharge. (a)D_α (b) radiated power (c) line averaged density (d) plasma temperature (e) plasma confinement factor H98, (f) magnetic fluctuations, (g) input ICRF power

The improved confinement can be maintained in steady state. L-mode like particle confinement prevents the buildup of impurities and consequently the accompanying increase in radiated power. The steady state operation in I-mode is associated with an edge turbulence mode observed on the density and magnetic fluctuations with a frequency around 100kHz as shown in Fig. 1-6 (f). The mode appears to be similar to the QCM observed in EDA H-mode operation, but exists at much lower collisionality ($\nu^* < 1$) and is spread over a wider frequency range.

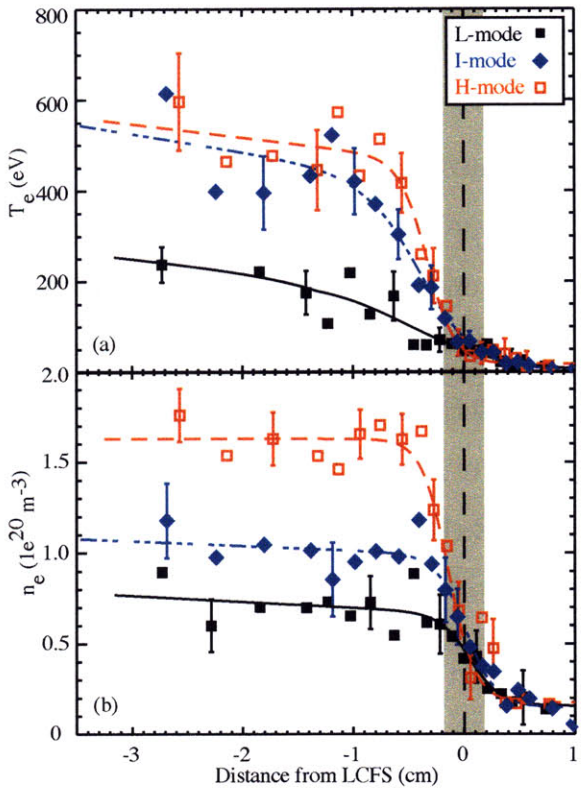

Figure 1-7: Comparison of the edge electron temperature (a) and density (b) profiles between L-mode, I-mode and H-mode.

1.3 Thesis Goals and Outline

The objective of this thesis is to acquire a better understanding of the connections between E_r, E_r shear and plasma particle and energy confinement. This information will lend itself to determining the physics of the L-H transition, comparing to theoretical predictions of E_r formation, and discerning the important factors that control pedestal shape and structure. To accomplish these goals this thesis will utilize the data from the new edge CXRS diagnostic to characterize the structure and behavior of the radial electric field in the edge pedestal region in a wide variety of plasma configurations and regimes.

Chapter 1 provides an introduction to the theme of the thesis and motivates the importance of the work. It gives sufficient background information on Alcator C-Mod, available diagnostics, and plasma regimes to provide a basis from which the discussions of subsequent chapters can be understood.

Chapter 2 discusses in detail the status and history of L-H transition theories, especially where it relates to radial electric field formation and behavior. It also introduces the concepts of **ExB** shear suppression, which is an integral part of this work. Lastly, it outlines the experimental work that has been performed on other machines in pursuit of a better understanding of the role E_r plays in high confinement plasmas.

Chapter 3 describes the details of charge exchange recombination spectroscopy as a plasma diagnostic. It begins with the physics behind the measurement, introduces the diagnostic setup on C-Mod and concludes with the data analysis techniques used to analyze the data presented in this work.

Chapter 4 presents the experimental results of the edge CXRS system. The obtained impurity ion temperature, velocity, and density profiles are introduced and their general characteristics and behaviors are described.

Chapter 5 presents the structure and behavior of the edge radial electric field, as determined from the CXRS data, in a variety of plasma operational regimes and examines its relationship to both particle and energy confinement.

Chapter 6 illustrates the relationship between the H-mode radial electric field and plasma parameters. It also examines the behavior of the main ion population in the pedestal region and discusses the implications C-Mod radial electric field measurements have for E_r formation, L-H transition, and pedestal structure theories.

Chapter 7 summarizes the results and main points of the thesis and discusses the next steps in pursuing this research.

Chapter 2

Tokamak Edge Radial Electric Fields: Theory and Experiment

Since the discovery of the H-mode on the ASDEX tokamak in 1982, numerous theoretical models have been proposed to explain the sudden plasma transition to a higher energy confinement state. Many of the models can not explain all of the observed phenomenology surrounding the L-H transition including particle and energy barrier formation, plasma flows, radial electric field formation and structure, turbulence suppression, and the extremely fast time scales. Some models have been refuted explicitly by experimental results and still others remain contenders to explain, at least in part, the wide range of phenomenology observed across the many different fusion devices. Unfortunately, many of the models do not provide predictions that are conducive to experimental testing, which makes comparisons to theory difficult or impossible. This chapter will attempt to summarize both the theoretical and experimental work done to date on L-H transition and pedestal formation theories with a focus on those that touch upon the edge radial electric field.

2.1 Early Theories

The first observations of the H-mode were made in the early 1980's in diverted tokamaks, namely, ASDEX [22], Doublet III (DIII) [23], and the Princeton Divertor Ex-

periment (PDX) [24]. Since that time, H-modes have been observed in many different magnetic configurations and seem to be a phenomenon ubiquitous to tokamak plasmas. However, the early observations of H-mode plasmas were observed concomitant with diverted plasma geometries and lead theorists to focus on such topics as electrical and thermal properties of the divertor channel [25] and edge magnetic shear stabilization of turbulence [26]. These theories were mainly speculative in nature, seeking plausible explanations for the observed phenomena consistent with the experimental information available at the time.

In 1985 Hinton proposed a model for the L-H transition in which the ion transport was assumed to be neoclassical and the electron behavior was influenced by the ions [27, 28]. For the high ion collisionality case the radial ion heat flux was found to depend upon the location of the active X-point, with the flux significantly reduced if the X-point is in the favorable $B \times \nabla B$ direction. The model purports to show that in this magnetic geometry large ion temperature gradients can develop at the edge and the L-H transition occurs at a critical, though non-specified, value of the radial ion heat flux. The model also predicts that an L-H transition can take place regardless of magnetic topology if the input power is sufficient to bring the edge ions into the low collisionality regime. In this way, Hinton explains the observed differences in the L-H transition power threshold between the unfavorable and favorable drift directions. However, Hinton's theory is vague on the specifics of the L-H transition trigger and does not give testable predictions on the pedestal shape, except to say that the edge ion temperature gradient scale length should be of order one ion banana width. The model also does not address the density pedestal formation and does not address how the ion dynamics couple to the electrons over the wide range of collisionalities considered, though the radial electric field is cited as a possible mechanism.

Other early L-H transition theories were developed through consideration of tokamak stability properties to a variety of known instabilities and turbulence mechanisms, including ideal ballooning and interchange modes [29], tearing modes [30] and resistive fluid turbulence and resistive kink modes [31]. Bishop, in 1986, considered the effect that divertor geometry, specifically the existence of a separatrix, has on

ideal ballooning and interchange instabilities in H-mode edge pressure gradients [29]. In this work he proposed that the existence of a current localized inside the separatrix could act to stabilize pressure driven modes by altering the local magnetic shear. In L-mode the edge temperature gradient is small as is the edge current making the edge region unstable to these modes. However, if this current could be increased then the edge region could be made locally stable enabling a positive feedback cycle and the sustainment of a temperature barrier.

Hahm and Diamond considered the effects of resistive turbulence in diverter geometry on the formation of the edge transport barrier [31]. They found that the increase in edge magnetic shear associated with a separatrix [26] has a larger effect on resistive pressure and resistivity gradient driven modes than it does on the ideal modes previously examined by Bishop, and that the ideal ballooning stability limit is not the only contributor to H-mode dynamics. The paper demonstrated that diverter geometry, through increased magnetic shear, reduces the step size of the resistive fluid turbulent diffusion processes, improving plasma confinement and stabilizing resistive kink modes near the LCFS. Hahm and Diamond propose two possible scenarios for the L-H transition, both of which rest on the idea that the improved confinement in diverted discharges enhances the edge plasma's stability against pressure driven modes and enables the plasma to support steeper edge gradients. Neither of these scenarios, however, represent a bifurcation as indicated experimentally.

Beginning in the late 1980's L-H transition theories began to focus on the radial electric field as a potential hidden variable that could have bifurcated states and thus act as the causal mechanism for L-H transitions. In 1988 Shaing published a neoclassical transport theory that included electric and magnetic fluctuations in which the electron and ion particle and heat fluxes were explicitly calculated and found to depend on the electrostatic potential, Φ [32]. Shaing proposed that a change in E_r ($E_r = -\nabla\Phi$) would cause the radial ion and electron particle fluxes to become unbalanced, inducing a change in the turbulence frequency and wave number spectrum that would act to keep the plasma quasi-neutral. If the change in the radial electric field were to a more negative value then the corresponding change in the turbulence

could lead to an improvement in both particle and energy confinement [32]. This and Shaing's later works considered the evolution of turbulence in the presence of a constant sheared electric field [33, 34] (sheared **ExB** flow) and concluded that the turbulence is suppressed by positive E_r shear ($\frac{dE}{dr} > 0$), a result that occurs due to the inclusion of diamagnetic effects in the analysis.

2.2 ExB turbulence suppression

Perhaps the most well known piece of L-H transition theory is the **ExB** shear suppression model. Although not proven, this model is widely accepted due to the great success it has had at explaining a large variety of observed plasma transport phenomena [2, 35]. The foundations for this model were provided in 1990 by Biglari, Diamond and Terry (BDT) [1], who showed that sheared poloidal flow leads to the suppression of turbulent transport through a reduction in the radial correlation length of the turbulence and that this effect is independent of the sign of both the radial electric field and its shear.

The BDT model was not the first to consider the effect of sheared flow on turbulence. The work of Shaing [32], which was discussed in section 2.1, was published first and both Shaing and Biglari had as their predecessor the work of Chiueh *et al*[36], which considered the effect of a sheared radial electric field on collisional drift wave turbulence. All three theories were developed in cylindrical geometry and **ExB** flow was not differentiated from poloidal flow. In his work, Chiueh assumed that the turbulence perturbations were ballooning like, while the works of Shaing and Biglari consider flute like perturbations.

Like Shaing, the BDT model considers the effect of poloidal flow on edge turbulence, however, it comes to very different conclusions. They find that poloidal flow has a shearing effect on turbulent eddies, which acts to de-correlate them without the need to include diamagnetic flow and most importantly, the BDT results are valid regardless of the sign of the flow or of its shear. According to the BDT model the rate at which turbulence is pulled apart by poloidal flow, that is the rate at which two

fluid elements separated by a radial distance Δr_t are separated by a poloidal distance ${k_{\theta t}}^{-1}$, is given by

$$\omega_s = (k_{\theta t}\Delta r_t)\left|\frac{\partial v_\theta}{\partial r} + \frac{v_\theta}{r_+}\right| \tag{2.1}$$

where v_θ is the poloidal velocity and r_+ is the minor radius at which the shearing is taking place. The radial diffusive scattering rate of the turbulence is given by

$$\Delta\omega_t = \frac{4D}{{\Delta r_t}^2}. \tag{2.2}$$

where, D, is the diffusion coefficient. These two processes together are responsible for the de-correlation of turbulence eddies with the shearing mechanism likely to be the dominant of the two.

The BDT model specifically addresses the strong poloidal flow (or flow shear) regime in which ω_s is assumed to be much larger than $\Delta\omega_t$. Under this constraint the poloidal flow and radial scattering decorelation mechanisms are found to couple and the characteristic turbulence decorrelation time is dependent upon both rates, $\tau_c = (2\omega_s^2\Delta\omega_t)^{-\frac{1}{3}}$. The characteristic radial correlation length of the turbulence is given by

$$\Delta r_c \simeq \left(\frac{\Delta\omega_t}{\omega_s}\right)^{\frac{1}{3}}\Delta r_t \tag{2.3}$$

from which one can see that the radial correlation length, Δr_c, will be reduced from its initial value, Δr_t, if the initial assumption was valid, namely $\frac{\Delta\omega_t}{\omega_s} < 1$. Thus, the BDT model provides a simple and in principle experimentally testable criterion to determine if the measured sheared poloidal velocity flow is sufficiently large to suppress the turbulence.

The physical mechanism by which the shearing takes place is actually very simple. Generally, a fluid element in a constant background flow will be carried along by the flow without distorting the shape of the element, see Fig.2-1a. However, if shear is added to the background field perpendicular to the direction of flow then the eddy is distorted, being stretched in the direction of the velocity flow and its width (radial

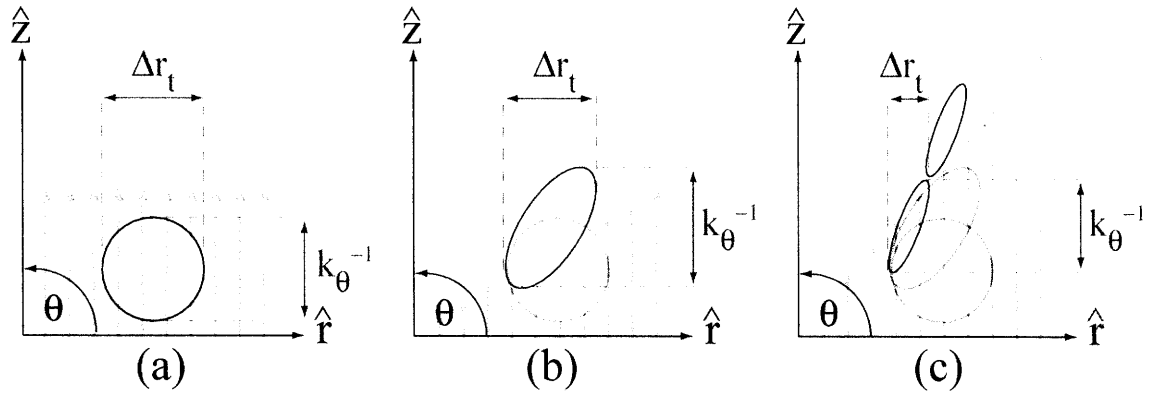

Figure 2-1: (a) An example turbulent fluid element in the presence of a constant velocity field (b) Distortion of fluid element due to sheared velocity flow (z(r)=αr)(c) de-correlated fluid element due to sufficiently large velocity shear

correlation length) reduced in the direction of the velocity gradient, see Fig. 2-1b. If the shear in the velocity flow is sufficiently large then the fluid element can no longer maintain its structure and is shorn apart, Fig.2-1c [35].

The results of the BDT model were derived in cylindrical geometry and as a result there is little differentiation drawn between poloidal flow (v_θ), **ExB** flow (v_E), and the total flow perpendicular to the magnetic field ($v_\perp$). This causes confusion as to which flow is actually important in the turbulence decorrelation process [2, 1]. The answer to this puzzle was provided by Kim *et al* [9] who, while extending the theory of ion-temperature-gradient-driven turbulence to the banana-plateau regime, derived to second order and in general toroidal geometry the equations governing the evolution and propagation of flute like energy and density fluctuations. In this work, Kim shows explicitly that these fluctuations are convected only by v_E and that the diamagnetic flow (Eq. 1.3) does not contribute. As such, all subsequent modifications to the BDT model consider specifically the effect of **ExB** velocity on turbulence.

The extension of the BDT model to full toroidal geometry was considered by Hahm for the cases of both circular cross-section [37] and arbitrarily shaped tokamak plasmas [38]. In these works Hahm considered not only the effect of v_E, which is important at the edge, but also parallel flow shear, $v_\parallel$, which can be important in the core of tokamak plasmas (e.g. internal transport barrier theory). In doing so, Hahm derived more complicated expressions for the flow shear rate, which improve the

original cylindrical approximation in that they correctly take into account the effects of magnetic shear. For the case of circular cross-section plasmas [37] the rotation shear rate is given by

$$\omega_s^2 = \frac{\Delta r_t^2}{\Delta\phi^2}\left\{\frac{\partial}{\partial r}\left(\frac{qV_E}{r}\right)\right\}^2 + \frac{\Delta r_t^2}{\Delta\eta^2}\left\{\frac{\partial}{\partial r}\left(\frac{V_\parallel}{rR}\right)\right\}^2, \tag{2.4}$$

where $\Delta\phi$ and $\Delta\eta$ are the toroidal and parallel correlation angles of the turbulence and q is the safety factor. For flute like perturbations, which align themselves along the magnetic field and so have $\Delta\eta \gg 1$, only the first term in equation 2.4 is important and given that the toroidal angle of the fluctuations is almost the same as the magnetic field angle, $\Delta\phi \simeq q\left(rk_{\theta t}\right)^{-1}$ [38], the rotational shearing rate can be represented in the more familiar form

$$\omega_s \simeq \left(k_{\theta t}\Delta r_t\right)\frac{r}{q}\left\{\frac{\partial}{\partial r}\left(\frac{qV_E}{r}\right)\right\}. \tag{2.5}$$

Note that in the case of weak magnetic shear, this result reduces to the cylindrical result given in equation 2.1. In practice the poloidal and radial scale lengths of the turbulence are assumed to be approximately equal and so the coefficient in equation 2.5 is set to 1. In toroidal geometry, the radial correlation length is again found to be related to the ratio of ω_s to $\Delta\omega_t$ though the dependence is different

$$\Delta r_c = \frac{\Delta r_t}{\sqrt{1+\frac{\omega_s^2}{\Delta\omega_t^2}}}. \tag{2.6}$$

As in the cylindrical approximation, the turbulence radial correlation length becomes significantly reduced when the rotational shearing rate Eq. 2.4 is greater than the diffusive radial scattering rate, which in toroidal geometry is given by $\Delta\omega_t = 4D_\phi\left(\frac{q}{r\Delta\phi}\right)^2$.

Flow shear can act to reduce turbulent radial transport not only by reducing the turbulence radial correlation length, but also by altering the cross-phase between the temperature, density, and potential fluctuations [39, 40, 41]. The radial fluctuation driven particle flux, Γ, and energy flux, Q, are composed of electrostatic and magnetic components that depend upon the cross-phase of the relevant fluctuating quantities.

The fluxes are given by [41]

$$\Gamma_j = \frac{\langle \tilde{E}_\theta \tilde{n_j} \rangle}{B_\phi} - \frac{\langle \tilde{J}_\parallel \tilde{b_r} \rangle}{eB_\phi} \tag{2.7}$$

and

$$Q_j = \frac{3}{2} k_b \left(\frac{n_j \langle \tilde{E}_\theta \tilde{T}_j \rangle + T_j \langle \tilde{E}_\theta \tilde{n_j} \rangle}{B_\phi} \right) + g_{2j} \left(\frac{\tilde{b_r}}{B_\phi} \right) \nabla T_j. \tag{2.8}$$

Here the subscript j denotes species, the fluctuating quantities are the electric field (E), the density (n), the temperature (T), the magnetic field (b), and the current (J). Directional subscripts are with respect to the magnetic field (B), the angles brackets denote averages on a flux surface (assuming circular flux surfaces), and k_b is Boltzman's constant. The factor $g_{2,e}$ can be determined from $g_{2e}\left(\frac{\tilde{b_r}}{B_\phi}\right) \approx \chi_{e\parallel}\left(\frac{\tilde{b_r}}{B_\phi}\right)^2$, where $\chi_{e\parallel}$ is the classical parallel thermal diffusivity.

The flux dependence on the cross-phase can be seen by writing out the contributions explicitly, for example, the electrostatic contribution to the particle flux is given by

$$\Gamma_j^E = \frac{\langle \tilde{E}_\theta^2 \rangle^{\frac{1}{2}} \langle \tilde{n^2} \rangle^{\frac{1}{2}} \cos \phi_{En}}{B_\phi} \tag{2.9}$$

where ϕ_{En} is the relative cross-phase between the density and potential fluctuations [40]. From equation 2.9 it is clear that the electrostatic contribution to the particle flux can change sign, be completely negated, or completely unaffected depending on the cross-phase of the fluctuations. Carreras and Ware have both shown that for resistive pressure gradient driven turbulence (RPGDT) **ExB** velocity shear and its derivatives can affect the cross-phase of the turbulence and thus alter radial transport [39, 42]. As yet, there is no complete theory on the effects of sheared **ExB** flow on the cross-phase of turbulent fluctuations.

2.3 Two-Step Theories

Many E_r based L- to H- transition theories are "two-step" theories: step one, the formation of a radial electric field and step two, the suppression of edge turbulence

via **ExB** shear. These theories can be categorized roughly by the proposed method of radial electric field formation. From examination of equation 1.1, one can see that there are two main feedback mechanisms by which the radial electric field can be altered: the **VxB** term and the pressure gradient term. Many theories have focused on the poloidal velocity contribution ($v_\theta B_\phi$) to E_r, in large part due to experimental observations of evolution in this quantity (impurities not main ions) prior to L- to H- transitions. The details of these observations will be discussed in section 2.6. Transition theories that require the poloidal velocity to be the dominant contribution to E_r at the time of the transition are referred to as poloidal spin-up theories and those that rely upon the diamagnetic contribution to E_r as pressure gradient theories. Poloidal spin-up theories will be discussed in sections 2.3.1, while pressure gradient theories will be addressed in section 2.3.2. Many of the following theories seek to identify a"trigger" mechanism for the L-H transition focusing, typically, on only one aspect of the plasma dynamics. As the plasma flows, pressure gradients, heat and particle fluxes, turbulence, and radial electric field are intimately connected they must be evolved self-consistently to determine reliably a causal mechanism for the L-H transition. Thus, the term "trigger" in these theories can be misleading and in the following discussions will only be used to indicate the dominant contribution to E_r at any given time.

2.3.1 Poloidal Spin-up Theories

Ion Orbit Loss

The first of the poloidal spin-up theories was developed by Shaing and Crume who, motivated by experimental results [43, 44] which indicated the presence of a negative electric field in H-mode plasmas, proposed a mechanism by which E_r could become more negative and lead to the transition [45, 46]. Namely, the loss of ions at the edge due to the intersection of their orbits with open field lines or limiter surfaces results in the formation of a negative radial electric field. By balancing the poloidal angular momentum imparted to the plasma as a result of ion orbit losses against

the neoclassical poloidal viscosity a bifurcation in the poloidal flow as a function of ion collisionality is found; When the poloidal mach number, $U_{pm} = \frac{B_\phi}{B_\theta}\frac{V_E}{V_{th}}$, is of order 1 the parallel viscosity decreases enabling a sudden positive increase (electron diamagnetic direction) in the poloidal flow, which gives an equivalent negative change to the radial electric field thus potentially yielding an L-H transition. In a later work, after experimental measurements on DIII-D demonstrated that the main ion poloidal flow is in the ion diamagnetic direction both in L-mode and in H-mode plasmas [47], Shaing clarified that only at the transition did the main ion rotation need to be in the electron direction and after the bifurcation it could switch to the ion diamagnetic direction [48].

In the ion orbit loss theory the authors do not exploit **ExB** shear suppression. Rather they draw upon Shaing's earlier work, discussed in section 2.1. As such they explicitly state that it is the effect of positive E_r shear ($\frac{\partial E}{\partial r} > 0$) on edge turbulence, which results in the improved plasma confinement and that negative E_r shear ($\frac{\partial E}{\partial r} < 0$) will act to destabilize the plasma turbulence resulting in a degradation of plasma confinement. The authors note that a negative decrease in the edge radial electric field would necessarily lead to regions of both positive and negative E_r shear, but claim the stabilizing effects of the positive region would outweigh the destabilizing effects of the negative. The results of experiments done on TEXTOR [49], which show that H-mode plasmas can be induced through the application of either a positive or negative electric field (an edge E_r "hill" or "well"), disagree with theories that rely upon the sign of the electric field or its shear. However, the formation of the negative E_r field through ion orbit loss is still valid and coupled to the BDT model is still a potentially viable model. This theory does not predict the shape or the depth of the radial electric field, although the negative E_r region is expected to be localized to a layer at the edge with a width proportional to the squeezed ion banana width[50]

$$\Delta r \sim v_{ti}\left(\frac{\epsilon}{\left(\frac{e}{m}\right)\left[\frac{dE_r}{dr}\right]}\right)^{\frac{1}{2}}. \tag{2.10}$$

where v_{ti} is the thermal velocity of the ion, m is the mass of the ion, e is the elementary

charge, and ϵ is the inverse aspect ratio. From this the width of the E_r shear layer ought to scale as the square root of the ion temperature over the E_r shear.

Around the same time that Shaing and Crume proposed their ion orbit loss theory, Itoh and Itoh also proposed an E_r based L-H transition model. In this model the non-ambipolar (NA) losses of electrons (turbulence, wave interactions, and magnetic braiding) and ions (orbit loss) are balanced under a zero net current condition, $\Gamma_i^{(NA)} = \Gamma_e^{(NA)}$, from which a self consistent radial electric field can be determined [51]. The model finds a bifurcation in the radial electric field and edge particle flux for a fixed value of n and T. However, it predicts that E_r will be negative in L-mode and become positive after the L-H transition. The region of the plasma in which this is supposed to occur is a thin sheath inside the LCFS of order the ion poloidal gyroradius. This prediction is in direct disagreement with all experimental measurements of radial electric field behavior made since that time, which find that the electric field in this region becomes more negative after the L-H transition.

Stringer Spin Up

Another poloidal spin-up theory was suggested by Hassam in 1991. He proposed that the Stringer instability[52], which was typically taken to be small in tokamaks due to magnetic pumping, could actually be sizable because the edge particle loss rate was much greater than predicted by neoclassical theory [53]. In this case, Pfirsch-Schluter flows in the presence of radial diffusive processes could lead to the poloidal and toroidal spin up of the plasma and a bifurcation of the edge density through the suppression of micro-turbulence. This theory has the advantages that it predicts changes in both toroidal and poloidal rotation and can occur on a very fast transport time scale (sub millisecond) as observed in the experiments. However, this theory again predicts poloidal rotation in the electron diamagnetic direction both before and after the L-H transition, which does not agree with experimental measurements.

Reynold's Stress

A third possibility for the poloidal spin up of the plasma, as shown by Diamond and Kim, is Reynold's stress induced poloidal rotation [54]. Reynold's stress is the shear on a fluid element that results from the presence of random turbulent fluctuations in the fluid momentum and it is obtained by averaging the fluid momentum equation over the fluctuations. In cylindrical coordinates the relationship between the Reynold's stress and the poloidal velocity can be seen directly by examining the poloidal velocity component of the fluid momentum balance equation

$$\frac{\partial}{\partial t} = -\left\langle \left(\tilde{\mathbf{V}} \cdot \nabla \tilde{\mathbf{V}}\right)_\theta \right\rangle = -\left\langle \frac{\partial}{\partial r}\left(\tilde{V}_r \tilde{V}_\theta\right) \right\rangle. \tag{2.11}$$

From this it is clear that if the Reynold's stress $\left(\tilde{V}_r \tilde{V}_\theta\right)$ is non-zero and has a radial gradient then it will induce poloidal flow [54]. Diamond and Kim demonstrated that the turbulence induced poloidal flow can be calculated either through examination of the energy density flux of the turbulence or by examining the derivative of the Reynold's stress obtained through a "vorticity" equation. Regardless of the method used, the driving term for the poloidal spin up are found to be the same.

One requirement for this type of flow generation is that there must be a radial gradient to the Reynold's stress. This can happen in a number of situations: 1) if the average size of the turbulent fluctuations is larger than the local scale length in the plasma, 2) if the turbulence is located within a spectral width (radial correlation length) of the LCFS, and 3) if the turbulence is in the vicinity of large local gradients in the plasma (e.g. temperature and density pedestals) [54]. The second possibility suggests that the induced poloidal flow will occur in a region inside the LCFS with a width of order 2Δ, where Δ is a characteristic width of the turbulence spectrum. Process 3 will occur when the turbulence size is of an order with the local gradient scale length ($\Delta \sim L_T, L_N$). Both possibilities 2 and 3 are likely in the edge region of tokamak plasmas, thus turbulence induced poloidal spin-up is expected to be a prevalent phenomena in this region.

2.3.2 Pressure Gradient Theories

The second category of "two-step" theories are those that focus on the pressure gradient contribution to E_r as the trigger mechanism for the L-H transition. These theories still rely upon **ExB** shear suppression to reduce the turbulence and maintain the increased gradients, but suggest that the increased **ExB** velocity shear is the result of, and not the cause of, the steep edge gradients. One such model was proposed by Hinton, who showed that a bifurcation in the edge temperature gradient may occur at a critical edge heat flux using the standard neoclassical expression for main ion poloidal flow, the idea of **ExB** shear turbulence suppression, and a simple expression for the plasma thermal conductivity, κ[55].

Hinton expresses the perpendicular thermal conductivity as the sum of a neoclassical contribution and an **ExB** shear modified turbulent contribution. The turbulent contribution is formulated such that as the **ExB** shear increases the turbulence contribution decreases

$$\kappa = \kappa_n + \frac{\kappa_a}{a + \gamma_a \left(\frac{\partial V_E}{\partial r}\right)^2}. \tag{2.12}$$

Hinton estimates the **ExB** velocity shear contribution as the neo-classically driven main ion poloidal velocity ($u_\theta \propto \frac{\partial T_i}{\partial r}$), a bad approximation as it neglects the pressure gradient contribution to V_E, which for the main ions is quite large at the edge. Nonetheless, using this the local conductive heat flux (heat flux is assumed to be the only loss mechanism) can be expressed as

$$Q\left(-\frac{\partial T}{\partial r}\right) = -k_n \frac{\partial T}{\partial r} - \frac{k_a \frac{\partial T}{\partial r}}{1 + \lambda_a \left(\frac{\partial T}{\partial r}\right)^4} \tag{2.13}$$

where κ_n, κ_a, and λ_a are assumed to be constants. This function has a local maximum corresponding to the bifurcation point or critical heat flux, if the turbulent conductivity is of order twice the neoclassical conductivity.

This model explores the scaling of the L-H transition power threshold by examining κ's dependence on plasma parameters. κ's dependence on the plasma density

indicates that there is a minimum density below which there can be no bifurcation and a similar result is obtained with respect to the magnetic field. A minimum density has been observed experimentally [56, 57, 58, 59], while a minimum magnetic field has not.

The type of bifurcation model promoted by this theory [55] is known as an S-curve model. The model can be depicted as in Fig. 2-2, where the variation of a particular parameter, A (temperature profile), varies in an 'S' shape pattern as a function of a control parameter, B (heat flux). In this diagram the L-mode is represented as Region 1, the H-mode by Region 2 and the critical heat flux to make the transition by B_{12}. Following the diagram in Fig. 2-2, the L-mode edge temperature gradient and heat flux increase together after the application of ICRF heating. When the critical edge heat flux is reached the temperature gradient reaches a bifurcation and jumps to a higher value. This increases the **ExB** shear through both the diamagnetic and neoclassical driven poloidal velocity components, which in turn suppresses the edge turbulence enabling the plasma to support the increased edge gradients. This model does not address the density pedestal formation, does not make predictions on pedestal or electric field structure, and can only be compared qualitatively to experiments due to the unknown coefficients in the thermal conductivity. Although Hinton's model can not be compared to experiment quantitatively, the experimental data can be examined as a function of edge heat flux or input power to determine if it displays an S-curve type bifurcation structure. This was done for C-Mod pedestal data by Hubbard *et al*[60] and such a structure was observed in both the density and temperature pedestal heights, supporting the idea of this type of bifurcation for the L-H transition physics.

The S-curve model is appealing in its simplicity, but there are some fundamental problems with the S-curve picture [61]. To begin with, it is a gross over simplification of the problem not taking into account much of the physics that must be present at the edge of the plasma including turbulence and poloidal flow. In addition, the S-curve picture is inherently a single curve description of the transition and can not take into account the multi-parameter dependence observed in L-H transitions.

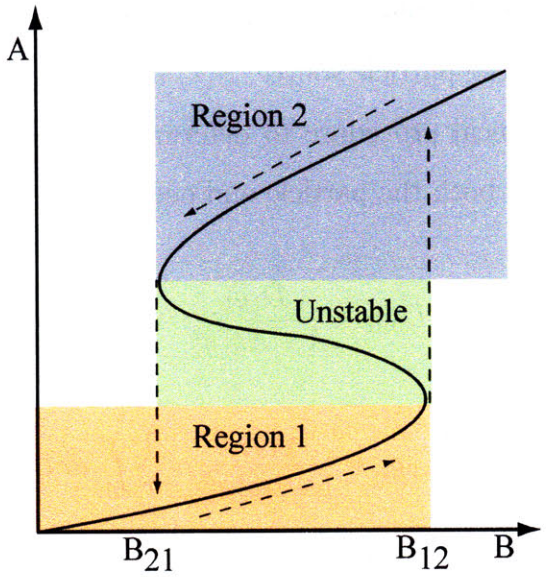

Figure 2-2: Example S-curve bifurcation diagram demonstrating the transitions between the two stable branches

In recognition of the multi-parameter deficiency of the basic S-curve model, Hinton and Staebler expanded upon the theory to include more than one dependent parameter and develop a model characterized by a bifurcation in both particle and energy confinement [62]. In this expanded version the authors consider both the particle and energy fluxes, rather than the heat flux. The diffusion coefficient and thermal diffusivity are modeled in the same way as in equation 2.12. However, in this work the **ExB** velocity shear is approximated as the shear in the pressure gradient contribution rather than the neoclassical poloidal velocity shear. Or, in other words, the radial electric field is assumed to be driven predominately by the main ion pressure gradient.

$$\frac{dV_E}{dr} \simeq -\frac{c}{eBn_i^2}\frac{dn_i}{dr}\frac{dp_i}{dr} \tag{2.14}$$

One should note that in deriving Eq. 2.14 the authors have neglected the term proportional to the second derivative of the pressure gradient. This was done to make the problem tractable. However, it is not a good assumption as this term is of the same order as the one that was kept. Using Eq. 2.14 the particle and energy fluxes are each functions of both the density and the pressure gradients ($-g_1$ and

$-g_2$). The gradients are determined by balancing the fluxes and the integral of the sources (assumptions on the particle source, $S(r)$ and energy source, $H(r)$, must be made) and using a graphical procedure to determine at which values of g_1 and g_2 there exists a solution for both the particle and energy fluxes [62].

$$\Gamma(g_1, g_2) = D_0 g_1 + \frac{D_1 g_1}{1 + \alpha g_1^2 g_2^2} = \frac{1}{r}\int_0^r dr S(r), \tag{2.15}$$

and

$$Q(g_1, g_2) = \chi_0 g_2 + \frac{\chi_1 g_2}{1 + \alpha g_1^2 g_2^2} = \frac{1}{r}\int_0^r dr H\chi(r), \tag{2.16}$$

By this graphical method, it is found that at low Q there exists only one solution of pressure and density gradients (L-mode), whereas if the value of Q is increased then multiple roots are found (only one of which is stable) at higher g_1 and g_2 (H-mode). The threshold criterion (when the gradients will switch roots) is determined by the product of the particle and energy fluxes ($Q\Gamma$). This model derives an estimate of the width of the edge gradient layer and determines that the width is proportional to the neutral penetration length and increases as the natural log of the edge heat flux. This implies that the width should decrease for higher edge densities (shorter neutral penetration lengths).

Hinton and Staebler note that an L-H transition by a poloidal spin-up theory does not disagree with this theory if it happens before the critical values of edge heat and particle flux are reached. A multi-parameter S-curve model of the L-H transition was reconsidered by Malkov and Diamond [61] who approached the problem analytically, rather than numerically, and showed that the transition criterion employed by Hinton and Staebler is invalid. In their model, Malkov and Diamond consider several additional effects to the system including the curvature of the pressure profile, which introduces hysteresis into the transition criterion. An expression or scaling for the pedestal width was not provided in their revision.

A complete theory of the L-H transition physics would necessarily have to account for all of the observed characteristics and to treat the evolution of all of the relevant plasma parameters in a self-conistent manner. As more and more pieces

of the puzzle (both theoretical and experimental) have come to light attempts have been made to construct a complete picture. These attempts led to the development of more comprehensive theories such as the "phase transition model", which considers together the evolution of the electric field, the poloidal velocity, and the main ion pressure gradient[63, 64, 65, 66]. In this model the turbulence drive is assumed to be proportional to the pressure gradient and the poloidal velocity is spun up via the turbulent Reynold's stress [65]. The transition from L-mode to H-mode occurs when the turbulent drive overcomes the damping of the **ExB** flow, at which time a "dynamo" like instability occurs. At this point the poloidal velocity and the electric field are amplified leading to **ExB** shear stabilization. According to this model the poloidal velocity is the dominant contributor to the electric field at the time of the transition with the pressure gradient developing on a slower time scale. However, when the input power is significantly greater than the threshold power the pressure gradient is the dominant contributor.

2.4 Pedestal Structure Models

There are many other models that specifically address the structure of the fully formed edge H-mode energy and particle barriers rather than considering the L-H transition itself. These models do not all touch directly upon the radial electric field, however, as E_r is believed to be an integral part of the pedestal structure, it is reasonable to assume that it might also follow the predictions of these theories. One such category of theories are those that analyze the stability of the edge pedestal to a variety of unstable modes such as ballooning or peeling. Some of the initial work on this topic was discussed earlier in section 2.1. However, since that time more progress has been made in developing these theories. References [67] and [68] give a good overview of these works and show that they generally predict a pedestal width scaling that is proportional to the ion poloidal gyro-radius ($\Delta P_{ped} \propto \rho_{i,\theta}^{\alpha}$). A simple scaling of the pedestal width can be obtained by assuming that the pedestal is at the critical MHD stability limit. This assumption yields a width scaling proportional to both the

ion poloidal gyro-radius and the plasma current ($\Delta P_{ped} \propto \rho_{i,\theta}^{\frac{2}{3}} I_p^2$) [69, 68]. However, most recent experimental work has not observed this kind of scaling in the edge pedestal data [67]. Another model connected to this topic is the work of Snyder *et al* [70], who have proposed a pedestal model for ELMing H-modes based on the magnetohydrodynamic (MHD) stability of the pedestal to coupled ballooning and peeling modes. This work suggests that the width of the pedestal scales as the square root of beta poloidal ($\Delta \propto \sqrt{\beta_\theta}$).

Sugihara *et al* have developed a pressure pedestal width scaling based on the assumption that the H-mode turbulence growth rate is balanced by the **ExB** shear, that the diamagnetic term is the dominant contribution to E_r and that the pressure gradient is close to the ideal ballooning stability limit [71]. The results of the model suggest the pedestal width should scale as

$$\Delta \propto \rho_{tor} S^2, \tag{2.17}$$

where ρ_{tor} is the toroidal Larmor radius and S is the magnetic shear.

A last set of theories that give predictions on the pedestal width are neutral penetration models [72, 73]. The neutral penetration picture employs a slab geometry to model the plasma edge and assumes purely diffusive transport. The plasma particle flux is balanced against the ionizing neutral flux and an equation describing the edge density pedestal is derived.

$$n_e(x) = n_{e,ped} \tanh C - \frac{x}{\Delta_{ne}} \tag{2.18}$$

where C is a constant of integration and is typically assumed to be small. The pedestal width, Δ, is given by $\Delta = \frac{2*\lambda_i}{E}$, λ_i is the neutral penetration length and E is a geometric factor associated with the flux surface expansion. The neutral penetration length is inversely proportional to the edge plasma density and this scaling will likely dominate the predicted pedestal width [67, 68] - a result that is experimentally testable.

2.5 Neoclassical Theory

Neoclassically, the radial electric field is determined through the conservation of toroidal angular momentum. The calculations are typically done under one of two ordering schemes: the MHD ordering or the drift ordering. In the MHD ordering the ion thermal velocity is assumed to be of the order of the ion toroidal velocity [74, 75, 76]. As a result of this ordering, the MHD formulation tends to neglect temperature gradient effects [77] and is most applicable in the core region of beam driven tokamak plasmas. The drift ordering assumes that the ion toroidal velocity is less than the thermal velocity and is more applicable to the edge region of non-beam driven plasmas [78, 79, 80, 81]. As this thesis is mainly concerned with the pedestal region of C-Mod (a non beam driven tokamak) the following discussion will focus on calculations done using the drift ordering.

The first neoclassical evaluation of the radial electric field using this ordering was done by Rosenbluth *et al* [78], who considered the problem in the banana regime. The calculations were done for the case of an axisymmetric plasma with circular flux surfaces and any poloidal variation of the potential and ion pressure were neglected. The Rosenbluth *et al* expression for E_r is proportional to the gradient of the temperature and is independent of the the plasma density

$$\vec{E_r} = \frac{\partial}{\partial r}\left[\frac{6T_0}{e}\left(\frac{R}{a}\right)^{\frac{1}{2}} \cdot \left[1 - 3\left(\frac{r}{a}\right)^2 + 2\left(\frac{r}{a}\right)^3\right]\right]\hat{r} \tag{2.19}$$

The first Pfirsch Schlüter (PS) calculation was undertaken by Hazeltine [79], who developed the "standard procedure" for determining the radial electric field in this regime. This procedure was to derive an expression for the gyro-orbit dependent portion of the ion distribution function, $\tilde{f}$, in terms of the gyro-orbit independent portion, $\bar{f}$. This was then used in the angular momentum conservation equation and to derive an appropriate drift kinetic equation based on his assumptions and orderings [79, 81]. The drift kinetic equation is then solved for $\bar{f}$, substituted into the angular momentum equation, and the equation for the radial electric field determined by setting the radial toroidal momentum flux equal to zero. From this procedure,

Hazeltine concluded that the equilibrium electric field in the PS regime was much smaller than the ion temperature gradient and in the large aspect ratio, circular flux surface limit is given by

$$E_r \simeq \frac{-T}{e}\left(\frac{r}{R}\right)^2 \frac{d\left(\ln T\right)}{dr}. \tag{2.20}$$

Later, this problem was reconsidered by Claassen *et al* [80] in the circular flux surface, large aspect ratio limit, and by Catto and Simakov [81] in general geometry. Catto and Simakov determined that Hazeltine's results and method were invalid for a number of reasons [81]: First, like Rosenbluth *et al*, Hazeltine assumed there was no poloidal variation of the ion pressure or the potential. Second, the drift kinetic equation employed by Hazeltine was incomplete. And third, an important term in the expression for the radial flux of toroidal angular momentum was neglected [81]. Catto and Simakov offer a new more complete procedure for determining E_r using fluid equations. The procedure requires evaluating both the gyro-viscous and perpendicular viscosity contributions to the stress tensor, which are then used in the angular momentum conservation equation to determine E_r. Catto and Simakov arrive at a very different and considerably more complicated expression for E_r than did Hazeltine. The full expression is too complicated to give here. However, if one assumes that the poloidal magnetic field is much smaller than the toroidal field, $\frac{B_p}{B_t} \ll 1$, then the solution becomes more tractable [77, 82]

$$\begin{aligned}
\left\langle \frac{R^4 B_p^2}{B^2} \right\rangle_\theta \frac{d\omega}{d\psi} &= -0.19 \frac{I^2 T_i T_e \left(\frac{d\ln T_i}{d\psi}\right)^2}{M\left\langle B\Omega_i\right\rangle_\theta \left(T_i + T_e\right)} \left\langle R^2 \left(1 - \frac{B^2}{\langle B^2\rangle_\theta}\right)\right\rangle_\theta \\
&+ 0.53 \frac{B}{\nu_i p_i m_i \Omega_i} \frac{d}{d\psi}\left\{ I^2 \nu_i p_i \frac{dT_i}{d_\psi} \left\langle R^2\right\rangle_\theta \left\langle \left(\frac{1}{B} - \frac{B}{\langle B^2\rangle_\theta}\right)^2 \right\rangle_\theta \right\} \\
&- 0.53 \frac{B}{\nu_i p_i m_i \Omega_i} \frac{d}{d\psi}\left\{ I^2 \nu_i p_i \frac{dT_i}{d_\psi} \left\langle \frac{R^2}{B^2}\left(1 - \frac{\langle R^2\rangle_\theta}{R^2}\right)\right\rangle_\theta \right\}.
\end{aligned} \tag{2.21}$$

The electric field, $E_\psi = -\frac{d\Phi}{d\psi}$, enters through the toroidal rotation frequency, ω, given by

$$\omega = -c\left(\frac{\partial \Phi}{\partial \psi} + \frac{1}{en}\frac{\partial P_i}{\partial \psi}\right). \tag{2.22}$$

In these expressions R is the major radius, B the magnetic field, $T_{i,e}$ the ion and electron temperatures, M is the ion mass, Ω_i the ion cyclotron frequency, p_i is the ion pressure, ν_i is the ion-ion collision frequency using the Braginskii definition and the function I is given by

$$I(\psi) = R^2 (B \cdot \nabla \zeta). \tag{2.23}$$

where ζ is the unit vector in the toroidal direction. Wong and Chan [82] presented a more compact version of Catto and Simakov's theory by utilizing the assumption of small $\frac{B_p}{B_t}$ at the outset and achieved results similar to the expression given above. However, they ignored the ion diamagnetic term as small in their calculations [77].

The Pfirsch-Schlüter formulation of rotation and electric field for the case of circular flux surfaces was actually obtained by Claassen *et al* [80] prior to Catto and Simakov. The general geometry results of Catto and Simakov and the expression given in Eq. 2.21 reproduce the results of Claassen *et al* when taken in the large aspect ratio and circular cross-section limit. The banana regime case was re-examined by Wong and Chan [83], who corrected some of the errors of Rosenbluth [78] *et al.* However, they too ignored the poloidal variation in the potential and acknowledged in reference [84] that the inclusion of this effect would result in substantial modification to the banana regime expressions derived in [83]. As such, to date, there is no reliable neoclassical formulation for the radial electric field in the banana regime.

2.6 Experimental Results from Other Tokamaks

Beginning in the late 1980's experimentalists too began to turn their attention to the radial electric field and the role it plays in the L-H transition. In 1989 CCT[85] and DIII-D[86, 43] demonstrated the connection between the edge radial electric field and H-mode confinement by showing, for the case of CCT, that H-modes could be induced

by imposing a radial electric field on the plasma, and for DIII-D, that E_r does indeed become more negative in the edge of tokamak plasmas from L-mode to H-mode. The earliest E_r measurements focused on confirming and/or refuting L-H transition theory. Only later were the details of the radial electric field structure, behavior and effect on confinement studied during H-mode plasmas. This is in part due to the initial impetus to understand the L-H transition physics, and in part due to the limitation of the diagnostics then available. It is easier to measure a change in E_r than it is to measure the complete profile. Now, as high resolution pedestal diagnostics become more prevalent, nearly every major tokamak has made measurements of the edge radial electric field structure and several features of the E_r profile have been found to be ubiquitous to tokamak plasmas. Namely, during L-mode the profile inside the LCFS is typically small in magnitude and exhibits very little shear, however, after the L-H transition a negative E_r well forms just inside the LCFS, coincident with the pedestal and the region of turbulence suppression.

2.6.1 DIII-D

The first measurements of the edge radial electric field on DIII-D were done using He emission spectroscopy (He II 468.8nm) [86, 43, 44, 87, 88] in D plasmas. The measurements indicated that somewhere in the edge region the impurity poloidal velocity evolved in the electron diamagnetic direction (indicating a negative radial electric field) 8-10 ms before the L-H transition. These results imply that the poloidal or perhaps perpendicular velocity is the trigger for the L-H transition. The authors point out that the largest velocity change at the L-H transition occurs not in v_θ or v_ϕ, but in $v_\perp$, thus illustrating the importance of this flow to any L-H transition theory. This observation was confirmed in ohmic discharges in which the observed flows are uncorrupted by external momentum sources and thus truly represent the flows inherent to the L-H transition physics. It should be noted that the spin up was not observed prior to all L-H transitions, making the precursor inconclusive. The inconsistency of the observed poloidal spin up could simply be due to the temporal or spatial limitations of the diagnostic [44, 87].

Later more detailed CXRS measurements of E_r from both impurity ions and main ion species enabled more exact comparisons with theory [89, 90, 47]. From these measurements it was clear that the H-mode radial electric field profile formed a negative well like structure inside the LCFS that was tens of kV/m deep and was roughly 1cm wide (full width half max). More importantly, these measurements gave temporal evolution information on the E_r well formation. They showed that 3ms before and after the L-H transition the main ion poloidal rotation was in the ion diamagnetic direction, giving a positive contribution to E_r. After the transition the main ion pressure gradient is the dominant term resulting in the negative radial electric field well. However, the main ion poloidal velocity contribution, though positive, is of the same order as the pressure term and can not be ignored [47, 90]. These measurements are important for L-H transition theories, as they disagree with the Stringer spin up theory, which predicts electron diamagnetic main ion poloidal rotation in the H-mode, and it poses challenges for ion-orbit theories, which require main ion electron diamagnetic rotation at the time of the L-H transition - a prediction that is unlikely though not impossible given the available data. The measurements made from the impurity species resulted in the same total radial electric field profile as the main ions [47], but the relative contributions were very different. The impurity poloidal velocity was in the electron diamagnetic direction, giving a negative contribution to E_r and was the dominant term at the L-H transition, with the pressure gradient contribution becoming more important tens of milli-seconds into the H-mode.

DIII-D data from a combination of probes, spectroscopic measurements and Thomson Scattering indicate that the changes in E_r toward more negative values several milliseconds before L-H transitions could not be accounted for by changes in the main ion pressure gradient [91]. Additionally, 0.5ms after L-H transitions there exists a fully formed radial electric field well and that at this time the main ion pressure gradient can only account for half of the well depth. This indicates that the main ion **VxB** term, and not the main ion pressure gradient, is the trigger for the L-H transition. To account for the observed negative change in E_r, the main ion perpendicular velocity must evolve in the positive direction or equivalently, $V_{\theta i}$ must increase in the electron

diamagnetic direction or $V_{\phi i}$ in the direction opposite to the toroidal magnetic field. To date, neither of these flows have been observed experimentally. One should note that the main ion flow measurements made in reference [47] show the main ion flow in the ion diamagnetic direction on either side of the L-H transition, which does not support the conclusions of reference [91]. However, these two sets of measurements were made in very different plasmas, with different main ion species, and different collisionalities. The discrepancies in the data point to our lack of understanding of the fundamental physics of the transition.

DIII-D probe data yields information about the potential and density fluctuations in the edge. These measurements show that the amplitudes of both the density and potential fluctuations are sharply suppressed after the L-H transition, but show no change in amplitude in the time prior to the transition in which E_r begins to evolve [91]. This is consistent with **ExB** suppression of turbulence and the idea of a critical E_r value for turbulence suppression. Probe measurements also provided information on the spatial structure of the fluctuations with respect to the shear in the E_r profile. In the negative shear region (innermost portion of the E_r well) the highest levels of suppression were observed on both the potential and density fluctuations. At the bottom of the well, ($E_r' \sim 0$) the density fluctuations were only modestly suppressed while the potential fluctuations were actually increased. This did not lead to enhanced transport because the potential and density fluctuations were completely out of phase.

CXRS measurements were used to determine the behavior of the E_r well in ELM-y H-mode discharges as a function of a variety of plasma parameters including magnetic field, current, density, and topology [92]. It was found that over the entire range of parameters and topologies explored, including both USN and LSN discharges, the general profile shape did not vary. For all cases, the width of the well ($\sim$1 cm) was found to be constant within the radial uncertainty of the measurement ($\pm$ 0.3cm). There was some variation in the depth of the well between -10kV/m and -30kV/m with the shallower wells observed at lower plasma densities, lower plasma current, and lower magnetic field - although a consistent dependency on these parameters was not found. Based on these results it was speculated that lower power threshold

discharges were correlated with shallower E_r wells [92]. This work also correlated faster L-H transitions with deeper E_r wells or alternatively higher **ExB** shear cases. This is again consistent with the idea of a critical shear rate that once attained enables H-mode confinement. The BDT criterion for turbulence suppression was estimated and found to be satisfied for all of the observed E_r wells. In addition to the ELM-y H-mode, the radial electric field profile has been examined in DIII-D's steady state H-mode regime the quiescent or QH-Mode. In this regime the E_r well is significantly deeper (100kV/m) than in the standard ELM-y discharges [93]. The width of the well remains the same, however, at approximately 1cm. The exception to this is QH modes that are run in double null with high plasma triangularity. This topology enables higher pedestal densities than can otherwise be obtained and the E_r well is observed to be significantly shallower and broader, despite the increased pedestal pressure.

2.6.2 ASDEX and ASDEX Upgrade

On ASDEX the magnitude of the edge radial electric field was estimated using line integrated measurements of impurity ion velocity perpendicular to the total magnetic field[94]. E_r was found to become negative inside the LCFS during H-mode plasmas with values of order -25kV/m . Additionally, the magnitude of E_r appeared to increase with higher magnetic fields (at constant q) similar to observations made on DIII-D [92]. Detailed radial electric field measurements from the ASDEX tokmamk are not available.

On ASDEX Upgrade (AUG) a novel way of inferring high time resolution (sub millisecond) information about E_r was developed utilizing the measured thermal charge exchange neutral particle flux from ripple trapped ions whose density is strongly dependent upon the magnitude of the radial electric field [95]. Using this method the magnitude of the radial electric field is inferred to increase rapidly after the L-H transition with a rise time of order 1ms. No evolution of E_r before the transition was observed, however, any changes that might exist could easily be lost in the noise of the measurement [96].

CXRS measurements of impurity ions are available in the core of AUG and can provide E_r measurements in this region, but to date the pedestal CXRS measurements are incomplete (lacking poloidal views) and can not be used to determine the edge E_r profile. However, AUG developed a second novel approach to determining the edge radial electric field structure. Using Doppler reflectometry it is possible to directly measure the plasma fluid velocity perpendicular to the magnetic field, $u_\perp$, and as this velocity is dominated by the **ExB** velocity they have a direct measurement of the radial electric field, $E_r = -u_\perp B$. Using this method the structure of the edge radial electric field has been studied in a variety of plasma regimes and configurations [97]. It was found that the radial electric field formed a negative well like structure in the pedestal region in both L-mode and H-mode plasmas. In L-mode the E_r well is between -5 to -10 kV/m deep, while in H-mode the well depth is between -30 and -45kV/m. The depth of the E_r well was also examined in improved H-mode plasmas, which exhibit higher confinement properties than standard H-modes, and was found to be slightly deeper than in standard H-mode discharges ($\sim$ -50kV/m). In general, the depth of the E_r well was found to scale with plasma confinement, or alternatively, the pressure gradient. No variation in the width of the well was observed. Lastly, AUG results indicate that the negative E_r shear region plays a more important role in plasma confinement than the positive shear region, disagreeing with the theories of Itoh [51] and Shaing [46], but consistent with Biglari, Diamond, and Terry [1].

2.6.3 JET

The edge radial electric field on JET has been measured using an edge CXRS diagnostic. The original measurements indicated the presence of an E_r well during H-mode operation that was -50 to -60 kV/m deep and $\sim$2cm wide (FWHM). The well was created by the diamagnetic term only. The poloidal velocity was not observed to change within the error bars of the measurement (5km/s) [98]. However, upgrades to this diagnostic system later demonstrated the existence of impurity ion poloidal rotation in the electron diamagnetic direction, similar to the observations made on other devices [99]. This rotation has been observed up to 9km/s and does in fact play

an important role in calculating the edge radial electric field. No poloidal velocity evolution prior to an L-H transition has been observed on JET, although the coarse time resolution (50ms) of the measurement makes such an observation unlikely. The measurements on JET indicate that the radial electric field well forms gradually after the L-H transition and that during the H-mode the radial electric field is set by the plasma confinement, rather than the confinement being set by the electric field. It is the authors opinion that on JET, **ExB** shear suppression is not responsible for triggering H-mode confinement and is not necessary to maintain it [99].

2.6.4 JFT-2M

The edge radial electric field on the JFT-2M tokamak was first measured using a combination of CXRS and passive impurity ion spectroscopy[100, 101]. It was determined that E_r became more negative after the L-H transition and formed a well like structure several centimeters wide and of order -15kV/m deep. Both the impurity ion poloidal velocity and pressure gradient terms made important negative contributions to the total E_r well depth and the impurity ion poloidal velocity was observed to evolve before the ion temperature profile again indicating a **VxB** trigger for the L-H transition. The location of the negative radial electric field shear is well correlated with the energy transport barrier, while the bottom of the E_r well aligns with the location of the particle barrier [100, 102]. This suggests that the negative E_r shear is correlated with the thermal diffusivity, while the negative radial electric field may itself contribute to an edge particle pinch[103]. The width of the radial electric field shear layer was examined in the context of ion orbit loss theory [104, 105] and a very weak (to non-existent) dependence of the width on the ion poloidal gyro-radius was found. However, the results were ultimately inconclusive as a sufficiently large range of ion poloidal gyro-radii could not be accessed and because the theory was reformulated so that the theoretical width was no longer dependent upon the examined parameter, see equation 2.10.

The installation of a heavy ion beam probe (HIBP) on JFT-2M enabled the examination of the edge potential and density fluctuations on a 1-2μs time scale

[106, 107, 108]. With this temporal resolution the behavior of these quantities could be tracked through very fast phenomena such as L-H transitions, H-L transitions and saw-tooth crashes. During L-H transitions the edge electric potential was found to drop in two stages. In the first stage the potential drops very quickly (10- 100 μs) and this coincides with the L-H transition and the suppression of low frequency turbulence (0-50kHz)[107, 102]. The potential stays constant for a short time ($\sim 1ms$) during which time higher frequency fluctuations appear(50-100kHz) and then the potential drops a second time with a time scale of $200\mu s$. The second drop in the potential is connected to the formation of the edge particle and energy transport barriers and it is at this time that the high frequency fluctuations are suppressed [107, 102].

These results point to a bifurcation phenomenon of the electric field that is not caused by the pressure gradient. As the L-H transitions in these discharges were caused by sawtooth crashes, one possible explanation is that the heat pulse from the sawtooth increases the population of low collisionality ions at the edge, which can be lost either through charge exchange or ion orbit effects and thus lead to the build up of an electric field [109]. This speculation is consistent with L-H transition theories that are based on ion-orbit loss effects. The poloidal mach number at the L-H and H-L transition in the plasmas was calculated and found to be of order unity, which is consistent with the predictions of Shaing's model [102]

2.6.5 Alcator C-Mod

Previous work on C-Mod estimated the magnitude of the radial electric field based on the propagation speed of magnetic fluctuations and inferred values of E_r of up to 250kV/m; this magnitude was over four times larger than measurements made on other machines [18]. The first spatially resolved measurements of the radial electric field profile on C-Mod confirm the initial estimates and will be described in detail in chapters 5. Additionally, in chapters 5 and 6, the C-Mod radial electric field measurements will be compared with the theoretical predictions presented in this chapter. In particular, the following pieces of E_r and L-H transition theory can be examined in light of the new C-Mod data:

1) The width of the fully developed radial electric field well can be compared to the theoretically predicted scalings discussed in this chapter. The possible scalings are listed in table 2.6.5.

E_r Width Scaling	Theory and Section
$v_{ti}\left(\frac{\epsilon}{\left(\frac{e}{m}\right)\left[\frac{dE_r}{dr}\right]}\right)^{\frac{1}{2}}$	Shaing and Crume (Eq. 2.10)
$\frac{1}{n}$	Hinton and Staebler (Sec. 2.3.2) and Neutral Penetration (Eq. 2.18)
$\rho_i^{\frac{2}{3}} I_p^2$	MHD Pedestal Stability (Sec. 2.4)
$\sqrt{\beta_\theta}$	Snyder *et al* (Sec. 2.4)
$\rho_{tor} S^2$	Sugihara (Eq. 2.17)

Table 2.1: Theoretical scalings of E_r well width

2) The quality of the plasma particle and energy confinement can be compared to the levels of **ExB** present in the pedestal region.

3) The complete radial electric field profile can be compared to the Pfirsch-Schluter neoclassical predictions of Catto and Simakov given by Eq. 2.21.

Chapter 3

The Edge Charge Exchange Recombination Spectroscopy Diagnostic on Alcator C-Mod

Charge exchange recombination spectroscopy (CXRS), also referred to as CXS and CHERS, is a popular method of measuring ion temperatures, densities and velocities in fusion plasmas. The popularity of this technique rests in its ability to provide temporally and spatially resolved measurements of these quantities in a relatively straight forward manner[110, 111]. The charge exchange reaction is given by

$$H + A^{Z+} \rightarrow H^{+} + A^{(Z-1)+*} \rightarrow H^{+} + A^{Z-1} + \gamma \tag{3.1}$$

where H is a neutral hydrogen atom and A is an ion of elementary charge Z. In this reaction the electron from the neutral hydrogen is transfered to the ion, leaving the hydrogen an ion, reducing the charge on A and typically leaving it in an excited state. The ion, A, subsequently de-excites and emits a photon, γ. CXRS is the collection and interpretation of the photons emitted as a result of charge exchange reactions. It was first employed as a plasma diagnostic in the late 1970's [112, 110] and is now used as a routine diagnostic on many fusion devices.

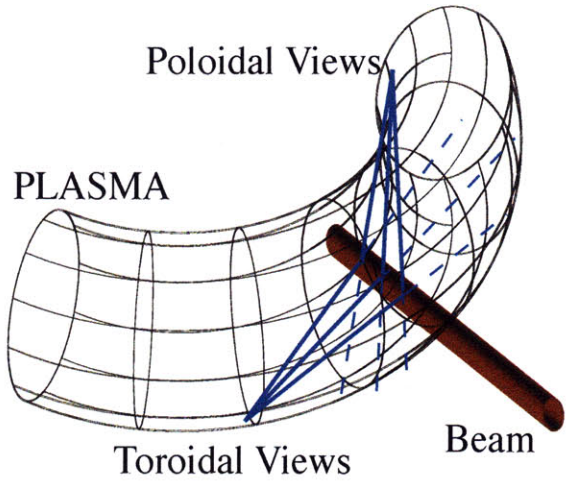

Figure 3-1: An example layout for a CXRS diagnostic including poloidal and toroidal views of a radially injected neutral beam

3.1 CXRS as a Plasma Diagnostic

Charge exchange reactions are typically induced by injecting neutral particles into plasma via energetic neutral beams or in some cases neutral gas puffs. The injected particles charge exchange with ions in the plasma causing them to radiate. The use of an external source of neutral particles provides the advantage of spatial localization, by restricting the emission region of the collected CX signal to the intersection of the lines of sight of the diagnostic and the trajectory of the injected neutral particles. The signal obtained is a line integrated measurement that contains contributions from collisional excitation, recombination, thermal charge exchange and the induced or "active" CX signal. The active portion is the only part of the emission that is localized. In order to separate out the active signal from the rest of the emission ('passive' or 'background' signal), it is necessary to have either a non-beam viewing periscope or to temporally modulate the source of neutral particles to gain a measure of the background. An example of a CXRS diagnostic layout using a neutral beam is shown in Fig 3-1.

CXRS diagnostics typically employ emission from low-Z impurities in the plasma rather than from main ions or from high-Z impurities. Measurements of the main ion

population are the most desirable. Unfortunately, this population is also very difficult to diagnose using charge exchange. This is in part because the large background emission from the main ion species makes obtaining an acceptable level of signal to background very difficult, and in part because the main ion species in fusion plasmas is typically an isotope of hydrogen, which after charge exchange becomes a neutral particle and is no longer bound to magnetic field lines. The new neutral atoms can travel significant distances within the plasma before emitting making the localization of the measurement very uncertain. This is of particular importance in regions of the plasma in which there are steep gradients. For charge exchange reactions that decay into the n=2 state of hydrogen (Balmer-series), typical excited state life times are of order 1e-7s and typical thermal velocities at the edge of C-Mod plasmas are between 1 and 4×10^5m/s. From this it is clear that ions can travel several centimeters before emitting, while the gradient scale length at the edge is only a few millimeters.

Charge exchange measurements using high Z-elements are possible, but not typically employed on fusion devices. First, high-Z elements tend not to be fully stripped in fusion plasmas, which means the emission from a particular transition is localized to a shell within the plasma in which the charge state of the ion exists. The location of this shell is dependent upon the plasma parameters and so a single set of diagnostic views is limited in the radial extent of the plasma it can measure. Low-Z impurities, being fully stripped, exist throughout the entire plasma volume, enabling charge exchange measurements to be made in all plasma regions. Second, the atomic structure of spectra from hydrogenic ions, as would result from fully stripped low Z-impurities, is considerably better understood than spectra from non-hydrogen-like atoms, making the analysis of low-Z impurities preferable.

Charge exchange reactions favor charge transfers that conserve the energy of the transfered electron. For the case of charge exchange between low Z impurities and neutral hydrogen the initial and final energy states of the electron ($\propto \frac{Z^2}{n^2}$) are unlikely to be the same. However, when the reactants are a particular distance apart the interaction of their potential wells can lower the energy of the electron such that the charge transfer can take place[111]. For low energy collisions, in which the relative

velocity of the reacting particles is less than the electron orbital velocity, this leads to a preferred quantum number n-level, into which the electron is transferred. The preferred n-level (n_{pref}) is given by

$$n_{pref} = n_0 \left(\frac{Z}{Z_0}\right) \left(\frac{2\sqrt{Z} + \sqrt{Z_0}}{2\sqrt{Z_0} + \sqrt{Z}}\right)^{\frac{1}{2}} \tag{3.2}$$

where n_0 is the initial n-level of the electron in an atom of nuclear charge Z_0 and Z is the atomic number of the charge exchange ion[111]. However, since charge exchange measurements are typically made using high energy neutral beams, the condition on the relative velocity of the charge exchange reactants is rarely satisfied. On C-Mod, CXRS measurement are made using a 50KeV neutral beam, which leads to reaction velocities of order twice the electron thermal velocity. At these energies, the charge exchange resonance at the preferred n-level is broadened to include several orbitals above and below the preferred level, which turns out to be highly advantageous for charge exchange measurements on fusion devices [111].

On Alcator C-Mod the dominant low-Z impurity is boron and the preferred charge exchange line is the n=4-3 transition at $\lambda = 749.7A$. Unfortunately, this line is in the ultraviolet region of the electromagnetic spectrum making it difficult to measure using standard optical components such as lenses, mirrors, and fiber optics. However, there are potentially transitions with wavelengths in the visible portion of the spectrum at higher n-levels that will still be populated by charge exchange reactions thanks to the n-level resonance broadening at high energy. Alternative longer wavelength BV charge exchange lines include the n=6-5 line at $\lambda = 2981.38A$, the n=7-6 line at $\lambda = 4944.67A$ and the n=8-7 line at $\lambda = 7618.59A$. The n=6-5 line is near ultraviolet, while the n=8-7 line is near infrared, making the n=7-6 transition the best choice for charge exchange measurements on C-Mod. There is also a $\Delta n = 2$, n=9-7 spectral line at 4519.8A, however, the intensity of this line is much lower than the n=7-6 transition.

Charge exchange reactions also have a preferred quantum angular momentum state (l), which is approximately equal to the preferred n-level for n-levels around

or greater than n_{pref} [110]. Thus, charge exchange reactions can cause un-statistical population of quantum levels. However, the Stark effect provides a mechanism that can remix the levels [111]. If the rate of the level mixing is faster than the de-excitation rate of the line then the levels will still be statistically populated. A rule of thumb to determine the critical density at which a specific transition is fully mixed was provided by Sampson [113] and later used by Isler [110],

$$n_e = \frac{Z^{7.5}}{n^{8.5}} \frac{1}{8.5 \times 10^{-16}}. \tag{3.3}$$

Here, n_e is the electron density in $cm^{-3}$and n is the quantum level. For the BV, n=7-6 transition this yields a critical density of $1.3{\times}10^{19}m^{-3}$, which is below the typical pedestal density on C-Mod indicating that the l-levels should be fully mixed. An alternate expression for the critical density was provided by Pengelly and Seaton [114] and altered by Fonck *et al* [115] for application to fusion plasmas. In their formulation the critical n-level above which the l-states will be fully mixed is given as a function of the ion charge, ion temperature, plasma density, and Z_{eff}. Using their formulation with Z=5, n=7, Z_{eff}=1.5 and T_i=500eV, the critical density is found to be around $1{\times}10^{18}m^{-3}$; considerably, lower than the value found from Eq. 3.3. In either case, the l-levels for the BV n=7-6 spectral line can be assumed to be fully mixed in C-Mod plasmas.

The spectra obtained from CXRS measurements are representative of the original ion population. For example, charge exchange with fully stripped boron, B^{5+}, results in emission from B^{4+}, but the information in the spectra pertains to the original B^{5+} population. If the ions have a Maxwellian velocity distribution then the spectra will also have a Maxwellian distribution of the form [111]

$$S(\lambda) = S(\lambda_0) \exp\left[-\frac{1}{2}\frac{(\lambda-\lambda_0)^2}{\lambda_0^2}\frac{m_i c^2}{T_i}\right]. \tag{3.4}$$

Here, $S(\lambda)$ is the intensity of the spectral line, c is the speed of light, λ_0 is the rest wavelength, m_i is the mass of the emitting ion, and T_i is the temperature of the ion population. This expression assumes the ion population has no net flow along the

line of sight of the measurement. The temperature of the impurity ion population is given by the Doppler broadening of the spectral line and is proportional to the width of the distribution. The standard deviation of the distribution (W_D) described by Eq. 3.4 is

$$W_D = \lambda_0 \sqrt{\frac{T_i}{m_i c^2}} \tag{3.5}$$

and the ion temperature is given by

$$T_i = m_i c^2 \left(\frac{W_D}{\lambda_0}\right)^2. \tag{3.6}$$

If the ion population has a net flow parallel to the line of sight of the diagnostic then this will result in a Doppler shift, $\Delta\lambda$, of the spectral line away from its rest wavelength and the adjusted distribution is given by

$$S(\lambda) = S(\lambda_0) exp\left[-\frac{1}{2}\frac{(\lambda - \lambda_0 - \Delta\lambda)^2}{W_D}\right]. \tag{3.7}$$

The corresponding flow velocity is

$$V_i = \left(\frac{\Delta\lambda}{\lambda_0}\right) c. \tag{3.8}$$

The measured brightness of the CX signal is proportional to the density of the ion population as well as the neutral hydrogen density and the effective cross-section for excitation of the CX line [115, 110]

$$\epsilon^{\lambda}_{CX} = \frac{1}{4\pi} \sum_k \sum_j \langle \sigma v \rangle^{\lambda}_{j,k} \int n_i n_{0,j,k}(l) dl. \tag{3.9}$$

Here ϵ is the CX brightness at wavelength λ in $\frac{photons/s}{m^2 ster - radians}$. The summation on j is over the energy components present in the neutral beam, the summation on k is over the excited state populations in the DNB (see section 3.4), $\langle \sigma v \rangle^{\lambda}_{j,k}$ is the relevant charge exchange reaction rate, n_i is the impurity ion density, $n_{0,j,k}$ is the neutral density, and the integral is over the path length of the diagnostic's lines of sight

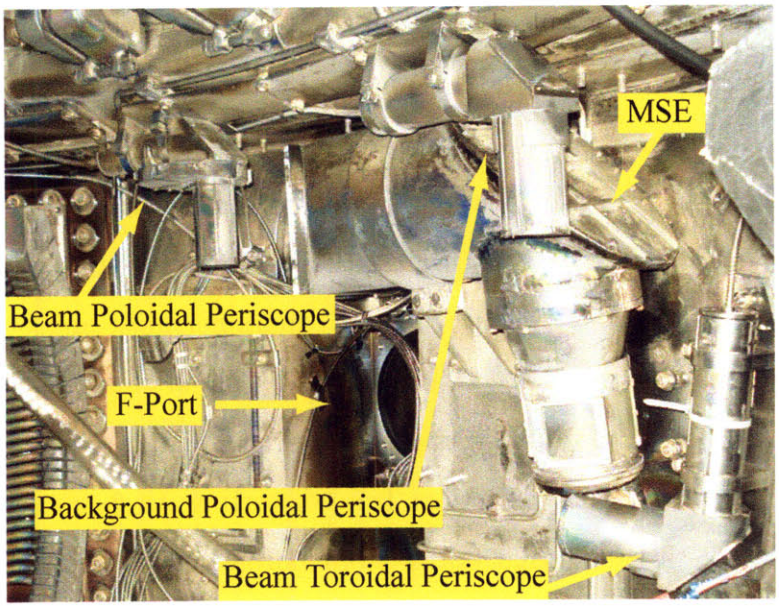

Figure 3-2: Low field side edge CXRS periscopes

(LOS) through the beam. If the neutral density of the beam components is known as a function of distance along the diagnostic's LOS then the density of the impurity ion population can be determined from the measured brightness. To do this the impurity ion density is assumed to be constant over the path length and is removed from the integral. The impurity ion density is then given by

$$n_i = \frac{4\pi\epsilon^{\lambda}_{CX}}{\sum_k \sum_j \langle\sigma\nu\rangle^{\lambda}_{j,k} \int n_{0,j,k}(l)dl}. \tag{3.10}$$

3.2 The C-Mod Edge CXRS Diagnostic

3.2.1 In-vessel Components

The low field side edge CXRS diagnostic system on Alcator C-Mod consists of three periscopes: a beam viewing toroidal periscope, a beam viewing poloidal periscope and a background viewing poloidal periscope. All of the periscopes are located inside the C-Mod vacuum vessel and are secured in place by means of studs welded to the vessel wall. The periscopes are shown in Fig. 3-2.

The beam viewing poloidal periscope has 25 lines of sight that cover a 5.5cm range

at the edge of the plasma between r/a of 0.75 and 1.0. The views have a 2mm spot-size at their focal point, which is at the mid-plane of the plasma, and a radial resolution of order 3.5mm after taking into account the curvature of the plasma and path length of the views through the DNB. The periscope is mounted to the top of the C-Mod vacuum vessel and the central view through the DNB is vertical to within a tenth of a degree both toroidally and radially, although the inner most and outermost views still have a radial angle of order 4°. The lines of sight of this periscope are shown in Fig. 3-3. The poloidal periscope utilizes black passivated shim-stock and plates as a viewing dump to prevent reflections from distorting its spectra and has a built in shutter to protect the internal optics from boronizations and other potentially damaging processes. The shutter can be actuated externally by means of a push-pull system, enabling the state of the shutter to be changed as needed during the course of a campaign.

Originally, the DNB had a purely radial trajectory and the beam poloidal periscope views were designed to align with the center of the beam. However, in 2006 the beam path was tilted by 6.6° toroidally, shifting the center of the beam line away from the periscope views by several centimeters. The mounting plate for the poloidal periscope was re-designed to accommodate this shift, however, it was no longer possible for all of the poloidal views to lie along the center of the DNB path. They now cross the beam trajectory at an angle of 5 degrees to the beam and also no longer fall along a major radius, see Fig. 3-4. This results in a deviation of several mm (from the center of the beam) for the inner and outermost viewing chords. Fortunately, the loss of signal due to this deviation is not significant, and the largest negative consequences are the increased difficulty in radially calibrating the periscope and installing it without damaging the fiber optics.

The beam viewing toroidal periscope was designed to work in conjunction with the pre-existing beam poloidal periscope. It has twenty lines of sight covering a 5cm range between r/a of 0.8 and 1.03 with a spot size at the focal point of 2.2mm. Ideally, this periscope would have a purely toroidal viewing geometry perpendicular to the DNB. Unfortunately, this was not possible due to the toroidal tilt of the beam and

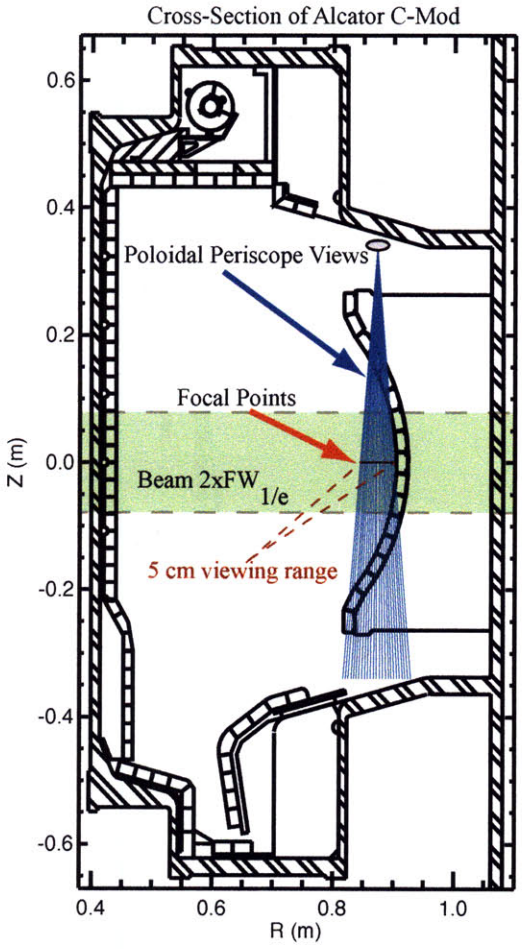

Figure 3-3: Lines of sight of the beam poloidal periscope views

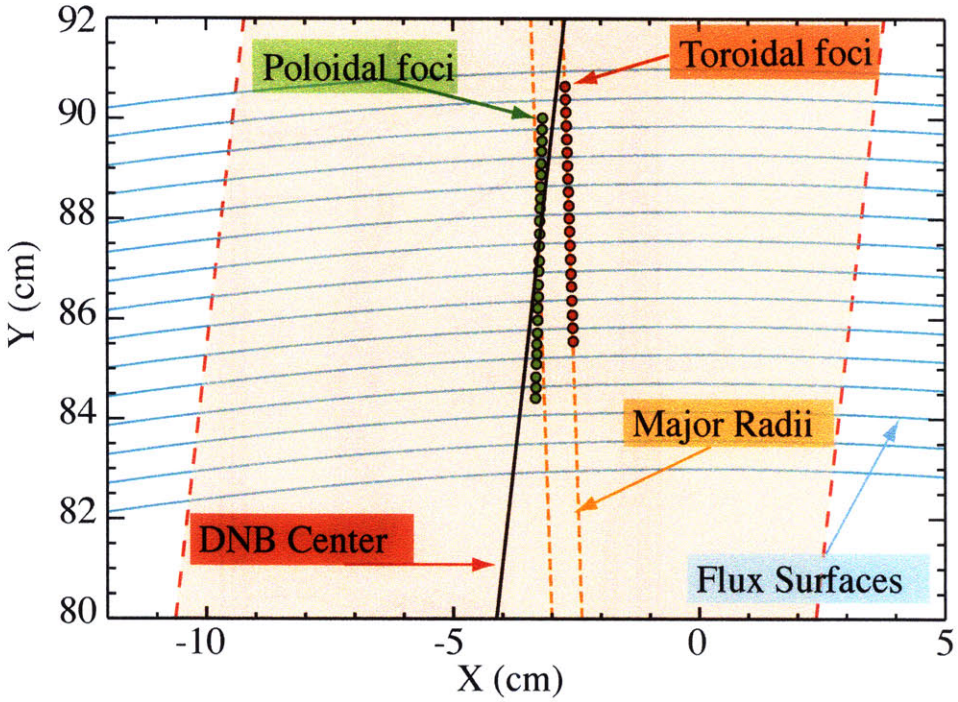

Figure 3-4: Poloidal and toroidal periscopes focal points with respect to the DNB path in a right handed cartesian coordinate system with the origin at the center of the tokamak and the y-axis passing the center of F-port.

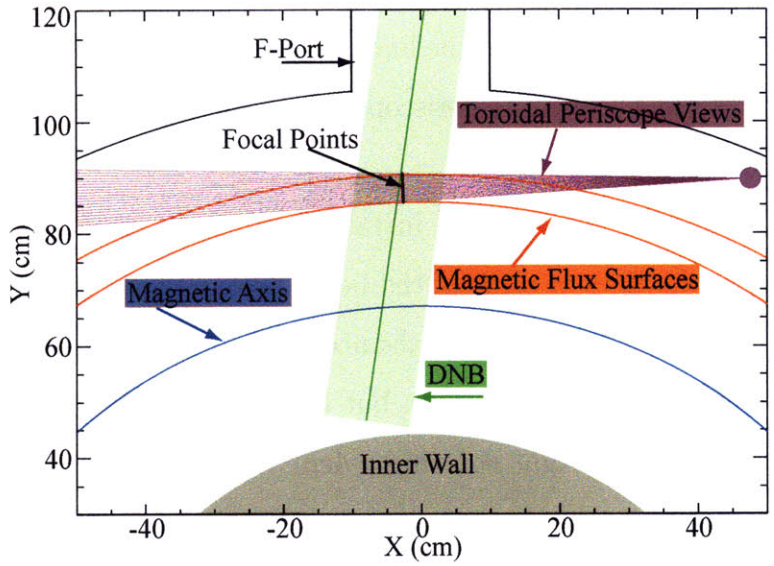

Figure 3-5: Lines of sight of the toroidal periscope views in a right-handed cartesian coordinate system with its origin at the center of the tokamak and y-axis passing through the center of F-port

an interference with the MSE diagnostic. Instead, the periscope is mounted slightly below the mid-plane, views vertically upward at an angle of 7.6 degrees and its focal points make a net angle of 9 degrees to the DNB path, see Fig. 3-4. The vertical tilt of the periscope creates a total angle between the periscope's lines of sight and the magnetic field at the out board mid-plane of roughly 17 degrees. Both the poloidal component to the periscope's LOS and the angle to the total magnetic field must be taken into account when analyzing data from this periscope. The lines of sight of this periscope, shown in Fig. 3-5, have a longer path length through the plasma than the poloidal periscope and were designed such that the center view is tangent to magnetic flux surfaces at a major radius of R_m=88.6cm. The focal point of the central toroidal periscope view was intended to intersect the center of the DNB path, however, the actual focus fell short by ~5mm, an error that was not realized until the end of the 2007 campaign.

The toroidal periscope does not have a built in shutter, it relies instead on a 3.5 inch long cylindrical snout to protect the internal optical components from boron coating. Also, it does not have a viewing dump, since its views intersect the side

and face of the E-port ICRF antenna. As a result, the line integrated spectra can be distorted by reflections. This makes the line integrated or passive toroidal spectra unreliable and makes using a separate periscope as a measure of the toroidal background spectra impossible.

The background poloidal periscope, installed prior to the 2008 run campaign, was designed to mimic the lines of sight of the beam poloidal periscope to enable active charge exchange measurements without the need to modulate the DNB. It is mounted similarly to the beam poloidal periscope, but toroidally displaced by 20 degrees, see Fig. 3-2. It has 20 lines of sight covering a 4cm viewing range between r/a of 0.85 and 1.05cm with a 2mm spot-size at their foci and equivalent radial resolution to the poloidal periscope. Like the toroidal periscope, it does not have a shutter and uses a 3.5 inch snout to protect its mirrors and lenses. A black passivated steel plate has been installed beneath this periscope to provide a viewing dump.

In addition to the low field side periscopes there is also a toroidal periscope that images the high field side pedestal region. This periscope utilizes a D_2 gas puff at the inner wall to make localized CXRS measurements of the BVI population. It has seven lines of sight covering a 2.4cm region that intersects the inner-wall gas puff and an equivalent set of background viewing chords that are displaced vertically from the puff by 4 centimeters. These background chords make it possible for the inner wall data to be analyzed for spatially localized CXRS measurements without the advantage of a temporally modulated neutral source. The inner-wall views have a spot size of 4mm at their foci, though when mapped to the outer wall this is reduced to 3mm. The temperature profiles derived from this periscope can be used to complement the outer-wall profiles.

3.2.2 External Components

The CXRS periscopes use achromat lenses to focus the collected light onto high OH silica clad silica (SCS) fibers with a core diameter of 400μ. These fibers carry the light out of the C-Mod vacuum vessel where they are coupled to relay bundles (also 400μ SCS), one bundle per periscope, that transmit the light from the C-Mod cell to an

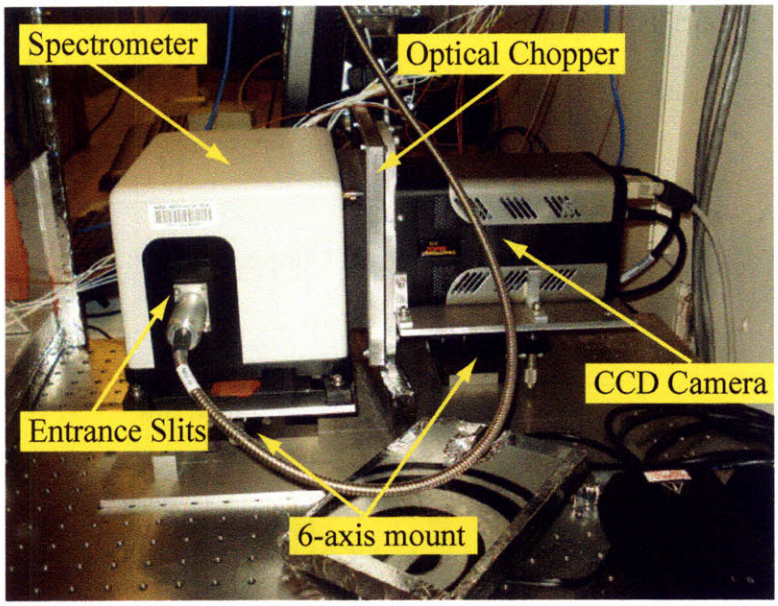

Figure 3-6: The edge CXRS system including Kaiser spectrometer, optical chopper, and Photonmax CCD camera

adjacent setup lab where the CXRS spectrometer systems are located. There are two parallel systems (Photon1 and Photon2), each consisting of a Kaiser spectrometer, an optical chopper, and a Photonmax CCD camera, see Fig. 3-6. The camera and spectrometer together are mounted on adjustable stages with 6 degrees of freedom (3 linear and 3 rotational) that allow the focus of the spectrometer onto the CCD chip to be optimized. The periscope relay bundles can be coupled interchangeably to either system.

The spectrometers are compact, high-throughput (f/1.8) devices made by Kaiser Optical Systems [116]. They employ an f=85mm (f/1.8) lens at the entrance slit, a narrow bandpass filter, a volume phase holographic grating (VHG) [117], and an f=58mm (f/1.2) lens at the exit to focus the light onto the CCD chip. The design of the spectrometer is shown in Fig. 3-7. The grating has a central dispersion wavelength of 494.3nm and a transmission efficiency at the central wavelength of order 80% [116]. One advantage of the Kaiser design is that the f-number of the system is of order the f-number of standard fibers optics used for diagnostic purposes (f/2.2). Thus, there is no need for awkward matching optics between the fibers optics and the spectrometer lenses. Additionally, the design enables multiple fibers to be stacked vertically at

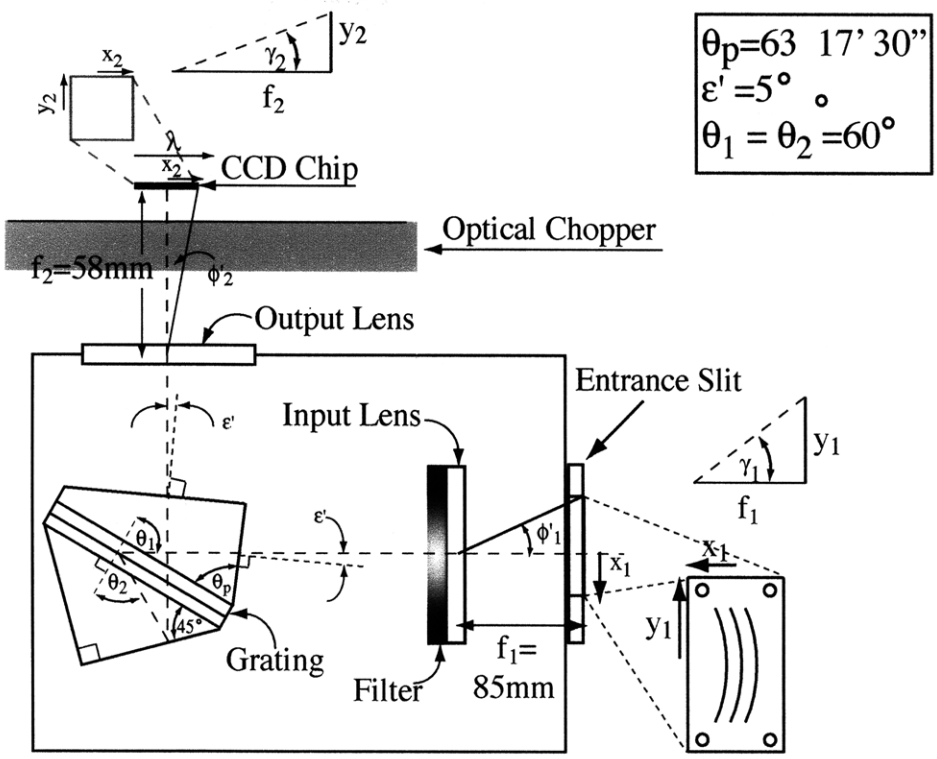

Figure 3-7: Layout of the C-Mod CXRS spectrometer design [118]

the spectrometer entrance without having to worry about spectral overlap in the image plane [118] and the narrow bandpass filter allows the use of multiple slits by preventing spectral overlap in the horizontal (wavelength) direction. These features maximize the number of fibers that can be imaged simultaneously by a single system.

There are some disadvantages to using a VHG grating. The wavelength range of diffracted light is limited to a narrow region around the central wavelength of the grating and so the spectrometer can not be tuned to look at different spectral regions [117]. Additionally, the very short focal lengths of the spectrometer lenses introduce significant spectral curvature into the image plane. Fortunately, this curvature can be effectively eliminated by using specially designed curved entrance slits, which vertically align the spectra from the fibers in the image plane [118].

The C-Mod systems use 3nm bandpass filters made by Barr Associates Inc [119] that have over 90% transmittance in the selected wavelength range. As shown in Fig. 3-8, these filters enable three spectra to be imaged horizontally without overlapping

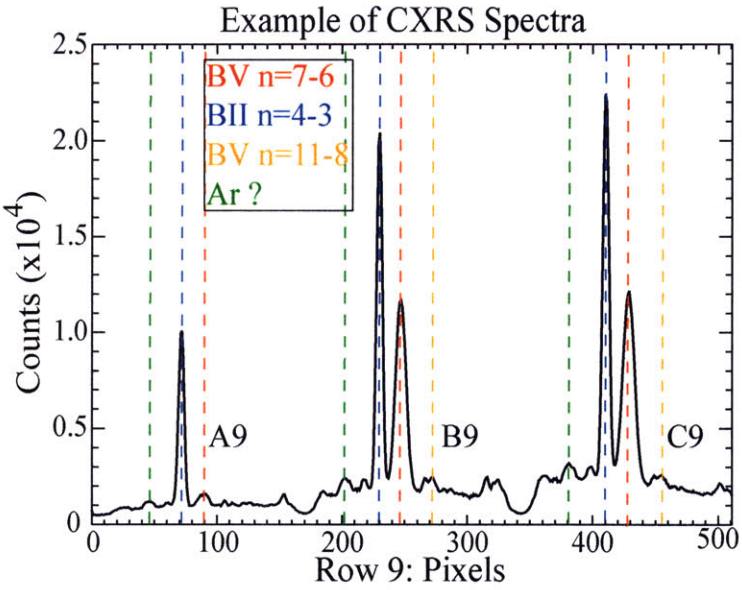

Figure 3-8: Three spectra from the CXRS diagnostic imaged together without spectral overlap

on the CCD chip. Additionally, the magnification of the chosen lenses enables 18 spectra to be imaged comfortably in a single vertical column. Taking advantage of this, the CXRS system uses three parallel curved 150μ entrance slits with 18 fibers per slit, see Fig. 3-7. This gives each system the capability of imaging 54 spectra for a total of 108 potential views of the plasma. The individual channels on the spectrometers are designated by row and column. The rows (1-18) correspond to the vertically stacked fibers, with 1 being the top fiber and 18 the bottom and the three columns (A-C) correspond to the three entrance slits.

The CXRS diagnostic uses Princeton Instruments 16-bit, frame transfer, Photon-MAX:512B CCD cameras with a 512×512, 16μ pixel chip. The cameras are thermoelectrically cooled to -70° C and controlled through Winspec and custom Visual Basic software. Each camera has a dedicated PC used for triggering and data collection. The standard timing for the systems is 5ms integration time with a duty cycle of 6.2ms, although alternative timing schemes have been used. The cameras are typically run in frame transfer mode with a 5MHz digitization rate. This means that the cameras integrate continuously, even while shifting frames from the exposed portion of the CCD chip to the covered region from where they are read out. During

this period of time ($0.6\mu s/row \times 512 rows = 0.3ms$) it is possible for the spectra to be distorted by incoming light from different locations in the plasma. Consequently, an optical chopper is employed to cover the CCD chip while the data is being shifted.

The chopper consists of a multi-tabbed wheel driven by a Boston Scientific 300M motor and controlled by a Boston Scientific Model 300CD controller and synchronizer. For the CXRS systems to function properly the timing of the chopper wheels must be synchronized with the triggers being sent to the cameras so that the cameras are exposed during integration times and blanked while the data frames are being shifted. To do this, the positions of the chopper blades are recorded by optical sensors, through which they pass on each rotation. This information is fed back to the synchronizers, which maintain the match between the chopper blade frequency and an external clock being provided to the system. The external clock used by the edge CXRS system comes from an MPB decoder on the C-Mod CAMAC highway. A Datx A/D Digitizer is used to keep track of the camera and chopper timing, as well as perform the necessary clock division and triggering. More information on the timing systems for the edge CXRS diagnostic can be found in reference [120].

3.3 Calibrations

To correctly interpret CXRS data the entire system must be calibrated carefully and accurately. The LOS of the periscopes must be calibrated spatially to know exactly where in the torus they are focused and the positions of the periscopes must be known to determine the 3-D geometry of the lines of sight. This information is then used to integrate the views through the DNB and also to invert the passive CXRS spectra. The system must have a complete brightness calibration, including the transmissions of all of the individual components, in order to correctly translate number of counts on the CCD to number of photons in the plasma, and thus the density of the emitting impurity ion population. A detailed knowledge of the instrument functions of the systems and the bandpass filters are needed to de-convolve the true CXRS spectra from the effects of the system's optics. And lastly, wavelength and linear dispersion

calibrations of the spectrometer-CCD camera system are required to infer velocities and temperatures from the positions and widths of the de-convolved spectral lines. All of the calibrations needed to maintain the CXRS system can be grouped into one of two categories: in-vessel calibrations and external calibrations, and will be discussed in the following sections.

3.3.1 In-Vessel Calibrations

Radial calibrations are performed for each periscope at the beginning and end of every run campaign. These calibrations can only be performed when the machine is up to air. They cannot be done in-situ by, for example, sweeping the edge of the plasma across the periscope views, because the accuracy needed for these calibrations exceeds the accuracy of EFIT. However, the relative radial calibrations of the different periscopes can be checked by this method. The radial calibrations for these periscopes, when done correctly, are good to within $\pm$1mm.

All of the radial calibrations employ a table that mounts to the inner-wall of the tokamak table and was designed and built specifically for this purpose. The table consists of a curved aluminum plate, which is strapped to the inner-wall and from which extends a perpendicular spar. The radius of curvature of the metal plate matches that of the inner wall so that when the plate and wall are flush the spar represents a major radius, along which distances can be measured easily and accurately. A digital level is used to insure the plate is level toroidally to within a tenth of a degree and to measure the angle (from horizontal) of the spar in the radial direction. To perform the radial calibrations for the poloidal periscopes a flat calibration table is attached to the end of the spar and is positioned directly beneath the periscope, at the mid-plane as shown in Fig. 3-9A. The periscope is then back-lit and the positions of the focal points are recorded on a sheet of paper attached to the calibration table. The light cone of the lines of sight are also recorded by raising and lowering the table position. For the toroidal periscope the table is positioned in front of F-port several inches below the mid-plane and a vertical plate is clamped to its surface to intercept the toroidal views. The toroidal periscope is back lit and the

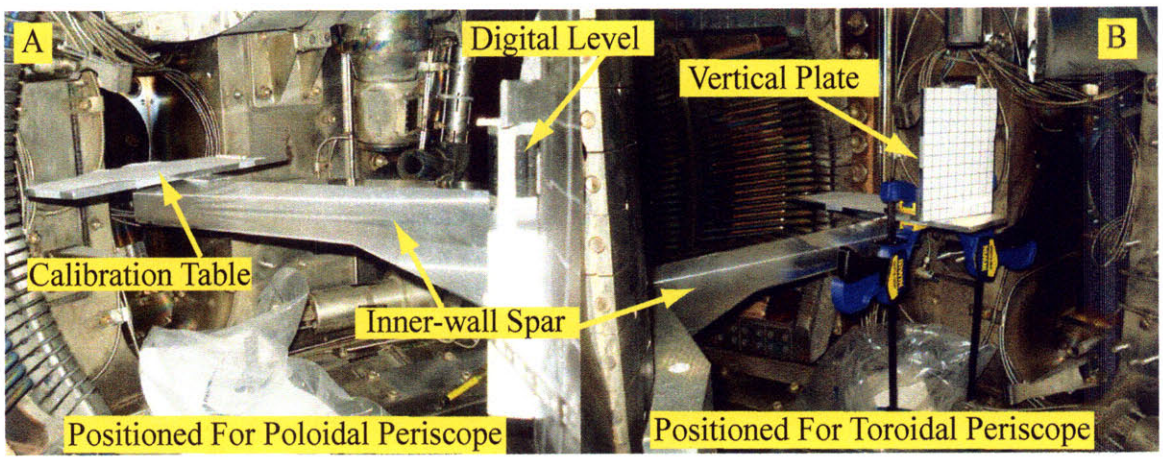

Figure 3-9: Radial calibrations of the poloidal and toroidal periscopes using the inner-wall spar and table

vertical table is shifted until the focal points are found. This procedure is illustrated in Fig. 3-9B. The light cone of the toroidal periscope can be examined by moving the vertical plate forward and backward.

Part of the brightness calibration is also done in-vessel. A US-060-SF lamp made by Labsphere Inc. (a light source with a known brightness) is taken in-vessel and used to completely fill the periscope's optics. This is easily done for the poloidal periscopes as the Labsphere can be placed on the calibration table and held in place beneath the periscope, as shown in Fig. 3-10. The toroidal periscope calibration is more difficult and less accurate as the labsphere must be held steady in front of the light cone of the periscope by hand for an extended period of time. When doing the in-vessel brightness calibrations the fibers from the periscopes are connected one at a time to single relay fiber, which is connected to a single channel on one of the two spectrometer systems. The result is a transmission calibration as a function of wavelength for all of the fibers from all of the periscopes, $T_{peri}(\lambda)$. This calibration can be performed more comfortably by removing the periscopes from the vessel. However, this is not always an option before and after every campaign, and is not as accurate as fiber transmissions can be changed with a change in the radius of curvature of the bundle and they can also be damaged in the removal process. The in-vessel transmissions alone do not make a complete brightness calibration. One also needs the transmissions of the individual relay bundle fibers, $T_{relay}(\lambda)$, that are used

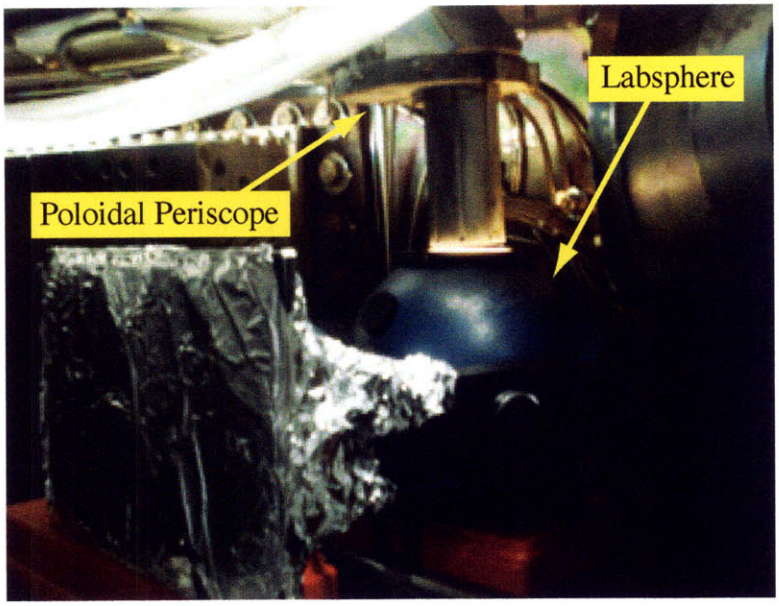

Figure 3-10: Brightness calibration method for the poloidal periscopes

to connect the periscopes to the spectrometers and a channel-to-channel brightness calibration at the spectrometer itself, $C_{spec}(\lambda)$. These pieces of the calibration process will be discussed in section 3.3.2. The complete brightness calibration is given by

$$B_{cal}(\lambda) = T_{peri}(\lambda)T_{relay}(\lambda)C_{spec}(\lambda) \tag{3.11}$$

Lastly, detailed measurements of the positions of the periscopes must be made in order to determine the 3-D geometry of their LOS through the plasma. To do this, an 'inside micrometer' and digital level are used to measure the distance and angle between known points on each periscope and a fixed reference point on the inner wall. These same tools are also used to measure the distances and angles between the focal points of the periscopes and known positions on the periscope body. The process for the poloidal periscopes is relatively simple as the periscope views are almost perfectly vertical. The toroidal periscope, however, views the plasma with both a vertical and radial angle, making these measurements and the reconstruction more complicated.

3.3.2 External Calibrations

As mentioned in the previous section, the transmissions of the relay fiber bundles and a brightness calibration of each channel on the spectrometer are needed to complete the brightness calibrations of the system as a whole. The transmissions of the relay bundles are obtained by coupling them to a short ($\sim$ 1m) fiber of matching size and numerical aperture and illuminating the fiber end with a constant broad band light source. The level of signal from this coupled system (as a function of wavelength) is then compared to the signal when the short fiber alone is illuminated to determine the attenuation in the relay bundles. To get the channel-to-channel brightness calibrations of the spectrometers the labsphere is used to fill the light cone of a single short relay fiber, which is then connected to each channel of the spectrometer. The complete brightness calibration is reproducible to within 15%, however, the actual error in the brightness calibration during a campaign can be greater if there is damage to the periscope fibers, lenses, or mirrors as a result of plasma operation.

The filter functions are obtained by a very similar process to the brightness calibrations. A constant broadband light source (doesn't need to be calibrated) is connected to a single fiber optic, which is connected to each channel on the spectrometer in turn. At each channel, two spectra are taken, one with the filter in place and one with the filter removed. The ratio of the two spectra give the filter function, which must be divided out of the actual CXRS spectra before any analysis can take place. The data and resultant filter function for B9 of Photon2 is shown in Fig. 3-11.

$$F_f(\lambda) = \frac{S(\lambda)_{\text{filter in}}}{S(\lambda)_{\text{filter out}}} \tag{3.12}$$

Instrument functions, wavelength calibrations and the linear dispersions for each channel are obtained using a neon light source. Neon has twin spectral lines at wavelengths of 4939.043A and 4944.987A. These lines conveniently straddle the key wavelength of interest, 4944.67A, and are thus well situated to provide all of the necessary calibration information. The instrumental line shapes of the system are not symmetric and it was found that a minimum of three Gaussians are required to

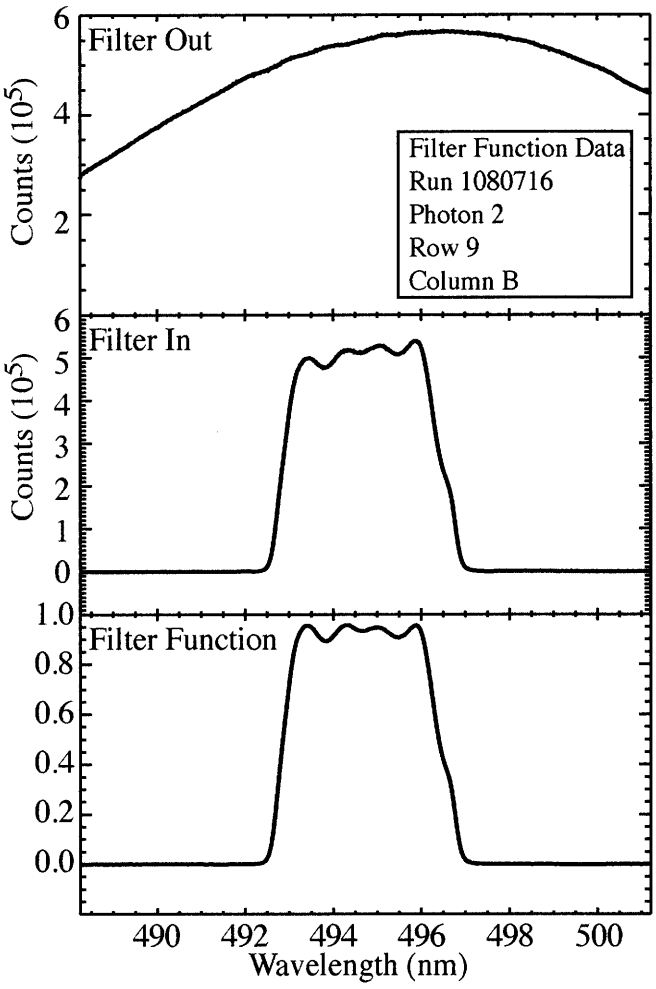

Figure 3-11: Filter Function Calibration Data

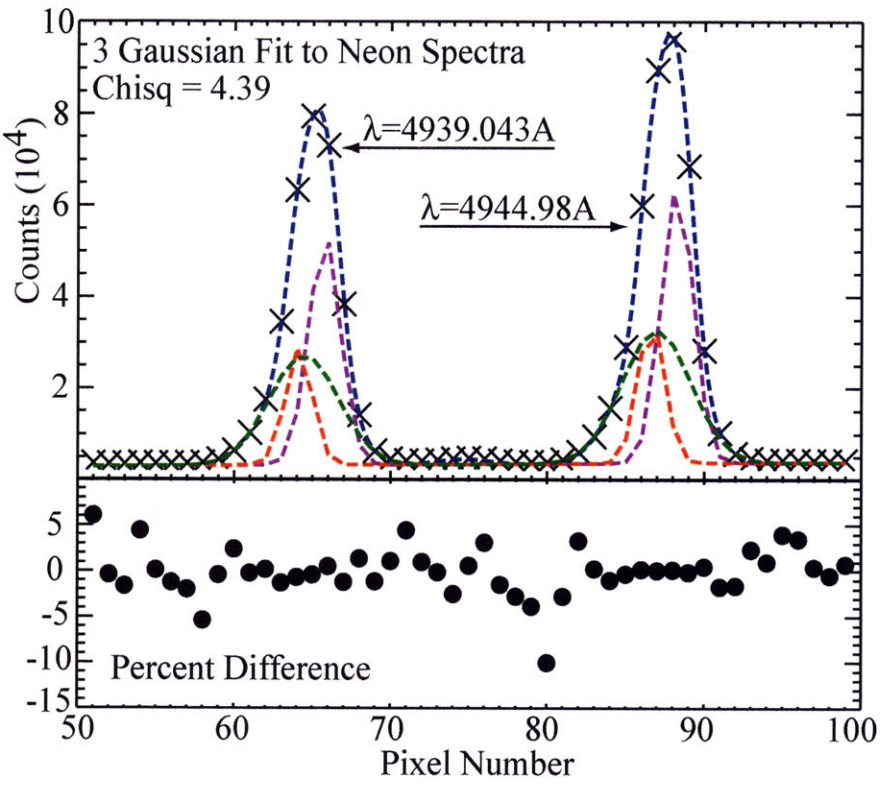

Figure 3-12: Three Gaussian fit to neon calibration lines used to determine instrument functions, wavelength calibration and linear dispersions

fit them well. The two neon lines for each channel are fit simultaneously in pixel space to three Gaussians plus a linear background. An example instrumental fit is shown in Fig. 3-12. The relative heights, widths and locations of the Gaussians are left as free parameters in the fit. The only requirements are that the same relative relations be used to fit both spectral lines and that the widths and amplitudes of the lines be positive.

The actual positions of the spectral lines, P_1 and P_2, are defined as the center of mass of the fits to the lines, and the linear dispersion and wavelength calibrations are calculated using these center of mass positions. The linear dispersion is given by

$$LD = \left(\frac{4944.98A - 4939.043A}{P2 - P1}\right)\frac{A}{pixel} \tag{3.13}$$

and the wavelength calibration by

$$\lambda(x) = LD(x - P_2) + 4944.98A. \tag{3.14}$$

The variable x is the 512 element array of pixels. The wavelength calibration can be determined quite very accurately with this method to better than 0.01 pixels ($\tilde{<}1km/s$).

The instrument functions for each channel are also derived from the fits to the neon spectra. The center of mass of the line is chosen as the zero, and the positions of the three Gaussians in the fit are written as a function of their distances away from the center of mass. The widths remain the same as the fitted values, but the fitted Gaussian amplitudes are multiplied by a normalizing factor such that the area under the instrument function in pixel space is equal to 1. The instrument function in pixel space, $I_f(x)$ is then described by 9 parameters, three amplitudes A_i, shifts L_i, and widths w_i

$$I_f(x) = \sum_{i=1,3} A_i exp\left(-\frac{1}{2}\left(\frac{x - L_i}{w_i}\right)^2\right). \tag{3.15}$$

Filter functions and brightness calibrations are done only at the beginning and end of each run campaign. The neon calibrations, however, are retaken every few weeks. This is because the instrument functions tend to relax (become broader) slowly over time and the wavelength calibrations drift in response to changes in temperature and pressure. This sensitivity was suspected when it was noted that the wavelength calibrations tended to drift in a single direction over the course of a day and then recover almost to their starting point on the following day. The drift over the course of a single day can be quite significant leading to errors in velocity measurements of up to 5km/s.

In order to maintain accurate wavelength calibrations on a shot-to-shot basis, it is necessary to have a neon calibration lamp coupled to at least one channel of the

spectrometer to track the wavelength drifts. It was also discovered that there were slight, but noticeable, differences between the wavelength drifts in each column of the camera. Thus an entire row (three channels) on each camera is now dedicated to neon calibrations. After every plasma shot the neon spectra from these channels are fit, their shifts relative to the most recent wavelength calibration determined, and the wavelength calibrations in each column adjusted accordingly by assuming that the relative shifts within a given column are the same. This method has proven to work well, reproducing correct wavelength calibrations within a few km/s over long periods of time. Even so, neon calibrations are performed every few weeks to refine the calibrations and new calibrations are almost always taken when an experiment that places high priority on charge exchange data is run - reducing the instrumental uncertainties on priority data.

3.4 The Diagnostic Neutral Beam

The small size of C-mod and its high density plasmas makes it impossible to install the type of tangential neutral heating beam that is employed on larger fusion devices. Rather, C-Mod employs a diagnostic neutral beam (DNB) that is both physically smaller and considerably less powerful than its big brother the heating beam. C-Mod's DNB, located on F-port (see figure 1-2), is injected radially into the plasma with only a slight toroidal angle (6.6°). It is a hydrogen beam capable of delivering up to 7 amps of beam current at 50KeV/amu, with the possibility of either long pulse (up to 1.5s) operation or fast modulation on the order of tens of milliseconds. However, when operating at beam currents of 6 amps or greater the current rise time of the beam is of order 25ms, thus limiting the actual modulation capability. For CXRS purposes a beam timing of 40ms high and 20ms low is usually requested.

The DNB was designed to have a focal length of 4m and a full width 1/e of 6cm at this point in the beam's trajectory [121]. This would place the focal point near the edge of the plasma, see Fig. 3-13. The focusing is provided by the acceleration grids, which are machined to have the same curvature as the surface of a 4m radius sphere.

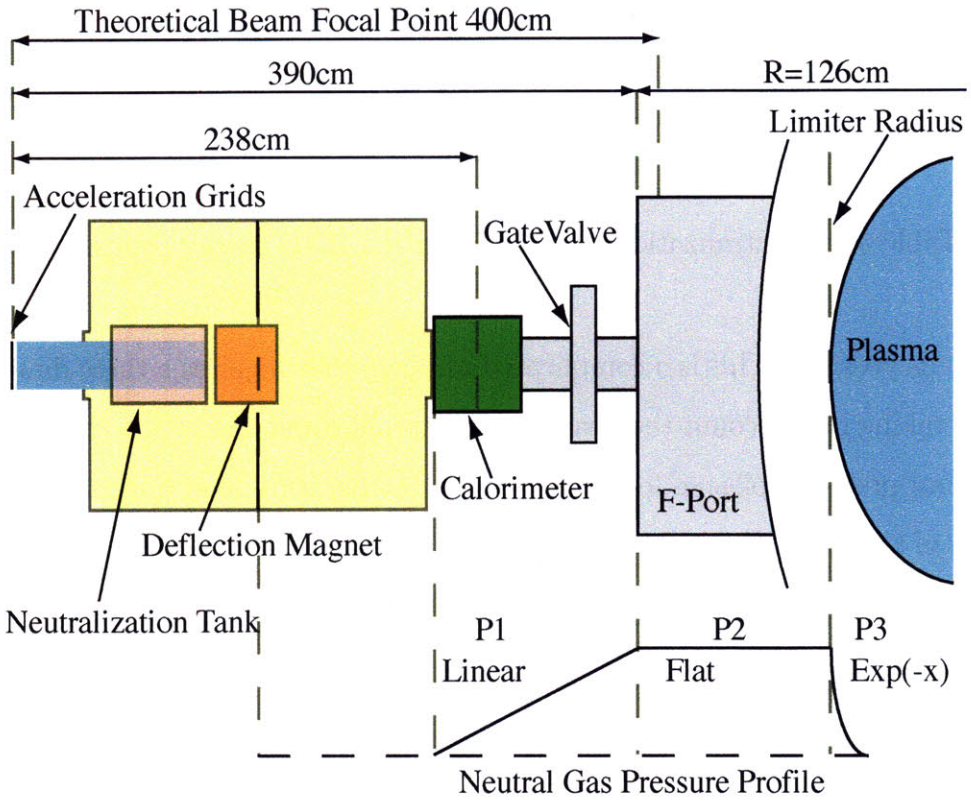

Figure 3-13: Schematic of the layout of the C-Mod diagnostic neutral beam

The profile of the DNB has been measured at several locations along the beam path and the measured widths deviate significantly from the designed parameter. The measurements at the calorimeter show a Gaussian profile with a full width (1/e) of 6.4cm. This is very close to the designed focal width, but the calorimeter is located only 230cm away from the grids, indicating that the curvature of the grids is incorrect by a factor of two. In addition, CXRS and BES measurements of the beam profile at a major radius of 80cm [122] demonstrate a considerably wider beam (~13cm FW) than would be present if the beam was focused correctly. For the purposes of the edge CXRS system the beam is assumed to have a Gaussian profile with a full width 1/e of 13 cm that does not vary over the region of interest ($84cm < R_m < 90.5cm$).

CXRS measurements of impurity density rely upon an accurate knowledge of the density of the neutral population with which the impurities are interacting. Lacking a direct measurement of the density of the beam components, the attenuation of the DNB through both the edge neutral gas and the plasma must be calculated as

Beam Component	Efficiency η_j
H^+	0.52
H_2^+	1.56
H_3^+	3.0
H_2O	1.8

Table 3.1: Neutralization efficiencies for the DNB energy components

carefully as possible. This is a complicated problem that requires a three dimensional analysis taking into account the beam current, profile, and energy fractions as well as the neutral pressure, plasma location, density, temperature, and impurity levels as a function of time.

The beam ion source is a lanthanum hexaboride (LaH_6) cathode which, when heated, emits electrons and creates a small plasma source. Ions from that plasma are extracted and accelerated down the beam line at 50KeV by 4 acceleration grids. The ion beam is composed mainly of H^+ ions but also has non-negligible contributions from H_2^+, H_3^+ and H_2O^+. After the acceleration grids the ions enter a magnetically shielded neutralization chamber filled with H_2 gas and are neutralized due to thermal charge exchange reactions. The fraction of the beam that is neutralized is a balance between the charge exchange rate and the re-ionization rate. The resultant neutralization efficiencies, η, for the four beam components are given in table 3.1. These efficiencies represent how many neutral hydrogen atoms are produced by the neutralization process per beam ion component.

The neutral particles that result from the H^+ ions preserve the full 50KeV from the accelerations grids and will be referred to as the full or first energy fraction of the beam. Likewise, neutrals from H_2^+, which have an energy of 25KeV, are the half or second energy component, H_3^+ the third, and H_2O^+ the eighteenth. After the neutralization tank any remaining ions are swept out of the beam line by a bending magnet. In this region the beam line is cryogenically pumped to minimize the attenuation of the newly formed neutral beam. A single channel visible Ocean Optics spectrometer is used to measure the Balmer-α ($\lambda = 656.28$nm) spectra from the interaction of the neutral beam with the remaining hydrogen gas. The contributions

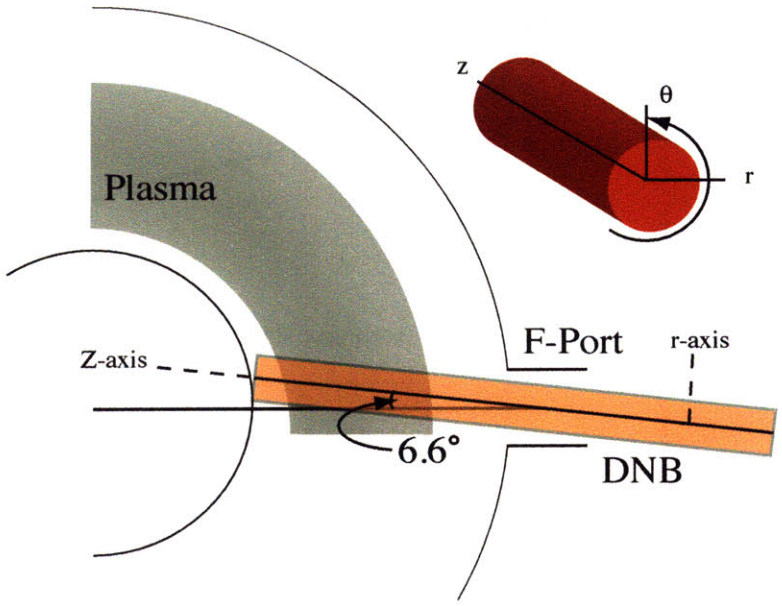

Figure 3-14: Geometry of diagnostic neutral beam used for calculating beam attenuation into the plasma

from the different energy components of the beam are easily distinguished from the thermal emission by their Doppler shifts. The relative intensities of the shifted lines, coupled with knowledge of the emission cross-sections, and neutralization efficiencies enables the determination of the relative current fractions in the beam. The emission cross-sections for H $+H_2$ are taken from reference [123] and the accuracy of the data is of order 10% for the full energy fraction and 5% for the lower energies [124].

The neutral beam density profile as a function of beam radius, r, and distance along the beam trajectory, z, (see Fig. 3-14) is given by

$$n_j(r,z) = \frac{I_j \eta_j}{v_j e \pi a^2(z)} exp\left(\frac{-r^2}{a^2(z)}\right), \tag{3.16}$$

where the subscript j refers to beam energy component, a is the beam 1/e half width, I_j is the beam current, and v_j is the velocity of the neutral particles. Equation 3.16 gives the profile of the DNB along its path if the divergence of the beam, $a(z)$ is known and the total particle flux is conserved. However, the condition on particle flux is not met due to the attenuation of the beam by the neutral gas in the beam line. Including this effect, the beam density is given by

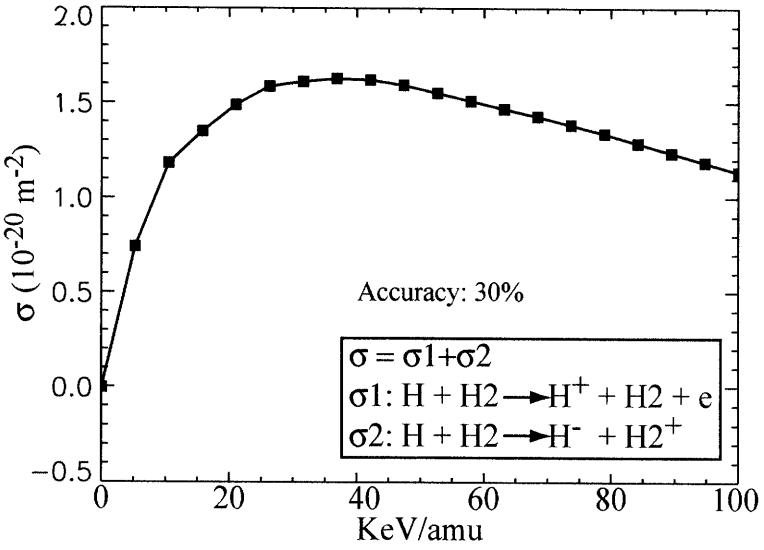

Figure 3-15: Stopping cross-sections for hydrogen on molecular hydrogen in the range of energies relevant for DNB attenuation

$$n_j(r,z) = \frac{I_j \eta_j}{v_j e \pi a(z)^2} exp\left(\frac{-r^2}{a(z)^2}\right) exp\left(-\int \left(n_{h_2}(z)\sigma_{(H+H_2)j}\right) dz\right). \tag{3.17}$$

Here n_{h_2} is the density of the neutral hydrogen gas and σ_{H+H_2} is the total cross-section for the interaction of the DNB neutrals with the molecular hydrogen gas. The relevant reactions are

$$H + H_2 \rightarrow H^+ + H_2 + e \tag{3.18}$$

$$H + H_2 \rightarrow H^- + H_2^+ \tag{3.19}$$

where the second is a 10% correction to the first at low energies. The cross-section for these reactions, shown in Fig. 3-15, were taken from reference [123] and are accurate to within 30%.

The neutral gas density profile between the calorimeter and the plasma can be calculated through the neutral pressure profile (shown in Fig. 3-13), and is divided into three regions: (P1) a linearly increasing pressure profile between the calorimeter and

the C-Mod vessel, (P2) a flat profile inside the C-Mod vessel up to the limiter radius, and (P3) an exponentially decreasing profile inside the plasma. The attenuation in sections two and three is actually by D_2 gas, not H_2. However, the cross-sections for $H+D_2$ will be very similar to those for $H+H_2$ especially for the high beam energies under consideration.

The neutral density before the calorimeter, P1, is of order 10^{-8} Torr, as a result of the strong pumping, and the data from the G-side pressure gauge is used to calculate the edge (P2) neutral density as a function time. The DNB attenuation by neutrals inside the plasma was found to be negligible because of the extremely fast decay of the neutral population at the C-Mod edge and is omitted in the calculation. Since the beam attenuation by neutrals inside the plasma edge is neglected, the beam profile obtained from Eq. 3.17 provides the initial condition, $N_{0,j}(r)$ for the attenuation of the DNB by the plasma.

The beam attenuation by neutral gas is shown in Fig. 3-17 as a function of edge neutral pressure. The edge pressure on C-Mod is typically between 0.01 and 0.5mtorr depending on the plasma density. These pressures results in neutral beam attenuation between 5 and 25% before the beam even enters the plasma. Towards the end of discharges, significantly higher edge pressures (>1mtorr) are not unheard of and result in beam attenuations up to 50% or more.

Once inside the plasma, the beam density is calculated according to

$$N_j(r,z) = N_{0,j}(r) exp\left(-\int \left(n_e(z)\sigma_{S_j}\right) dz\right), \tag{3.20}$$

where n_e is the electron density and σ_S is the effective beam stopping cross-section due to plasma interaction. The cross-sections used for this calculation are calculated via the Suzuki formulation [125], which gives an analytical expression for the total stopping cross-section as a function of plasma density, temperature, and Z_{eff}. The fits to the edge Thomson scattering temperature and density profiles and the average Z-effective measurement are used as input parameters and boron is assumed to be the dominant impurity in the plasma. The Suzuki parameterization of the cross-section

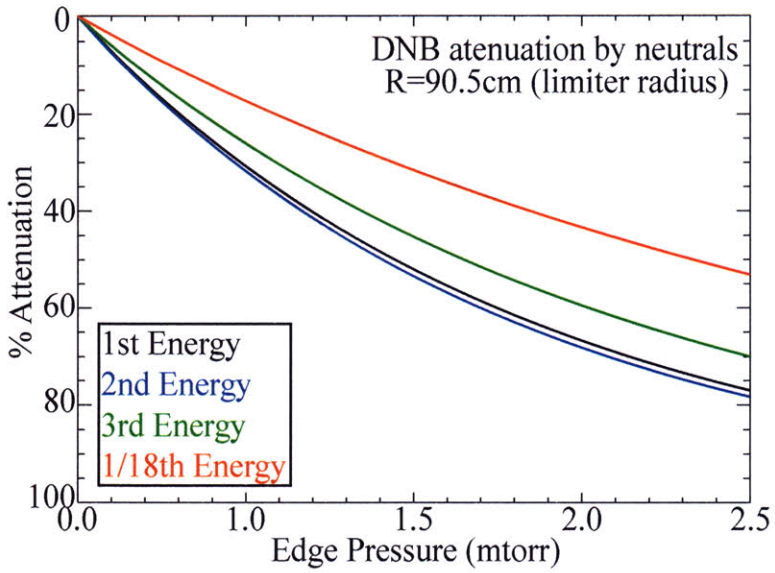

Figure 3-16: Attenuation of DNB energy components by neutral gas at the limiter radius (R=90.5cm)

fits the experimental data well. However, the uncertainty in the actual data used for the parameterization is between 10 and 30%. The uncertainties in the experimental data and theoretical cross-sections can be propagated into Eq. 3.20 to determine the uncertainty in the absolute neutral density in the plasma. The results of this propagation are shown in Fig. 3-18 for each of the four beam energy components. One should note, that the attenuation is only calculated at the center of the beam and the rest of the beam profile is assumed to have the same attenuation.

The calculated neutral densities are used to determine the boron density in the plasma through Eq. 3.10. The relative contributions of the different energy components to the measured charge exchange brightness depend not only on the density of the neutral population, but also on the effective emission rate for charge exchange with fully stripped boron into the n=7-6 line. The effective emission rates, shown in Fig. 3-19, used for the boron density calculations were taken from ADAS and include cascade radiation into the n=7 level from higher n-states. The uncertainty on this data is unknown, but is assumed to be of order 25%. The emission rates depend strongly on beam energy and only weakly on plasma density, temperature, and Z_{eff}. Due to the relatively weak dependence on plasma parameters the emission rates are

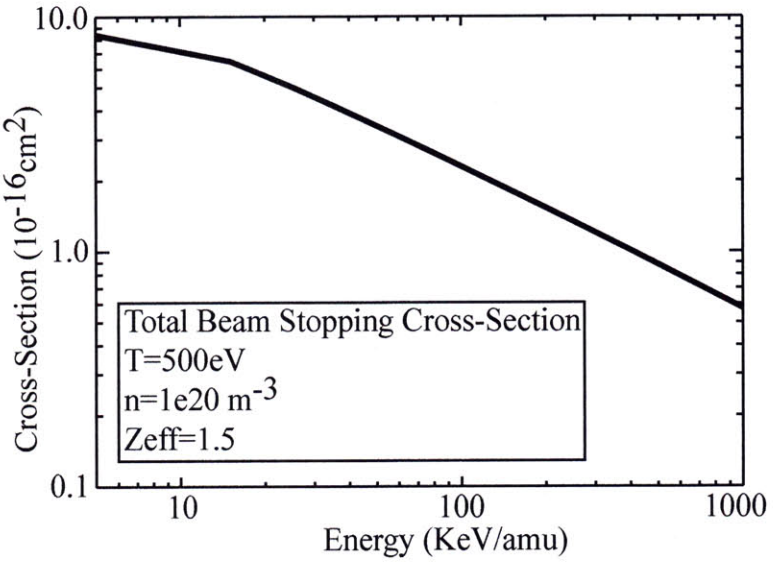

Figure 3-17: Total beam stopping cross-section according to the Suzuki formulation [125] for a hydrogen beam into a Deuterium plasma for T_e=500eV, n_e=1e20m^{-3} and Zeff=1.5

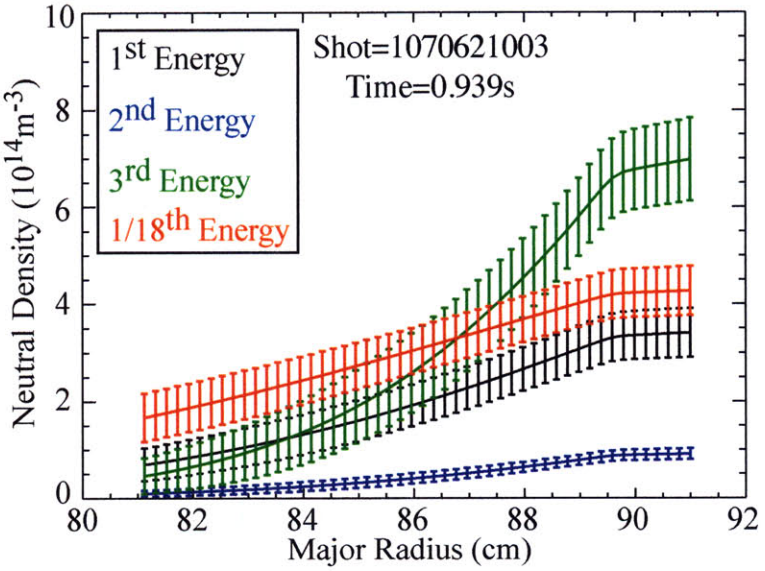

Figure 3-18: The attenuation of the individual beam energy components at the center of the DNB into an EDA H-mode plasma

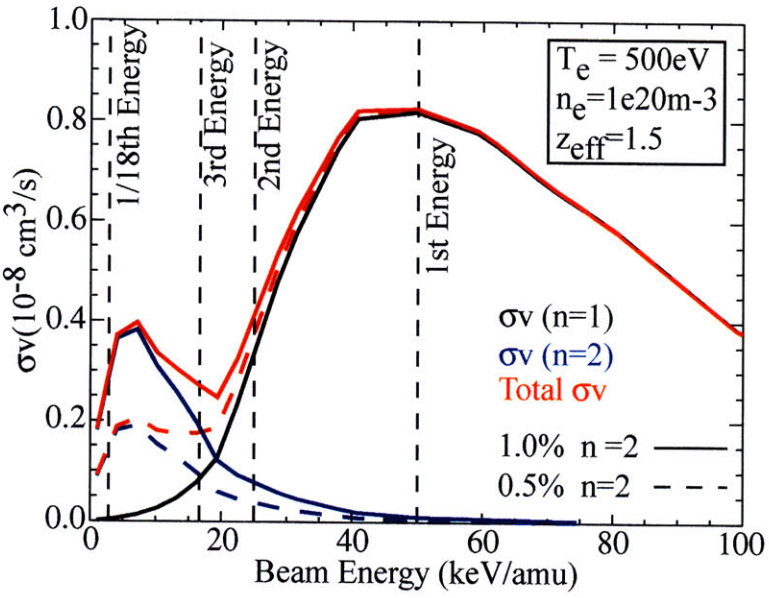

Figure 3-19: Effective emission rate for CX n=7-6

assumed to be constant over the LOS of the diagnostic through the DNB.

Most of the neutral particles in the DNB are in the ground state, however, a small but non-negligible fraction of the beam can be in an excited state. This small population in higher n-states can alter the effective emission-rate for the low energy components of the DNB as shown in Fig. 3-19. The lower energy components of the DNB are significant fractions of the total beam density and small changes in the neutral excited state population density (0.5%) can make significant alterations to the contributions to the total CXRS signal. This is shown in table. 3.2. Taking into account the energy population densities and the effective CX emission rate, the first energy component of the DNB is found to contribute between 40% (0.5% n=2) and 60% (1.4% n=2) to the total CXRS emission. The third and eighteenth energy fractions compose the rest of the signal, see tabe 3.2. The second energy population density it too small to contribute significantly to the total CX emission ($\sim$ 5%).

The current version of the CXRS density analysis code assumes a fixed 1% of the DNB is in the first excited state (n=2). However, work by the Texas CXRS group at C-Mod indicates that the n=2 excited state population fraction can be slightly higher than this and that the n=3 level can also give a non-neligible contribution [126, 127]. Calculations of the excited state density fractions in neutral beams have

Beam Component	0.5% n=2	1.0% n=2	1.4% n=2
1^{st}	60%	47%	40%
2^{nd}	5%	5%	5%
3^{rd}	20%	25%	27%
18^{th}	15%	23%	28%

Table 3.2: Beam energy component contributions to CXRS emission

been performed by Hutchinson for a wide range of plasma densities, temperatures, and beam energies [128]. The results of these calculations indicate that for typical C-Mod densities the n=2 population varies between 0.9 and 1.2% and the n=3 population is of order 0.5%. The underestimation of the second and third energy component contributions to the total CXRS emission can lead to boron densities that are too high by 20-30%. The extension of the current CXRS density code to include a detailed calculation of the relevant excited state fractions in the DNB is left as an exercise for a future C-Mod graduate student.

3.5 Data Analysis

To analyze charge exchange data the active signal must first be extracted from the background. There are many different ways this can be accomplished. The standard method on C-Mod is to temporally modulate the DNB and to assume that the charge exchange frames that do not fall in the beam pulses (background frames) are representative of the background during the beam pulse. The closest frames from both before and after a beam pulse are used to create mock-background frames for the time frames during the beam pulse (active frames). The mock frames are created by a pixel-by-pixel linear interpolation between the before and after background frames and the active charge exchange spectra is taken to be the difference between the active frame and its interpolated background. An example of this process is shown in Fig. 3-20A.

Alternatively, modulation of the neutral source is not necessary if separate background viewing chords are used to provide a measure of the background signal while the beam is on. This method is most useful when the background periscope's lines of

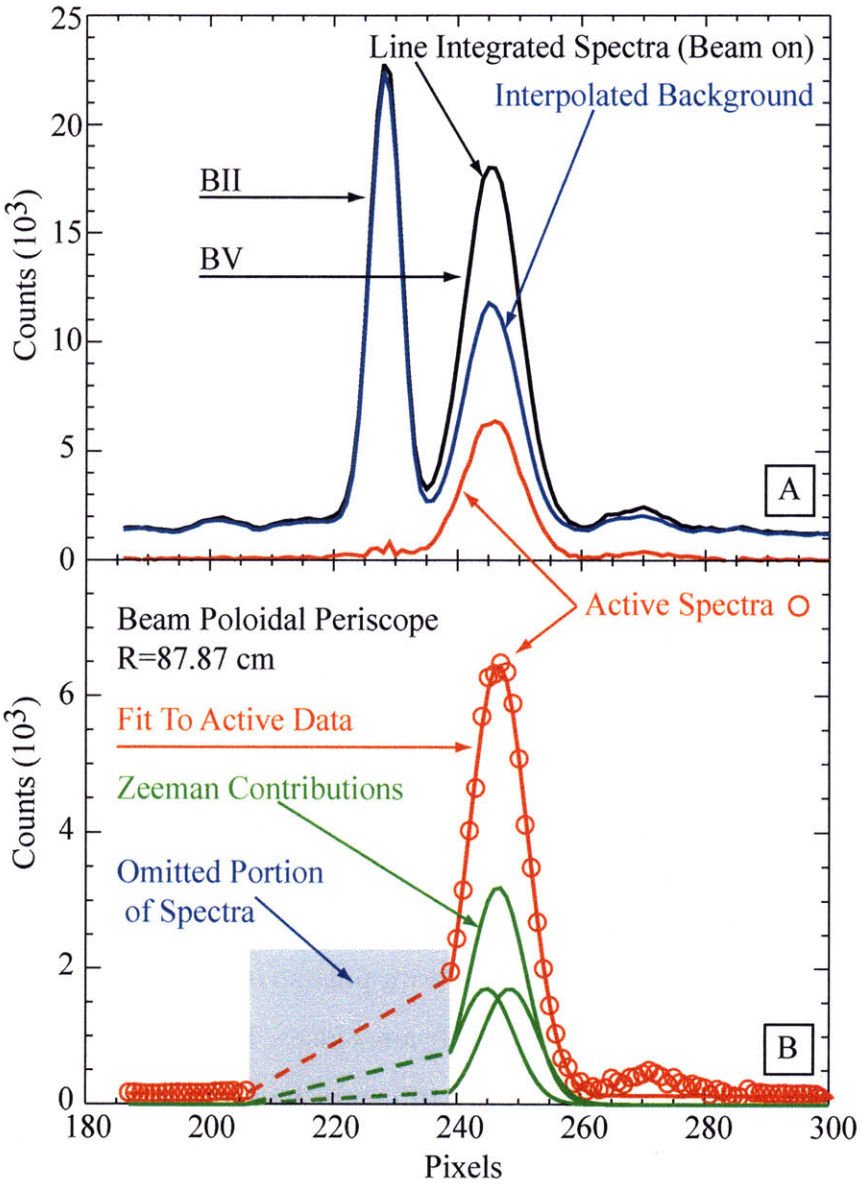

Figure 3-20: (A) Identification of the active charge exchange signal from the line integrated spectra by subtracting out an interpolated background spectra. (B) The fit to the obtained active spectra omitting the portion of the spectra that corresponded to the location of the BII line.

sight are a very close match to the lines of sight of the active view and the gradients of the relevant plasma parameters change slowly over the region of interest. Unfortunately for the edge CXRS diagnostic, the plasma gradients in the edge change very quickly, and it is extremely difficult to duplicate exactly the path of a viewing chord through the plasma down to the required millimeter scale. As such, despite considerable effort, the viewing chords of the background poloidal periscope do not mimic those of the active CXRS periscope well enough to translate the fitted backgrounds directly to the active data, especially in the pedestal region. Instead, a careful radial interpolation process of the poloidal background spectra is required before it can be used to extract the active charge exchange signal from the poloidal DNB viewing periscope's spectra. Even so, during periods of plasma discharges in which the background signal is evolving in a non-linear fashion, such as L-H transitions, this method can provide more accurate results than using a temporally interpolated background from the same periscope. As the toroidal periscope has no comparable background viewing chords, all toroidal background measurements are derived using the linear interpolation (in time) method.

There is an additional complication that arises when identifying the active charge exchange signal. Namely, the BV n=7-6 spectral line has a close neighbor in the BII line located at λ=4940.38A. The BII is usually more intense than BV and small errors in the interpolated (or fitted) backgrounds can cause a distortion to active spectra that manifests as an increased temperature and apparent velocity shift. For this reason, extra care is taken in fitting the active CXRS signal. The fitting code discriminates against the data points in the vicinity of the BII line by omitting a fixed wavelength region (that includes all of the BII line) from the final fit. Fig. 3-20B shows the accepted and omitted parts of an active CX frame from the beam poloidal periscope.

Once the active CX spectrum is obtained it must be fit to a functional form that correctly describes the population of emitting ions in order to derive any information from the spectra. As stated in section 3.1, if the ions have a Maxwellian distribution then the appropriate form to fit the spectra to is also a Maxwellian. However, there

are a number of different effects that can alter the shape of a spectra that would otherwise be a simple Maxwellian distribution. These effects must be included in the fit to the data and are discussed in sections 3.5.1 through 3.5.2.

The passive (background) spectra are also useful unto themselves as they provide radial profiles of line-averaged BV temperature, velocity, and brightness, which can give qualitative information about the plasma behavior. These profiles, thanks to higher signal levels, are less noisy than the active measurements, and extend across the LCFS into the scrape off layer. The BV population exists in a shell at the edge of the plasma and the portion of the radial profiles that exists outside of the peak in the emission layer can be considered marginally localized. Additionally, although not done routinely, the line integrated data could be inverted to provide localized profiles.

3.5.1 The Zeeman Effect on Charge Exchange Spectra

The Zeeman effect is the splitting of spectral lines that occurs when an atom is placed in a magnetic field. The so called 'normal' Zeeman effect treats the case when the net electron spin is zero and causes a splitting of a single line into three components, through the interaction of the magnetic field with the magnetic moment of the atom. Classically, the magnetic potential energy of the atom is given by

$$U(\theta) = -\mu \cdot B = \mu_z B \tag{3.21}$$

where z is the direction of the magnetic field and $\mu_z = -m_l \left(\frac{e\hbar}{2m_e}\right)$ is the magnetic moment of the atom. The potential energy splitting is then proportional to the magnetic quantum number m_l and is given by

$$\Delta U = m_l \left(\frac{e\hbar}{2m_e}\right) B. \tag{3.22}$$

Since there are $2l + 1$ values of m_l for each value of the orbital angular momentum number(l) each previously degenerate energy level breaks into $2l + 1$ energy levels. Although this means that a high l energy level will split into many more than three

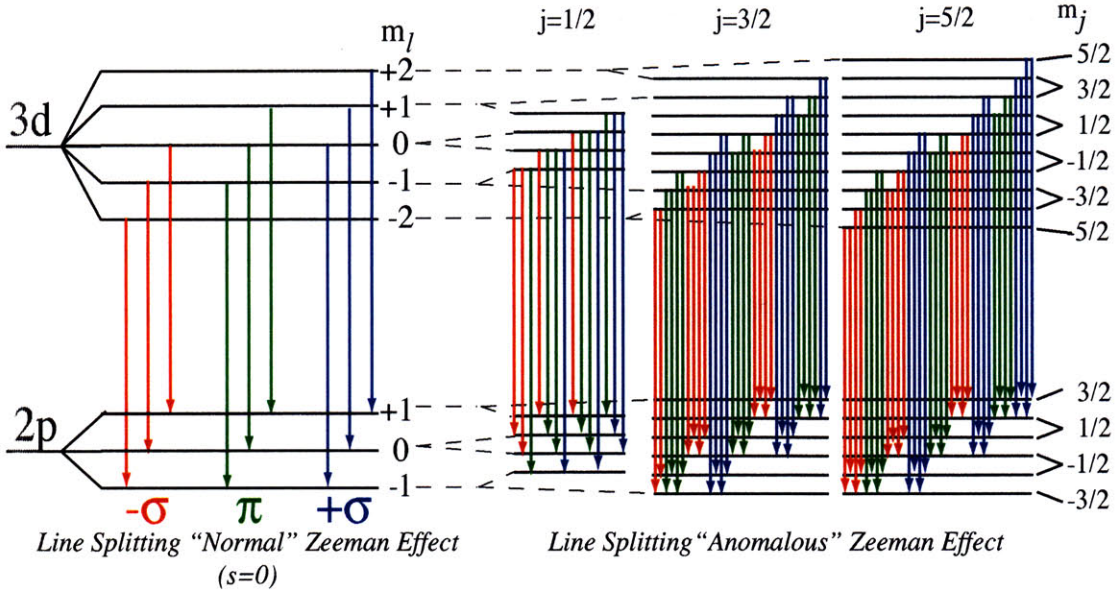

Figure 3-21: Left: 'Normal' Zeeman splitting of an n=4, l=3 to n=3,l=2 line. Right: 'Anomalous' Zeeman splitting of the same transition

levels, the spectrum only splits into three, due to the selection rules that govern transitions 3.23

$$\begin{aligned} \Delta l &= \pm 1 \\ \Delta m_l &= -1\ ,\ 0\ ,\ +1. \end{aligned} \tag{3.23}$$

Thus there are only three different energy levels for a given transition corresponding to Δm_l = -1, 0 , and +1. An example of this splitting for an n=4-3 and l=3-2 spectral line is shown on the left in Fig. 3-21. The splitting to the higher and lower energy levels result in the $\pm\sigma$ lines, while the $\Delta m_l = 0$ component gives the central (unshifted) π line 3-21. The observed intensity of these lines varies as a function of the observation angle to the magnetic field with the π component dominant for angles perpendicular to B, and the σ lines dominating for angles near parallel.

The so called anomalous Zeeman effect is a further splitting of the spectral line that occurs when the net spin of the electrons is non zero ($m_s = \pm\frac{1}{2}$) in either the initial or final state (or both). When this happens there is an additional spin component to the magnetic moment of the atom, which interacts with the the magnetic field

in equation 3.21 and alters the energy level splitting of the atom. In this case, the appropriate quantum numbers to consider are the total angular momentum number, j, defined by $\frac{1}{2} \leq j \leq n - \frac{1}{2}$, and the projection of j along a specified axis (usually along B) m_j, where $m_j = m_l + m_s$. The selection rules that govern the transition remain the same, see Eq. 3.23. As is clear from Fig. 3-21, the resultant splitting due to this effect can lead to significantly more distinct lines than the three from the normal Zeeman splitting.

The energy level splitting for the anomalous Zeeman effect is dependent upon the strength of the external magnetic field (B_{ext}) with respect to the internal magnetic field (B_{int}). In the rest frame of the electron the motion of the nucleus creates a current loop, which has an associated magnetic field given by the Biot-Savart law

$$\mathbf{B} = \frac{1}{4\pi\epsilon_0}\frac{Ze}{mc^2r^3}\mathbf{L}. \tag{3.24}$$

Here, $\mathbf{L}$ is the orbital angular momentum of the electron [129].

This internal field interacts with the magnetic moment of the orbiting electron and alters the energy levels of the system, an 'internal Zeeman effect'. This interaction is one of two mechanisms that together are known as the fine structure. The second mechanism is a relativistic correction to the kinetic energy of the electron due to its motion. The determination of the energy level splitting of the system will depend on whether or not the external field is greater than the internal. Using the Bohr formulation for the orbital energies and radii in Eq. 3.24 this gives an internal magnetic field of $\sim$0.5T for the n=7 level of boron. For C-Mod then the strong-field Zeeman limit, in which the Zeeman splitting dominates over the fine structure, is appropriate. In this limit the energy levels are given by

$$\begin{aligned} E_{n,m_l,m_s} &= E_Z + E_{FS} && (3.25)\\ &= \frac{-13.6eV}{n^2} + \mu_B B_{ext}\left(m_l + 2 \times m_s\right) && (3.26)\\ &+ \frac{13.6eV\alpha^2}{n^3}\left\{\frac{3}{4n} - \left[\frac{l(l+1) - m_l m_s}{l(l+1/2)(l+1)}\right]\right\} \end{aligned}$$

where α is the fine structure constant [129].

The total Zeeman pattern, which from here on will refer to both the Zeeman and the fine structure contributions, for the BV n=7-6 spectral line involves 710 lines, which should all be included in the analysis to correctly interpret the spectral shape. There are several methods of accounting for the Zeeman splitting in charge exchange spectra. First, there is the method of correction curves [130, 131, 132]. To apply this method one must assume that the total line shape of the spectra is Gaussian. This is only a valid assumption at high temperatures and low magnetic fields, where the Doppler broadening dominates over the Zeeman splitting. This is an acceptable assumption to make on many tokamaks, however, it is entirely inappropriate for the edge of Alcator C-Mod, where the magnetic field is large and the temperatures are quite low. However, the principle of the method is to calculate a complete Zeeman pattern for a matrix of magnetic fields and temperatures. The total pattern is then fit to a single Gaussian to obtain a database of apparent widths as a function of the field and the true temperature. The real charge exchange data is then fit to a single Gaussian and an interpolation process of the database is used to find the true temperature based on the apparent. The second method is to fit the active CXRS spectra to the complete Zeeman pattern for every single frame. Every line in the pattern would have to be convolved with the instrument function of the system making this method computationally intensive and time consuming. Luckily, there is a third alternative.

Parametrization of the Zeeman Effect: Method of Blom and Jupén

The complete Zeeman spectra can, to a large degree, be parameterized by its three polarization components ($-\sigma$, π, $+\sigma$) [131]. To do this, the complete Zeeman pattern for the transition of interest is calculated assuming statically distributed populations of the n and l levels [133] and the lines are grouped by their polarization. Each line in the pattern is a Gaussian with a width corresponding to the true temperature and since the lines are closely spaced, the total line shapes of the polarization components are also very nearly Gaussian. The intensities, locations, and widths of the three

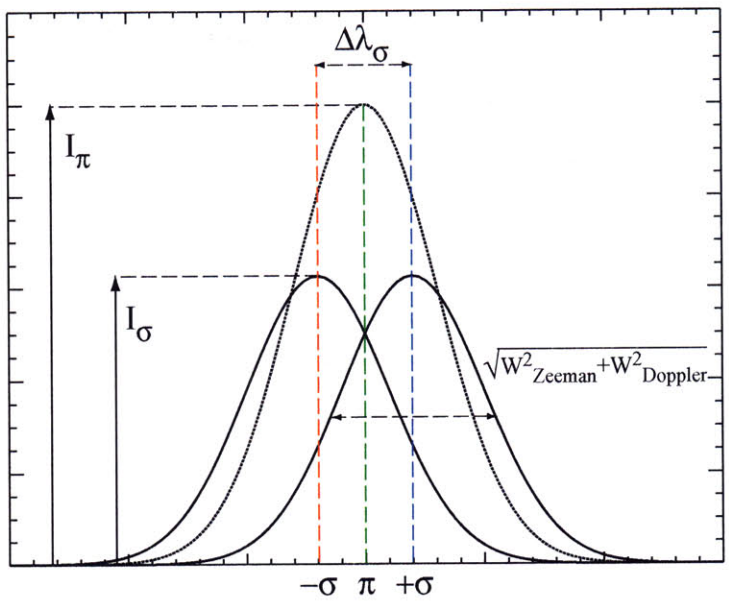

Figure 3-22: Parameterization of the Zeeman splitting by polarization components according to the method of Bom and Jupén[131]

components are determined by simple relations dependent upon the magnetic field and temperature. This parameterization of the Zeeman effect and the relations between the three components are illustrated in Fig. 3-22. From this point forward, the term 'Zeeman components' will be used to refer to the three polarization components rather than to the individual transitions in the complete pattern.

The width of each Zeeman component is contributed to by two effects: a broadening from the Zeeman splitting, W_{Zeeman}, and the true Doppler broadening, $W_{Doppler}$. The total fitted width of each Zeeman component is defined as

$$W_{fit} = \sqrt{W_{Zeeman}^2 + W_{Doppler}^2}. \tag{3.27}$$

and the relationship between W_{Zeeman} and $W_{Doppler}$ is found by plotting the ratio of the two widths as a function of ion temperature. In doing so, this ratio is found to fit well (to within a few percent) to the form

$$\frac{W_{Zeeman}}{W_{Doppler}} = \beta T^{\gamma}. \tag{3.28}$$

Here T is the ion temperature in eV and β and γ are fit parameters specific to

the transition. For the boron 4944.67A line these parameters are $\beta = 1.6546$ and $\gamma = -0.2941$. The uncertainty on these parameters, the fits, and in the determined temperature is of order 5%.

The ratio of the π to σ line intensities is dependent upon observation angle, θ, to the magnetic field. The relative intensity of the lines is given by

$$\frac{I_\pi}{I_\sigma} = \frac{2\sin^2\theta}{1+\cos^2\theta}, \tag{3.29}$$

The separation of the two σ peaks is proportional to the magnetic field and follows the energy level splitting expected from the normal Zeeman effect. The separation is given by

$$\Delta\lambda_\sigma = \alpha B. \tag{3.30}$$

where the parameter α is related to the energy of the specific transition and is given by

$$\alpha = \frac{\lambda_0^2 e}{2\pi c m_e}. \tag{3.31}$$

For the BV line of interest, α is equal to 0.228379 A/Pa.

The Blom and Jupén parameterization assumes that the σ lines are symmetric. However, this is not always the case. At sufficiently low temperatures the fine structure starts to become resolved outside of the Doppler broadening resulting in a small secondary feature on the blue side of the spectral line from the low l state contributions[131, 134]. According to Blom and Jupén if the spectra are fit to a single Gaussian (or symmetric Zeeman triplet) this will result in an apparent wavelength shift of the line to the red that can translate to an apparent velocity shift of up to several km/s. However, as the CXRS analysis on C-Mod discriminates against the blue side of the active signal due to the presence of the BII line (see Fig. 3-20), it is not clear how or if this asymmetry will affect the derived velocities.

If the Blom and Jupén analysis is used to estimate this additional error to C-Mod data then apparent velocity shifts between 4km/s and 0.3km/s are obtained for temperatures between 50 and 1000eV. Typical pedestal temperatures during EDA H-mode are of order 250eV, which results in a shift of 2km/s, going down to 1km/s

for a 400eV pedestal. The poloidal periscope, in forward field, would see an apparent shift in the ion diamagnetic direction meaning the true velocity is $\sim$ 2km/s greater in the electron direction. The opposite will be true when the magnetic field and plasma current are reversed. For the toroidal periscope the apparent shift is in the counter-current direction in forward field and co-current in reverse field.

All of the C-Mod active edge charge exchange data is analyzed using the Blom and Jupén parameterization. Each spectrum is fit in pixel space to the convolution of the appropriate three Gaussian instrument function with a three gaussian Zeeman spectra confined by the relationships described in equations 3.27 through 3.31. The true temperatures, velocities, and densities are then derived from the resultant fit parameters and the known calibrations of the spectrometer system. The low temperature asymmetry is not resolved by the system; the low temperature spectra still fit well to a symmetric Zeeman pattern with no discernible structure to the residuals outside of the noise.

3.5.2 Cross Section Effects on Charge Exchange Spectra

The observed charge exchange spectrum is dependent upon the direction of observation through the energy dependence of the charge exchange cross-section [135]. The spectrum is given by

$$f(v_z) = \int\int\int dv_x' dv_y' dv_z' \; g(v_x', v_y', v_z') \; \delta(v_z - v_z') \; Q(v_{col}), \tag{3.32}$$

where z is the direction of observation, $g(\vec{v})$ is the thermal velocity distribution of the ions, $v_{col} = |\vec{V} - \vec{V_b}|$ is the collision velocity for the reaction, δ is a delta function along the line of sight of the diagnostic and Q is the effective emission rate for the transition. The geometry under consideration is shown in Fig. 3-23. The beam trajectory lies in the y-z plane and θ is the angle between the beam velocity and the y-axis. The maximum angle, θ, for the toroidal periscope is of order 9 degrees and 4 degrees for the poloidal periscope. In this geometry the collision velocity is given by

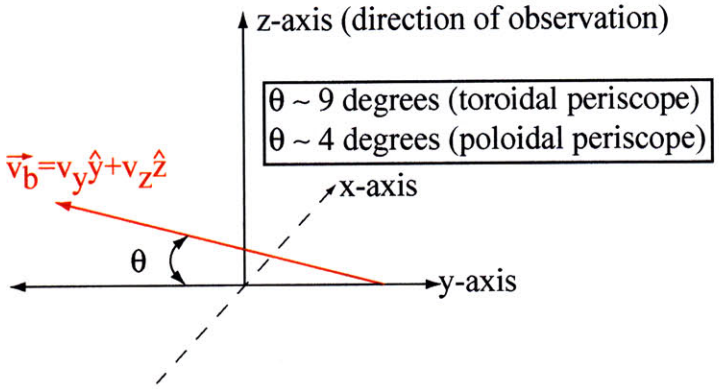

Figure 3-23: Geometry for calculation of the cross-section effects on the measured charge exchange spectra

$$v_{col} = \sqrt{v_b^2 + v^2 - 2v_b(v_y cos(\theta) - v_z sin(\theta)} \tag{3.33}$$

where v_b is the velocity of the beam neutrals.

At the edge of C-Mod the thermal velocity distribution, $g(\vec{v})$, is a Gaussian with a width corresponding to a few hundred eV and the emission rate, Q, is a much broader function of collision velocity, see Fig. 3-19. The integral over the product of g and Q determines the shape of the charge exchange spectrum. Note the spectrum's dependence on geometry through Q's dependence on v_{col}. If Q is flat in the vicinity of the beam velocity, as is the case for the first and third energy components of the DNB, then the shape of the CX distribution would be unchanged from a standard Gaussian. However, if Q has some slope in this region (second and eighteenth beam energies) then this will manifest itself as a shift in the observed spectrum and the curvature of the emission rate will alter the apparent temperature. Equations for the true temperature and velocity as a function of the system geometry and the observed temperature and velocity are derived in detail in reference [135] and won't be reproduced here. The C-Mod CXRS systems have nearly perpendicular viewing geometries and of order 80% of the CXRS brightness come from the first and third beam energy components. These two effects together minimize the alteration to the charge exchange spectrum due to cross-section effects. The corrections to the observed temperatures and velocities for the toroidal periscope are shown in Fig. 3-24 for the

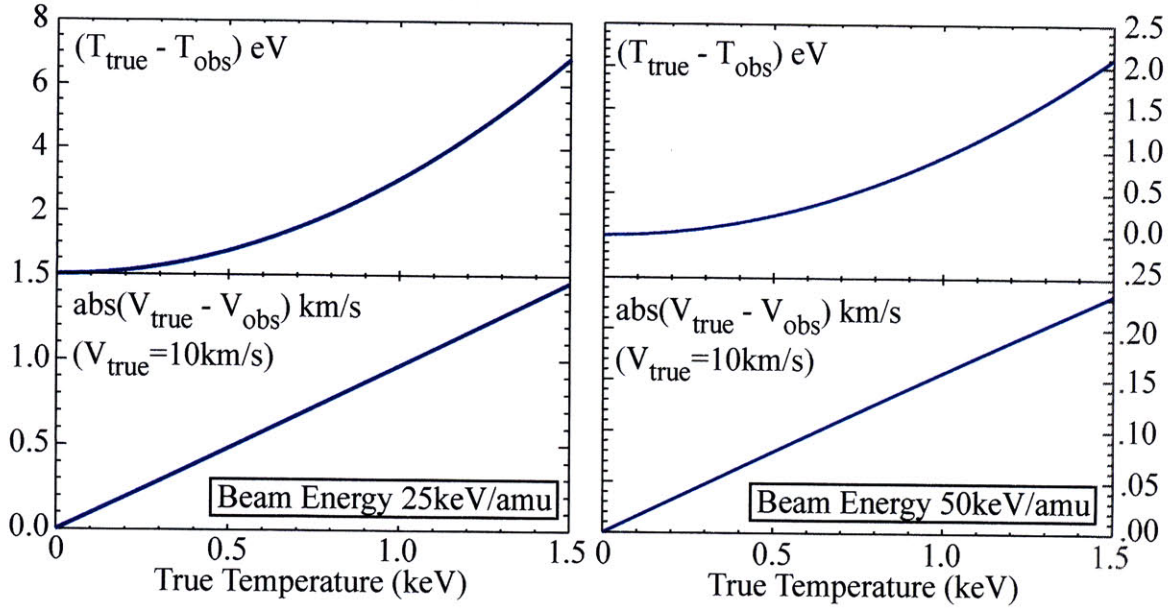

Figure 3-24: Corrections to observed charge exchange temperatures and velocities due to energy dependent cross section effects for the C-Mod CXRS system

first and second energy components of the DNB and are well within the error bars of the measurement for both cases.

3.5.3 Uncertainties in CXRS Measurements

There are several different sources that contribute to the uncertainties in charge exchange measurements some of which have already been discussed in previous sections of this chapter. The radial resolution of the diagnostic is set by the lines of sight of the periscopes and the magnetic topology. The spectrometer calibrations set limits on the minimum uncertainty for temperature and velocity measurements and the Zeeman parameterization used to analyze the CX data introduces additional uncertainties on these parameters. The uncertainties in the brightness calibration, neutral density calculation, and effective CX emission rate calculation control how well the absolute boron density can be known. Lastly, there are uncertainties inherent to the fitting process due to the photon statistics associated with the spectra and the presence of a distribution of background photons. These statistical uncertainties represent the minimum uncertainties achievable through the line fitting process and can be calcu-

lated without fitting the line shape provided that knowledge of the CX signal and background distributions are available [136].

In the section that follows uncertainties will be represented by δ and all widths, W_y, represent standard deviations of their corresponding distributions y. Standard deviations are defined in the usual way, namely, as the square root of the sample variance S_y^2

$$S_y^2 = \frac{1}{N-1}\sum_{i=1}^{N_y}(x_i - \bar{x_y})^2 . \tag{3.34}$$

Here, $\bar{x_y}$ is the mean of distribution y and N_y is the total number of photons. For the case of a Gaussian distribution, as is most applicable here, the standard deviation of the distribution, W_y is defined according to

$$G_y(x) = \frac{1}{W_y\sqrt{2\pi}} \exp\left[\frac{1}{2}\left(\frac{x-\bar{x_y}}{W_y}\right)^2\right] \tag{3.35}$$

Note, that the doppler width, W_D, as defined in Eq. 3.5 is already of this form, as are the instrument function widths, W_I, which were defined in Eq. 3.15.

The statistical uncertainties in the width and mean of an arbitrary photon spectra in the presence of a background distribution with the same mean are given by

$$\delta_w = \frac{W_{SIG}}{\sqrt{2N_{SIG}}}\sqrt{1 + \frac{W_{BCK}^4 N_{BCK}}{W_{SIG}^4 N_{SIG}}} \tag{3.36}$$

and

$$\delta_\mu = \frac{W_{SIG}}{\sqrt{N_{SIG}}}\sqrt{1 + \frac{W_{BCK}^2 N_{BCK}}{W_{SIG}^2 N_{SIG}}} \tag{3.37}$$

where W_{SIG} and W_{BCK} are the measured standard deviations of the signal and background distributions and N_{SIG} and B_{BCK} are the number of photons in each [136].

The total uncertainty in the velocity measurements will be proportional to the sum of the squares of the uncertainty from the wavelength calibrations, δ_λ, and from photon statistics, δ_μ (Eq. 3.37), plus an additional temperature dependent uncertainty, $\delta_T(T_i)$, from the cross-section and fine structure effects discussed in sections 3.5.1 through 3.5.2. The total uncertainty is then

$$\delta_V = \frac{c}{\lambda_0}\sqrt{\delta_\lambda^2 + \delta_\mu^2} + \delta_T(T_i). \tag{3.38}$$

Similarly, the uncertainty in the temperature will have a contribution from the instrument functions, the photon statistics, and the uncertainties in the Zeeman parameterization. The contribution from the cross-section effects is less than 1eV (Fig. 3-24) and is neglected here. The measured width of the spectra (W_M) has contributions from the instrumental width (W_I) the Doppler width (W_D) and the Zeeman width (W_Z)

$$W_M^2 = W_I^2 + W_D^2 + W_Z^2. \tag{3.39}$$

Rearranging and using Eqn. 3.28 we have

$$W_D = \left(\frac{W_M^2 - W_I^2}{1 + A^2}\right)^{\frac{1}{2}} \tag{3.40}$$

where A is the ratio of the Doppler width to the Zeeman width. The uncertainty in the measured width, δ_M, is given by Eq. 3.36. The uncertainty from the instrument functions, δ_I, is typically small as the width of the instrument functions can be known very accurately ($\delta_I < 5\% W_I$). Lastly, the uncertainty in the ratio A, as stated in section 3.5.1, is of order 5%. The uncertainty in the Doppler width is found by propagating all of these uncertainties in Eq. 3.40 yielding

$$\delta_D = \frac{W_D}{W_M^2 - W_I^2}\left[\delta_M^2 W_M^2 + \delta_I^2 W_I^2 + \delta_A W_D^4 A^2\right]^{\frac{1}{2}} \tag{3.41}$$

The uncertainty in the temperature is then

$$\delta_T = \delta_D \frac{2 m_i c^2 W_D}{\lambda_0^2}. \tag{3.42}$$

If the wavelength and instrument calibrations are done properly then the uncertainty due to photon statistics dominates the error. Velocity measurements can typically be made to within ±2km/s and temperature measurements to within ± 20-50eV with sufficient signal.

The uncertainty in the boron density measurement is dependent on the uncertainty of the brightness calibration and the fitted area under the spectral line (δ_ϵ), as well as the uncertainty in the effective emission rate (δ_Q), and the neutral density calculation, (δ_{n0}). Altogether, the uncertainty in the density measurement is given by

$$\delta_{n_i} = \sum_k \sum_j \left(\frac{4\pi \epsilon^{\lambda}_{CX,j,k}}{\sum_j \langle \sigma\nu \rangle^{\lambda}_{j,k} \int n_{0,j,k} dl} \right) \left[\left(\frac{\delta_{\epsilon_{j,k}}}{\epsilon^{\lambda}_{CX,j,k}} \right)^2 + \left(\frac{\delta_Q}{\langle \sigma\nu \rangle^{\lambda}_{j,k}} \right)^2 + \left(\frac{\delta_{n_{0,j,k}}}{\int n_{0,j,k} dl} \right)^2 \right]^{\frac{1}{2}} \tag{3.43}$$

and is typically between 40 and 50%. The uncertainty on the shape of the profile is considerably smaller as the uncertainties in the neutral attenuation, the emission rate, and the brightness calibration do not not affect the overall shape of the profile.

Chapter 4

CXRS Measurements of Pedestal Structure and Behavior

This chapter presents the initial flow, temperature, and density results from the new edge CXRS diagnostic. The behavior of these parameters will be explored in a variety of plasma regimes including ohmic L-mode, ELM-free H-mode, EDA H-mode and I-mode. When possible these results will be compared to measurements from other diagnostics on C-Mod. The majority of the CXRS data shown here is from the beam poloidal and toroidal periscopes and so represent the plasma behavior at the mid-plane on the low field side (LFS) of the tokamak. The only exception to this are the temperature profiles, which also include data points from the high field side (HFS) toroidal periscope (see section 3.2.1).

The toroidal velocity sign convention is defined in a top down view of C-Mod. Velocities in the clockwise direction are considered positive (forward field, co-current direction) and counter clockwise flows are negative. Similarly, poloidal velocities that are vertically upward at the low field side (forward field, electron diamagnetic direction) are positive, and vertically downward velocities (forward field, ion diamagnetic direction) are considered negative. These conventions, shown in Fig. 4-1, do not alter when the magnetic field and plasma current directions are switched and will employed throughout this thesis.

The CXRS temperature and density profiles are typically fit to the same modified

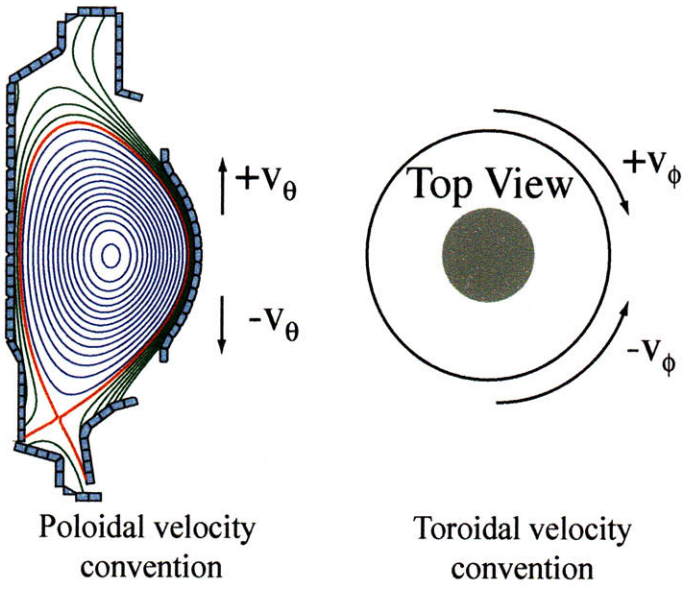

Figure 4-1: Sign convention for the velocities measured by the edge CXRS diagnostic

tanh function that is used to describe the Thomson scattering data [5]. The function is given by

$$f(R) = b + \frac{h}{2}\left[\tanh\left(\frac{R_0 - R}{d}\right) + 1\right] + m\,(R_0 - R - d)\,H\,(R_0 - R - d) \qquad (4.1)$$

where b is a baseline offset, h is the pedestal height, R_0 is the pedestal location, d is the half width, m is the slope of the fit inside the pedestal, R is an array of mid-plane radii and $H(x)$ is a discrete heaviside function. This form was chosen to facilitate the comparison between the edge electron and impurity ion profiles. In H-mode and I-mode plasmas this function describes both the CXRS density and temperature profiles well and is employed in the data analysis. However, in L-mode plasmas the edge gradients are typically not steep enough to fit well to this form. When this happens the profiles are fit to a second order polynomial instead.

4.1 Alignment of Temperature Profiles

The boron temperature profiles presented in this chapter utilize data from both the LFS CXRS periscopes and the HFS toroidal periscope. To do this the radial locations

of the HFS profiles are mapped along flux surfaces to the low field side using the EFIT magnetic reconstruction of the plasma. However, in doing so the LFS and HFS temperature profiles do not always radially align. The disagreement between the profiles is often small (1-2mm), but can be of order half a centimeter, which is outside the error bars of both the LFS and HFS periscopes spatial calibrations. The mapped HFS profiles are usually displaced outside of the LFS measurements (larger major radii). The uncertainty in the EFIT mapping is not well characterized, but the radial errors could easily be several millimeters. Since the temperature of a given species is constant on a flux surface, the radial discrepancy between the profiles is attributed to EFIT mapping errors and the HFS temperature profiles are manually shifted to align with the LFS data. This procedure has been used for all of the boron temperature profiles presented in this thesis.

A similar mapping uncertainty is encountered when comparing the CXRS boron temperature profiles (T_B) to the Thomson scattering electron temperature profiles (T_e). The T_e profiles are measured along a vertical chord passing near the center of the plasma and the mapping from the top of the plasma to the corresponding mid-plane positions is again determined using EFIT. Examination of the T_B and T_e profiles show that in all plasma regimes the profiles are similar in both shape and magnitude. This will be shown explicitly in subsequent sections of this chapter. However, these profiles can also be shifted radially from one another outside the spatial error bars of the CXRS and the TS diagnostics. The electron temperature profiles are on average displaced by 3mm outside of the boron temperature profiles, although shifts of up to 6-7mm have also been observed. Due to the similarity in appearance, it is very tempting to shift the T_e profiles so that they align with T_B. However, the answer to the question, "Should the electron and boron temperatures be equal on a flux surface?" or "Are the profiles *supposed* to be shifted with respect to one another?" is not clear.

To properly address this question requires a two dimensional analysis of the coupled ion and electron energy transport in both the plasma and in the SOL, which is beyond the scope of this thesis. In this work, it has been assumed that the T_e profile

should align with T_B and both the TS density and temperature profiles have been shifted accordingly. A qualitative discussion on why these profiles should be aligned is given below [137].

In a slab model the energy transport equations are of the form

$$\frac{\partial}{\partial t}\left(\frac{3}{2}n_\alpha k T_\alpha\right) = \sum_\beta k n_\alpha \left(T_\beta - T_\alpha\right)\nu_{\alpha\beta} + Q - \frac{3}{2}n_\alpha k \chi_\alpha \left[T_\alpha \frac{\partial}{\partial r}\lambda_{T_\alpha}^{-1} + \lambda_{T_\alpha}^{-1}\frac{\partial}{\partial r}T_\alpha\right]. \quad (4.2)$$

Here, the subscripts α and β denote species, n and T are the density and the temperature, k is Boltzman's constant, Q is an external energy source (i.e. ICRF), $\nu_{\alpha\beta}$ is the thermal collision frequency for α on β, χ is the thermal diffusivity and λ_T is the temperature gradient scale length ($\lambda_x = x/\nabla_x$). In Eq. 4.2 the density and thermal diffusivity have been assumed to be approximately constant and so were not included in the divergence of the heat flux. This is a poor assumption in the edge pedestal. However, making the assumption simplifies the analysis and does not affect the final the result. In steady state the time derivative goes to zero and at the edge of the plasma there are no external heat sources. Therefore, the energy transport equation for the boron population simplifies to

$$\left(T_e - T_B\right)\nu_{Be} + \left(T_i - T_B\right)\nu_{Bi} = \frac{3}{2}\chi_B\left[T_B\frac{\partial}{\partial r}\lambda_{T_B}^{-1} + \lambda_{T_B}^{-1}\frac{\partial}{\partial r}T_B\right]. \quad (4.3)$$

Here, only the main ion, electron, and boron populations have been included in the analysis. In equation 4.3 the unknowns are T_i, χ_B, and the radial shift between the electron and boron temperature profiles. However, the order of magnitude of the diffusion coefficient can be estimated using a χ based on global power balance

$$\chi \simeq \frac{P_{LCFS}}{3n_e\nabla\left(T_e\right)}, \quad (4.4)$$

where P_{LCFS} is the power crossing the LCFS. If this is used in place of χ_B then Eq. 4.3 can be evaluated using both shifted and unshifted profiles to find the maximum allowable deviation between the ion and boron temperature profiles. Rearranging Eq.

4.3 to solve for T_i gives

$$T_i = \left(\frac{3}{2}\chi_B\left[T_B\frac{\partial}{\partial r}\lambda_{T_B}^{-1} + \lambda_{T_B}^{-1}\frac{\partial}{\partial r}T_B\right] - (T_e - T_B)\,\nu_{Be}\right)\tau_{Bi} + T_B. \tag{4.5}$$

Here τ_{Bi} is the boron ion thermal equilibration time. If τ_{Bi} is sufficiently small compared to the terms in parenthesis then the boron and main ion temperature profiles can not deviate significantly from one another inside the LCFS. This calculation has been performed using both shifted and unshifted profiles from a variety of plasma regimes with the universal result that the thermal equilibration between the main ions and the boron dominates over the other terms. In ELM-free H-modes, however, this analysis is less applicable as the plasmas are not steady state and the time derivative of the energy cannot be ignored.

The input parameters and results of this calculation for an EDA H-mode plasma are shown in Fig. 4-2. Panels A and B show the inputted boron (red) and electron (blue) temperature and density profiles for the case where the TS profiles have not been shifted. Panel C shows the resultant main ion temperature profile from Eq. 4.5 (green) compared to the measured T_B profile. Panels D-F shows the same information for the case when the TS profiles are shifted by 3mm inward to align the electron and boron temperature profiles. In both cases the main ion temperature profile is found to be nearly identical to the boron profile. The radial shift of the TS and CXRS temperature profiles is negligible in this analysis because the ion-boron thermal equilibration is much faster than the electron-boron equilibration. The deviation between the boron and main ion profiles in the pedestal region is caused by the cross-field transport terms and is well within the error bars of the measurement. In addition, this result does not change significantly when the thermal diffusivity is varied within reasonable parameters ($0.1 < \chi\,(m^2/s) < 1.0$). This indicates that the measured boron temperature profiles inside of the LCFS can be trusted to represent the main ion species.

If the EFIT determined location of the electron temperature profile is correct then the main ion temperature is significantly lower than the electron temperature at the

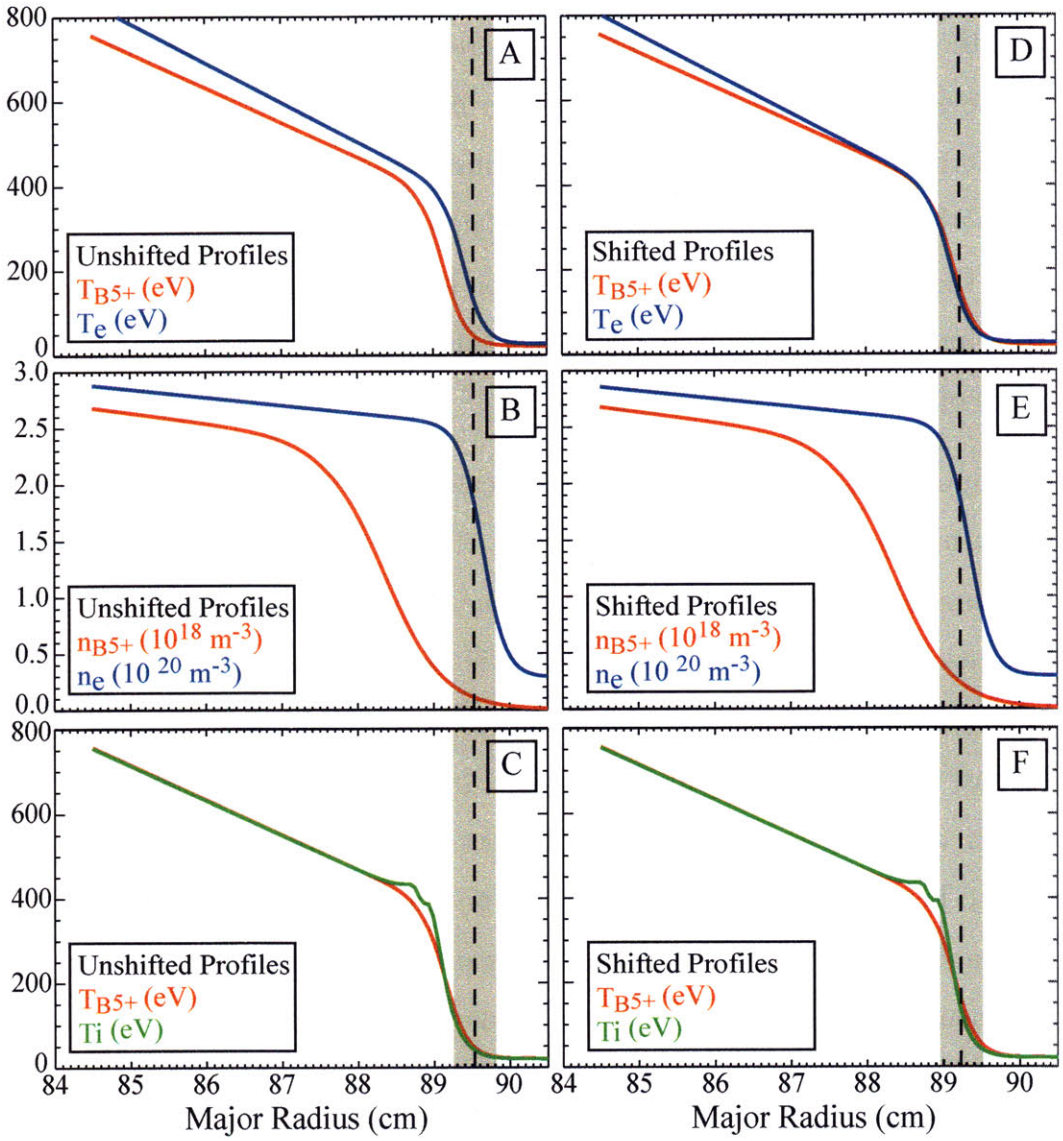

Figure 4-2: Estimation of the main ion temperature profiles based on measured electron and boron profiles (shot=1070621003, T=0.9s)

LCFS. On the other hand, if the EFIT mapping is wrong then the relative alignment of the T_e and T_i profiles is unknown. Unfortunately, with the information available there is no way to determine whether or not the profiles should be aligned without making assumptions about the energy transport.

C-Mod plasmas are heated using a combination of ohmic and ICRF power. The ohmic power heats the electrons exclusively and can be a non-negligible contribution to the total heating power in standard discharges. The ICRF power heats the minority ions in the plasma. These ions, if below the critical energy ($\sim 15 T_e(eV)$), slow down mainly on plasma ions and above the critical energy slow down on the electrons. For standard H-mode discharges, the total heating power is fairly well divided between the main ion and electron populations [138]. This is consistent with the measurements of the impurity ion (Ar) and electron temperature profiles in the core, which are observed experimentally to be very similar [139].

The thermal equilibration time between the main ions and the Ar in the plasma core is very fast compared to the local transport time scales. This indicates that in this region the Ar temperature profiles are also representative of the main ion population. Because the amount of heating power deposited into the ion and electron populations is of the same order and the temperature profiles of these two populations are observed to be very similar, the heat transport (power flux) in these two channels must also be very similar. This indicates that the ion and electron temperature profiles cannot deviate significantly from one another in the core of the plasma and out to the top of the pedestal. In the steep gradient region, however, the transport is not understood and the relative alignment between the ion and electron pedestals is unclear.

In the SOL if the power flux in the ion and electron channels is still approximately the same then the ion temperature cannot be lower than the electron temperature (as is the case for unshifted profiles). This result comes about through power balance in the SOL. On open field lines the heat sink for the electrons is significantly larger than for the ions, which means the electrons can lose their heat much faster than the ions, particularly via parallel conduction. This argues that the ion temperature in

the SOL must be at least equal to if not greater than the electron temperature. The amount of power flowing across the LCFS into the SOL in the ion channel relative to the electron channel is unknown. However, as argued previously, the ion and electron power fluxes at the top of the pedestal must be similar and it is reasonable to expect that they will also be of the same magnitude at the bottom of the pedestal. When the TS data is radially shifted to comply with the profile constraints both in the plasma and in the SOL then the T_e pedestal is found to align radially with T_B.

4.1.1 Position of the LCFS

In this thesis plasma profiles are plotted as a function of distance from the LCFS. However, the actual location of the LCFS is a matter of some debate, as the position reported by EFIT often does not make physical sense in light of power balance considerations. Under the assumption that T_i is equal to T_e the majority of the power crossing the LCFS is carried by means of the electron parallel heat conduction[140]. Given these assumptions a relationship between the temperature at the LCFS (T_0) and the power crossing into the SOL (P_{SOL}) can be found. Following the derivation in reference [141] the total power density into the SOL, $S(W/m^3)$, can be written as

$$S = -\nabla_\perp \cdot q_\perp = \nabla_\parallel \cdot q_\parallel. \tag{4.6}$$

Here, $q_\perp$ is the perpendicular heat flux crossing the LCFS, and $q_\parallel$ is the parallel heat flux in the SOL. The parallel heat flux is given by the Spitzer and Härm expression [140, 141]

$$q_\parallel = -\kappa_0 T_e^{\frac{5}{2}} \nabla_\parallel T = -\frac{2}{7}\kappa_0 \nabla_\parallel T_e^{7/2} \tag{4.7}$$

where κ_0 is a constant given by

$$\kappa_0 = \frac{(4\pi\epsilon_0)^2}{m_e^{1/2} \ln \Lambda e^4 Z}. \tag{4.8}$$

From Eq. 4.7 the total power density can be written as a function of the electron temperature along a field line

$$S = \frac{4\kappa_0}{7l^2}\left(T_u(\rho)^{7/2} - T_d^{7/2}\right) \tag{4.9}$$

Here l is the distance along a field line to the diverter, which can be estimated as a parallel connection length ($l \simeq \pi q R_0$), T_d is the diverter temperature and the flux surface (ρ) dependence of the up-steam temperature (T_u) has been written explicitly. If the upstream temperature is at least a factor of two higher than the diverter temperature then, thanks to the 7/2 power, the T_d dependence can be neglected. The power density in Eq. 4.9 can then be used in Eq. 4.6 and both sides integrated over the SOL volume to relate P_{SOL} to T_0.

$$A\int_0^\infty (-\nabla_\perp \cdot q_\perp)\, d\rho = P_{SOL} = \frac{A4\kappa_0 T_0^{\frac{7}{2}}}{7\pi^2 q^2 R_0^2}\int_0^\infty \exp\left(-\frac{7\rho}{2\lambda_T}\right)d\rho. \tag{4.10}$$

In Eq. 4.10 A is the area of the LCFS, λ_T is the temperature gradient scale length in the SOL and an exponential form for the $T_u(\rho)$ has been assumed. Solving for the temperature at the LCFS we find

$$T_0 = \left(\frac{49\pi^2 R_0^2}{8\kappa_0}\frac{q^2 P_{SOL}}{\lambda_T A}\right)^{\frac{7}{2}} \tag{4.11}$$

For L-mode plasmas Eq. 4.11 typically gives T_0 between 50 and 70eV. In ICRF heated H-mode plasmas T_0 can reach 130eV $\pm$ 15eV. However, these differences in temperature do not significantly impact the location of the LCFS if the edge temperature profile is sufficiently steep. Consider the EDA H-mode temperature profile shown in Fig.4-3. The possible range in T_0 (50-150eV) gives a range in radial location of only ~3mm. The error in the radial location of the tanh fits to the temperature data is of the same order (~2mm). For plots of H-mode and I-mode profiles the position of the LCFS has been chosen to align with the 100eV point on the temperature profiles and the uncertainty in this location is of order $\pm$2mm. For L-mode plasmas, the position of the LCFS has been aligned with the 50eV point on

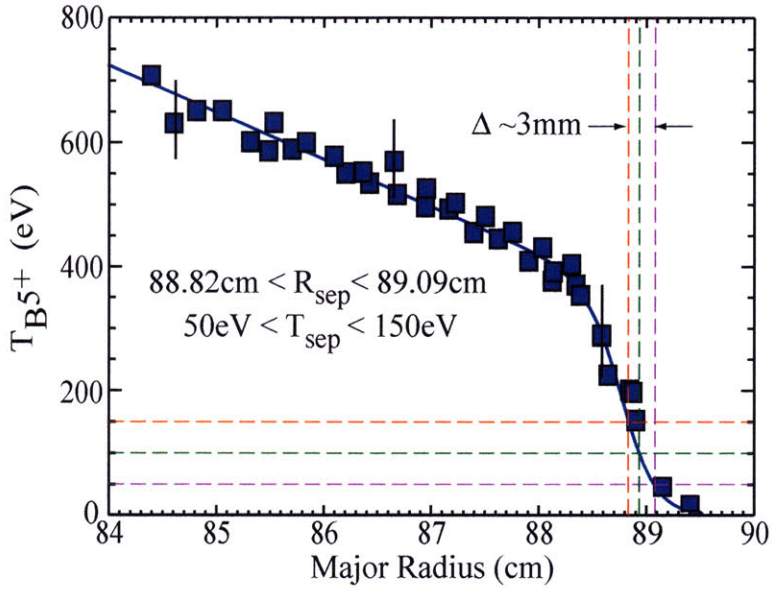

Figure 4-3: Position of LCFS with respect to the B^{5+}temperature profile in an EDA H-mode

the temperature profile.

4.2 CXRS Results in Ohmic L-mode Plasmas

CXRS measurements are difficult to make in ohmic L-mode plasmas. This is because the boron density is so low that individual time frames (5ms) do not have enough active signal to make a clean measurement. To obtain L-mode profiles it is usually necessary to add together multiple active time frames from steady state portions of the discharge until sufficient signal to noise is obtained. All of the profiles shown in this section were obtained by this method. In Ohmic L-mode plasmas the toroidal rotation profiles, shown in Fig. 4-4, are always co-current at the edge and become more counter current further into the plasma. Near the LCFS the rotation decreases in the counter current direction, but does not actually change sign. This is true in LSN and USN and in both forward and reverse field plasmas. These measurements are consistent with both core and SOL layer flow measurements. The core toroidal rotation measurements are in the counter-current direction during Ohmic L-mode discharges [7] and LFS probe data show that main ion flows in the low field side SOL

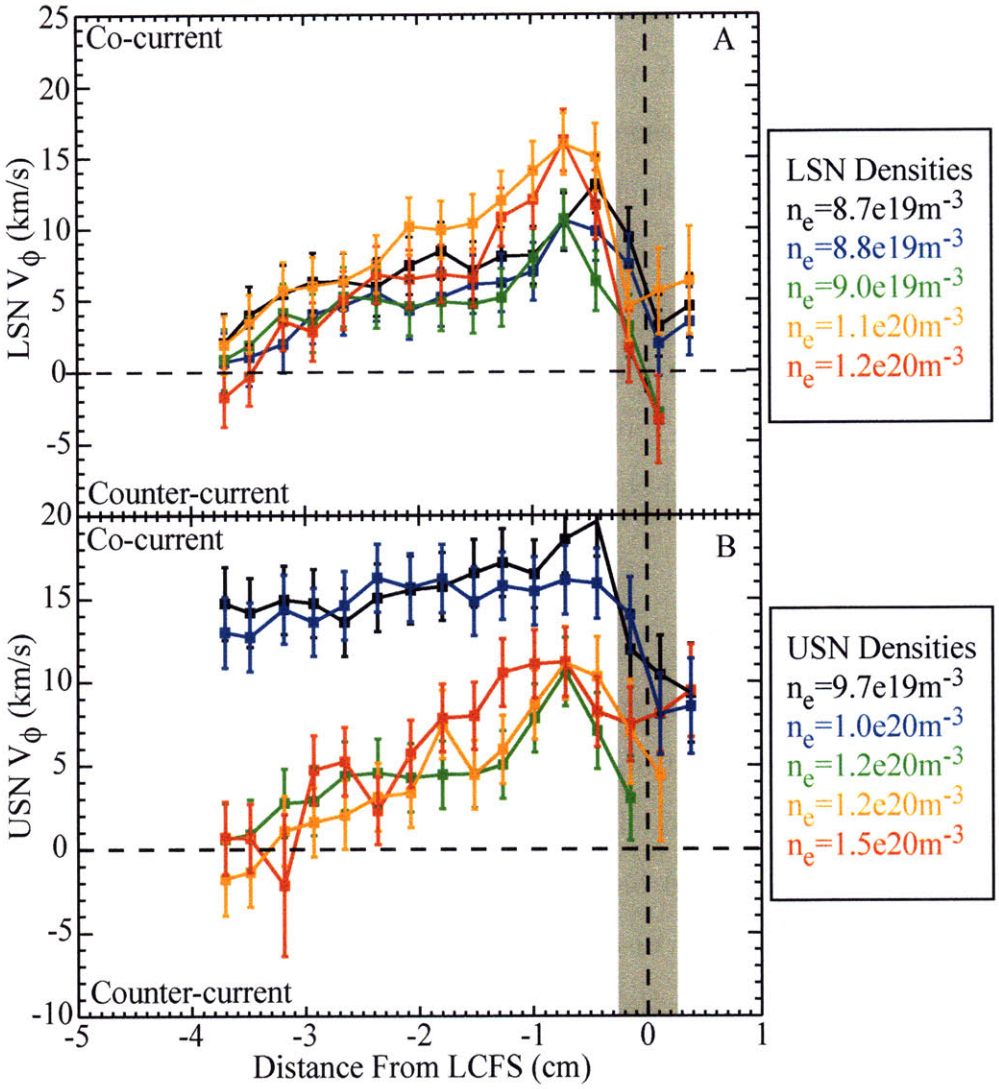

Figure 4-4: Edge BVI toroidal rotation profiles and their dependence on plasma density in LSN (A) and USN (B) discharges (Run 1070627)

are in the co-current direction and decrease in the counter-current direction from the near to the far SOL [8].

The edge toroidal rotation exhibits a dependence on both plasma density and magnetic topology, see Fig. 4-4. In LSN the rotation profile is insensitive to the plasma density, whereas in USN there is a clear density dependence. At low density in USN discharges the toroidal rotation is co-current and almost flat inside the LCFS. However, as the density is increased the flow decreases in the counter-current direction and actually changes sign. The magnitude of the change at the innermost chord ($\sim$ 3cm inside the LCFS) is around 15km/s for a change in the line averaged density of

$0.2e20m^{-3}$. A similar toroidal rotation dependence on density and topology has been observed previously in the core velocities [7]. The toroidal rotation does not continue to decrease linearly with increasing density, rather it reaches a saturation point beyond which it does not change. The smallest change in rotation is in the vicinity of the LCFS and neither the CXRS measurements nor the probes observe a variation in the SOL flow profiles as a function of density regardless of magnetic topology. The edge poloidal flows, shown in Fig. 4-5, are usually 1-2km/s in the ion diamagnetic direction, but are effectively zero within the error bars of the measurement. The profiles are generally flat and show no dependence on either magnetic topology or plasma density.

Due to the low signal level the CXRS temperature and density measurements can be quite scattered in L-mode plasmas. Generally, however, there is agreement between the ion and electron temperature profiles within the error bars of the measurement. This can be seen in Fig. 4-6A. In all of the L-mode plots shown here the position of the LCFS (vertical dashed line) has been shifted to align with the 50eV point on the temperature profile as discussed in section 4.1 and the highlighted grey area represents the uncertainty in this position. In these discharges it was not deemed necessary to shift the EFIT mapped positions of the Thomson scattering profiles as the unshifted profiles agreed with the T_B measurements within the radial uncertainty of the data.

The temperature profiles from the toroidal and poloidal periscopes tend to deviate with distance into the plasma, with the toroidal periscope reporting the higher temperature of the two. This is attributed to a low signal problem on the toroidal periscope as the poloidal periscope typically has higher signal levels and the discrepancy between the temperatures reported by the two periscopes decreases with improvement in toroidal signal levels. In Ohmic L-mode plasmas the boron density profile is fairly linear and is found to be between 0.1 and 0.3% of the electron density. The local boron density and temperature gradient scale lengths are roughly equal and are on the order of centimeters.

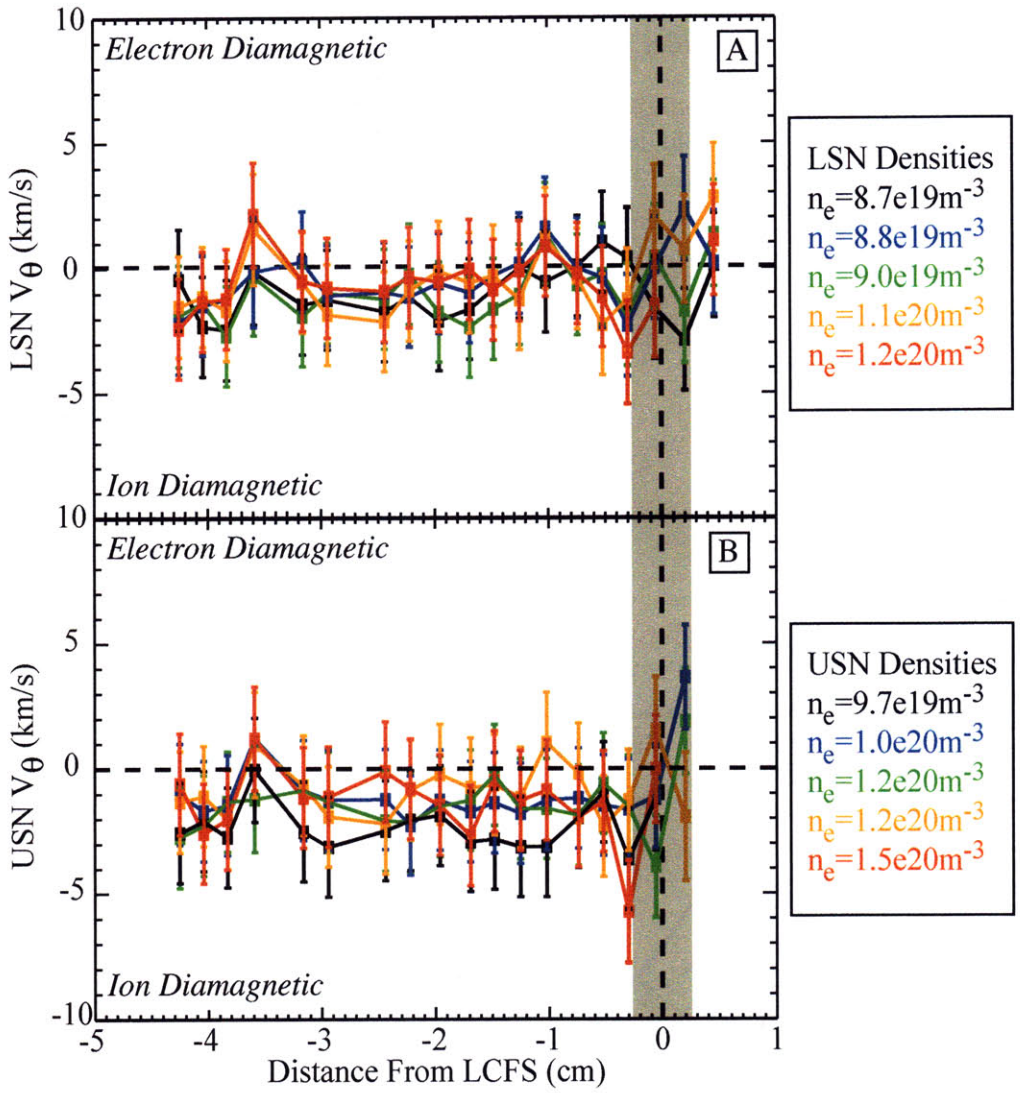

Figure 4-5: Edge B^{5+} poloidal rotation profiles and their dependence on plasma density in LSN (A) and USN (B) discharges (Run 1070627)

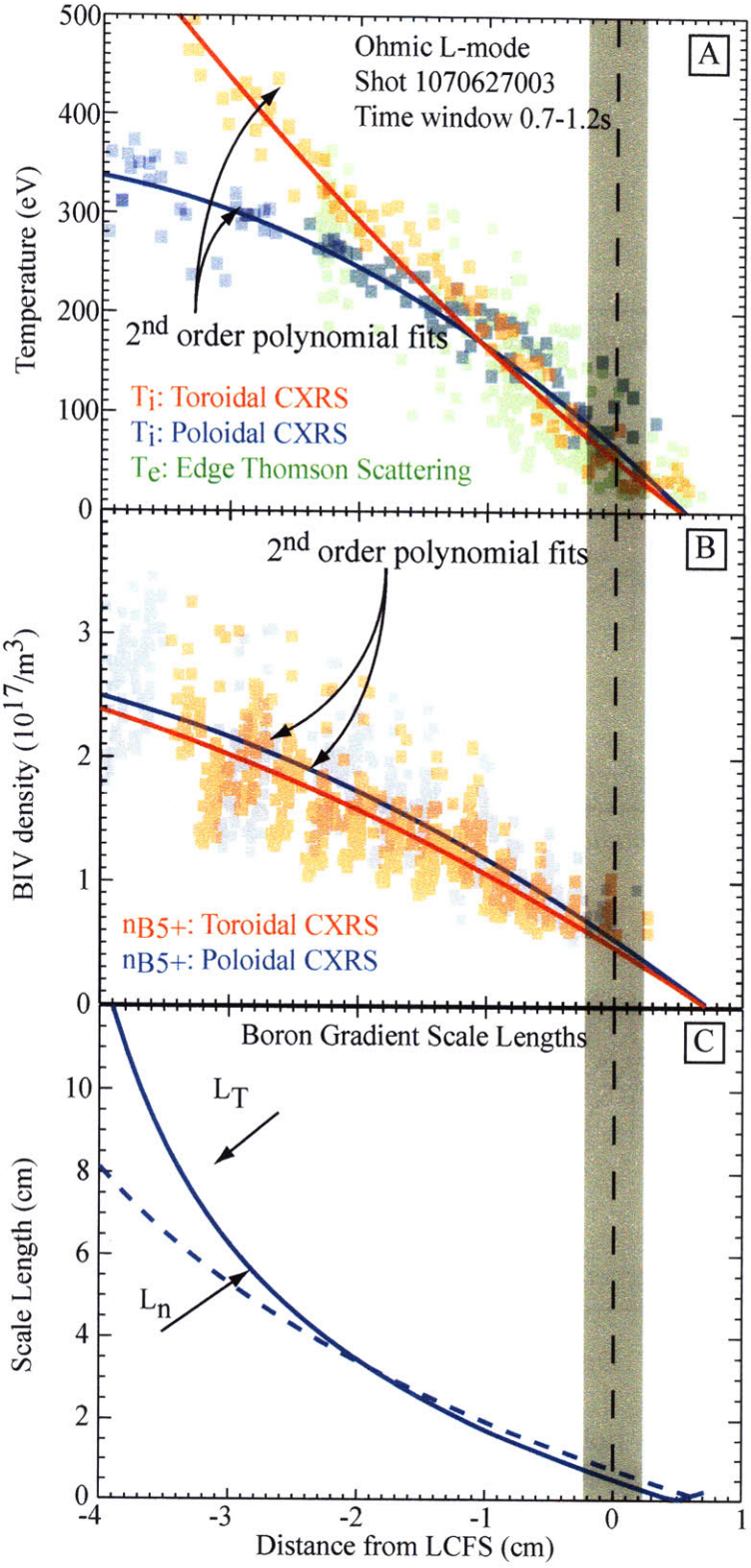

Figure 4-6: Boron temperature (A) and density (B) profiles from the poloidal (blue) and toroidal (red) periscopes averaged over a 500 ms portion of an ohmic L-mode discharge. In panel A the edge TS electron temperature profiles (black) are also plotted and agree well with the CXRS measurments. Panel C shows the boron temperature and density gradient scale lengths for this discharge.

4.3 CXRS Results in ELM-free H-mode Plasmas

ELM-free H-modes (discussed in section 1.2.2) are inherently transient H-modes characterized by continuously evolving plasma parameters. It is not surprising then that all of the edge parameters measured by the edge CXRS system also exhibit continuous evolution in these plasmas. This can be seen in Fig. 4-7, which shows the evolution of the edge flows, temperature, and density in a reversed field, LSN, ELM-free H-mode.

The poloidal velocity in the interior of the plasma remains flat and close to zero within the error bars of the measurement. However, in the pedestal region it develops a sharp peak in the electron diamagnetic direction, see Fig. 4-7 A. The well is deepest at the beginning of the H-mode and then decays as the H-mode evolves. The poloidal velocity peak and the gradient of the electron temperature profile exhibit similar rates of decay in ELM-free H-modes. This correlation is not surprising since neo-classically impurity ion flows are driven, in part, by edge temperature gradients [142, 143, 144]. The magnitudes of the poloidal velocity peaks observed in ELM-free H-modes can be very large (> 50km/s), far exceeding the toroidal rotation at the same radial location.

The temporal behavior of the toroidal velocity (Fig. 4-7 B) is similar to the poloidal velocity in that it increases co-current at the onset of the H-mode and then decays in the counter-current direction. In the pedestal region the toroidal rotation remains fairly fixed over the entire duration of the H-mode. The core toroidal rotation also increases in the co-current direction at the onset of the H-mode, however, it does not decay during the H-mode, rather the rate of rise slows and the rotation levels off at a constant value. The increase of toroidal rotation in the co-current direction from L-mode to H-mode appears to be a universal characteristic of C-Mod H-mode plasmas [7].

The boron temperature pedestal (Fig. 4-7C) reaches its peak fairly early in the H-mode and then decays as the plasma energy is radiated away by the increasing radiated power. The boron density profiles, shown in Fig. 4-7D, illustrate the cause of the increase in radiated power. In ELM-free H-modes the particle barrier is too strong leading to the monotonic increase in density (both plasma and impurity),

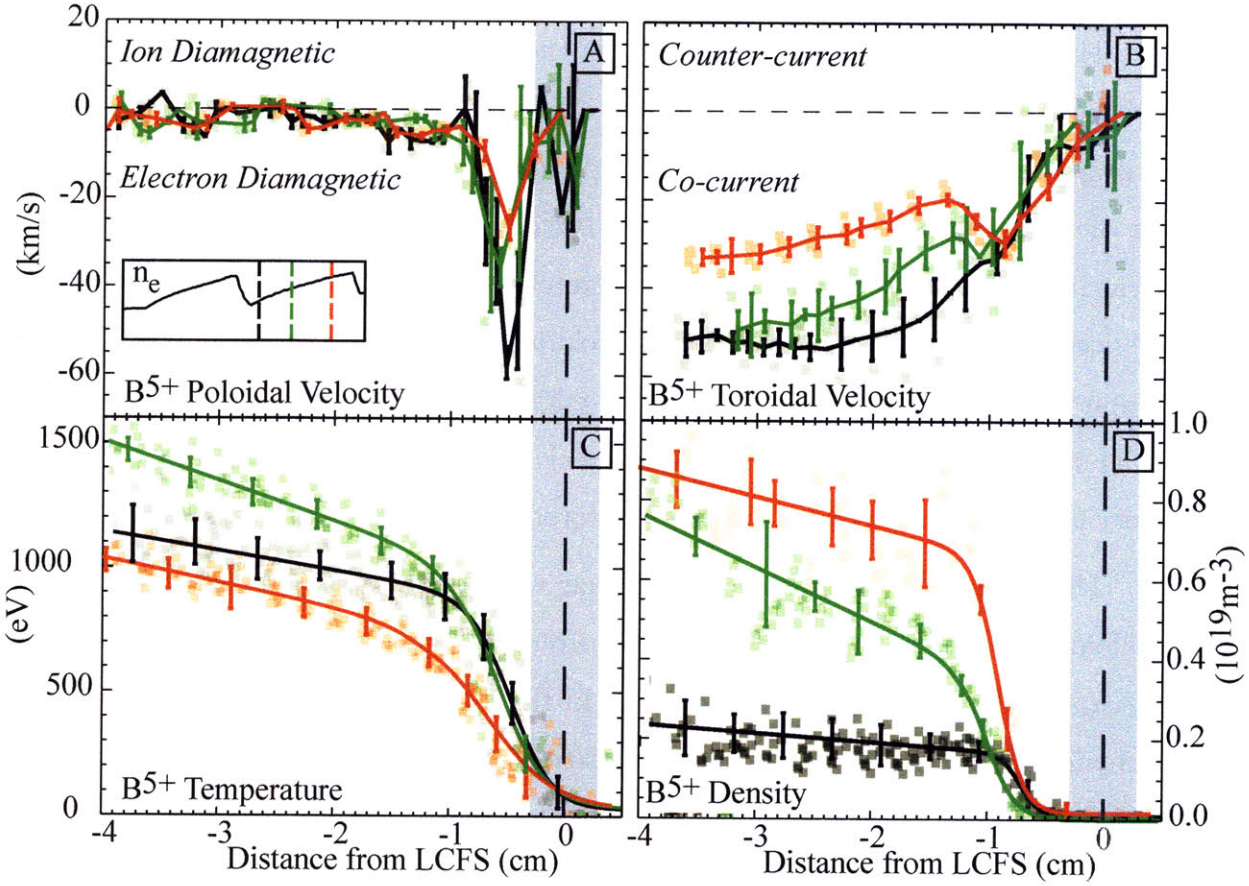

Figure 4-7: CXRS profiles in a reversed field, LSN, ELM-free H-mode (Shot=1070726014)

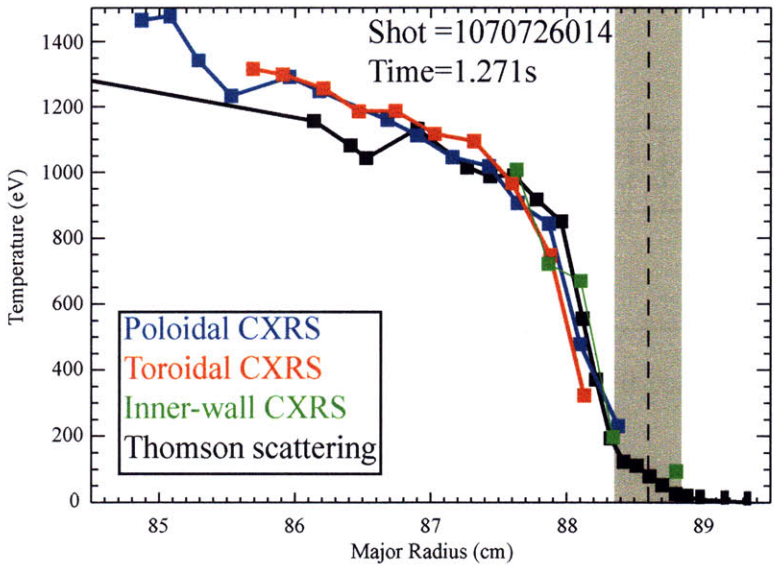

Figure 4-8: Comparison of CXRS and TS temperature profiles in an ELM-free H-mode

and thus the increase in radiated power, which is usually dominated by Mo. The boron density increases by almost a factor of 4 during the lifetime of the H-mode and increases by a factor of almost 40 from its initial L-mode value ($\sim$1.5e17m^{-3}). Compare this to the evolution of the electron density, which increases by a factor of two from L-mode to H-mode and another factor of two during the course of the ELM-free H-mode. In the ELM-free H-mode shown the boron density increases from 1.2% of the electron density to up to 3.5% by the end of the H-mode.

The boron temperature profiles agree well with the edge electron temperature profiles throughout the entire duration of the ELM-free H-mode. A comparison of the electron and ion profiles at a single time slice is shown in Fig. 4-8. In this figure the EFIT mapped positions of the TS data have been shifted by 4mm to align with the CXRS data and the position of the LCFS has been shifted to align with the 100eV point in the pedestal. This figure also illustrates how the low signal temperature discrepancy between the toroidal and poloidal periscopes disappears with improved signal level. These results indicate that the edge boron velocity distribution is isotropic since the boron temperature is measured to be the same in both the parallel and perpendicular directions.

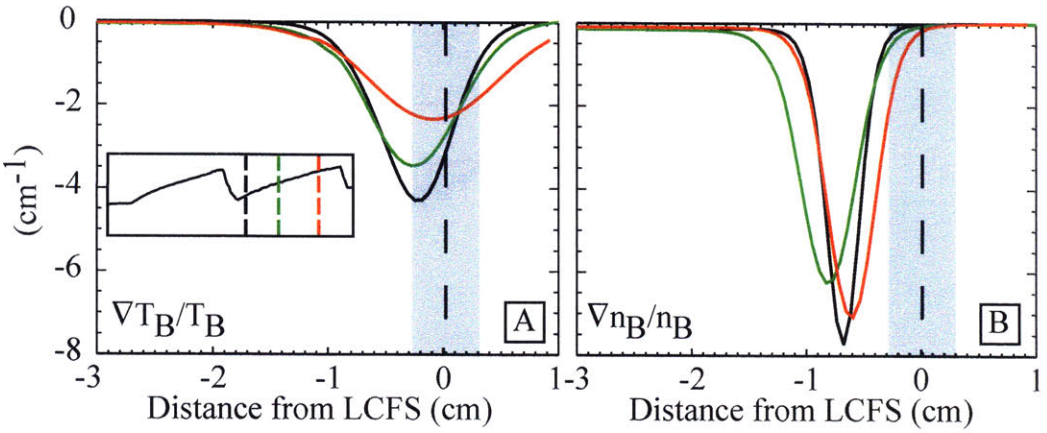

Figure 4-9: Boron temperature and density inverse scale length evolution in an ELM-free H-mode (Shot=1070726014)

The evolution of the impurity ion temperature and density gradients can also be examined during ELM-free H-modes. These gradients normalized to T_B and n_B respectively (L_T^{-1} and L_n^{-1}) are plotted in Fig. 4-9. Although the magnitude of the boron density profile exhibits much more dramatic changes during ELM-free H-modes than does the boron temperature profile, its inverse gradient scale length does not vary significantly during this evolution. The temperature inverse scale length, however, changes by a factor of two over the course of the H-mode. The impact of this behavior will be discussed further in chapter 5. The temperature and density gradient scale lengths in the pedestal region of ELM-free H-modes are both on the order of millimeters.

The ELM-free H-mode results discussed in this section have also been observed in forward field, USN discharges. However, the quality of the discharges, the level of CXRS signal, and the clarity of the results do not equal the reverse field examples. To illustrate this, the evolution of the boron poloidal velocity and density profiles from a forward field, USN, ELM-free H-mode are shown in Fig. 4-10. The magnitude of the poloidal velocity peak in forward field USN ELM-free H-modes, although still quite large (20-30km/s), are generally substantially less than the corresponding reversed field profiles.

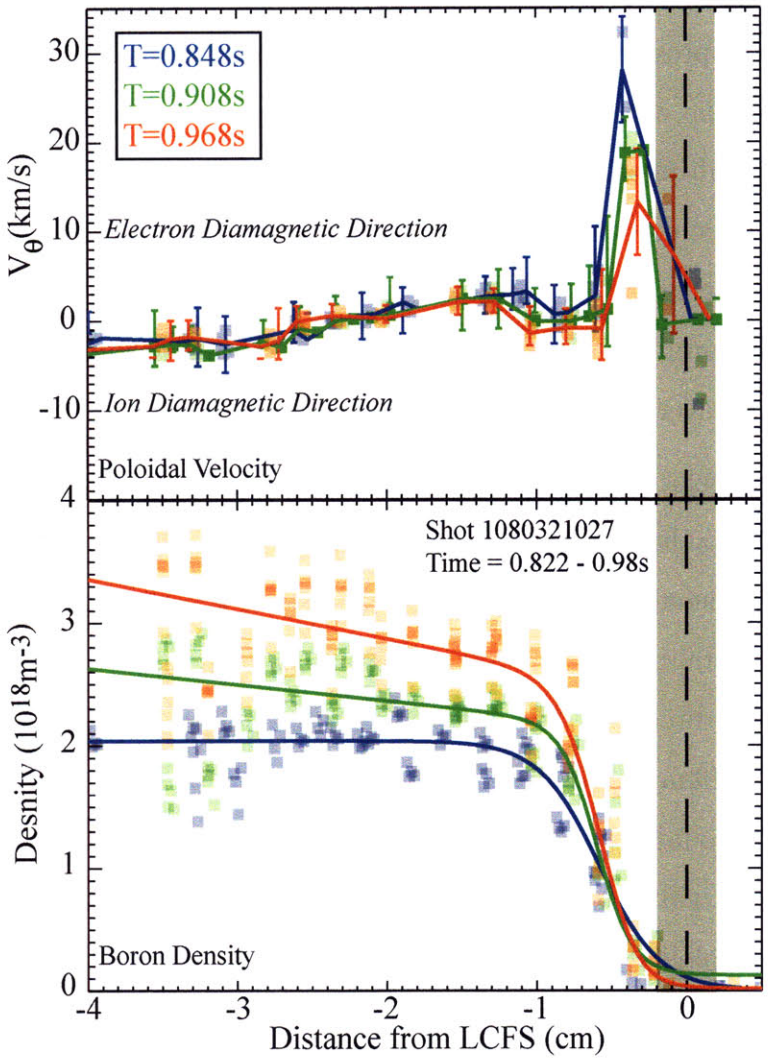

Figure 4-10: Boron poloidal velocity and density evolution in a forward field, USN, ELM-free H-mode. (Shot=1080321027)

4.4 CXRS Results in EDA H-mode Plasmas

EDA H-modes, discussed in section 1.2.1, are steady state H-modes characterized by an edge instability known as the QCM, which acts to increase particle transport through the pedestal, regulating the plasma density and impurity accumulation. In steady EDA H-modes the edge parameters measured by the CXRS system are also observed to be approximately constant in time. This behavior enables detailed, low noise profiles of the edge boron flows, temperature, and density to be obtained by averaging over multiple time frames. Additionally, the constancy of the plasma temperature, density, and position across DNB pulses in EDA H-modes makes CXRS data from this type discharge more abundant and more reliable than data from ELM-free H-modes. CXRS profiles from an EDA H-mode are shown in Fig. 4-11. These profiles were obtained by averaging over a 100ms period.

The poloidal velocity profiles observed in EDA H-modes (Fig. 4-11 A) are qualitatively similar to those observed in ELM-free H-modes. Inside the pedestal region the profile is flat, small in magnitude, and slightly in the ion diamagnetic drift direction. In the pedestal region, however, it develops a high, narrow peak in the electron diamagnetic drift direction. The magnitude of the poloidal velocity peak is typically between 10 and 20km/s and the width is measured to be between 3 and 4 mm wide (FWHM). One should note that the radial resolution of the diagnostic is of the same order. If the peak width were narrower it would be below the ability of the diagnostic to discern. The poloidal velocity peak roughly coincides with the top of the temperature pedestal (Fig. 4-11C) and the mid-point of the boron density pedestal (Fig. 4-11D). As a result of this alignment it is fairly easy to measure the inner half of the velocity peak, while the outer half is often lost due to insufficient signal. For this reason the ability in EDA H-modes to obtain detailed profiles by combining multiple time frames is highly advantageous to studying the structure of the edge poloidal velocity peak.

The toroidal velocity, shown in Fig. 4-11 B, increases in the co-current direction across the entire radial profile (inside the LCFS) at the onset of EDA-H-modes. Inside

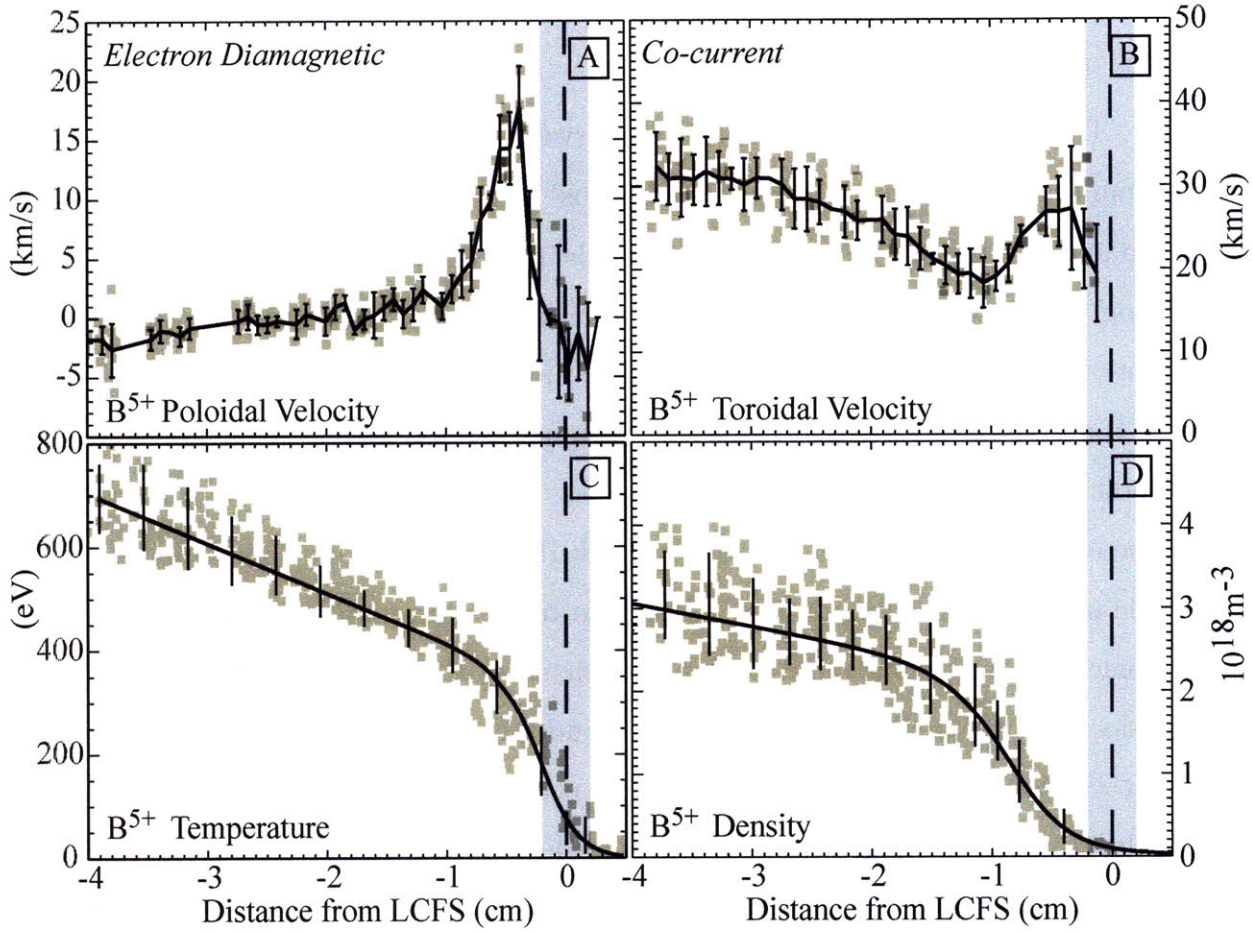

Figure 4-11: CXRS data in an EDA H-mode plasma averaged over a 100ms time window (shot=1070621003).

the top of the temperature pedestal the toroidal velocity profile becomes increasingly co-current with distance into the plasmas. In the pedestal region itself the rotation is observed to remain flat or to exhibit a local minimum around the pedestal top and to increase slightly in the co-current direction as it nears the LCFS. This leads to a small region of inverse toroidal velocity shear very similar to what has been observed on ASDEX Upgrade [145]. The ASDEX team correlates this flow behavior with the presence of steep edge gradients and speculates that PS flows may be able to explain the observations.

The core toroidal rotation is also observed to increase in the co-current direction from L-mode to H-mode. This 'spontaneous' H-mode rotation is believed to be 'spun-up', at least in part, by an edge source as the rotation is observed to propagate inward from the edge [6]. This can be seen by examining the time traces of the edge and core toroidal rotation during an L-H transition, see Fig. 4-12. Here, the time of the L-H and H-L transitions as determined through examination of the D_α time trace are indicated by the blue, dashed, vertical lines. The green line shows the time at which the edge toroidal rotation reached its peak H-mode value, and the red line indicates the same for the core rotation. The edge temperature and density pedestals both come to steady state values within $\sim$ 20ms after the transition. The edge toroidal velocity at the pedestal top (R=88.3cm) and the peak in the poloidal velocity profile (R=88.6cm) both continue to rise after the pedestals are fully formed taking of order $\sim$ 50ms to reach their steady-state H-mode values, while the core toroidal velocity does not reach a steady state until almost 130ms after the L-H transition (red dashed line). The edge velocities plotted in Fig. 4-12 are passive (line integrated) measurements of B^{4+} not localized CX measurements of B^{5+}. These traces are used because they are less noisy than the active traces and because they are not dependent upon DNB pulses and so can track the plasma evolution on a continuous 5ms time base through the L-H transition.

In the edge toroidal and poloidal velocity time traces from Fig. 4-12 there appears to be pre-cursor to the L-H transition, however, those data points are unreliable for several reasons. First, the exact time of the L-H transition as determined by the

D_α, can be delayed somewhat from the true L-H transition time. Second, these time points coincide with the injection of ICRF power and the beginning of a DNB pulse both of which alter the measured spectra. And lastly, according to EFIT, the plasma moved of order 3-4mm over this time period, which is a significant radial sweep with respect to the diagnostic views

The change in the core toroidal rotation from L-mode to H-mode, as measured by the soft x-ray diagnostics, is observed to scale linearly with the change in stored energy normalized to the plasma current and the change in the edge pressure pedestal height [7]. This scaling, shown in Fig. 4-13, was determined using a database containing over 1000 discharges representing forward and reverse field H-modes (EDA and ELM-free), a wide range of plasma parameters, and a variety of magnetic topologies. The black dots are core toroidal rotation from individual discharges and the larger red dots are the binned averages. The blue dots are edge toroidal rotation data (inside the top of the pedestal) from steady state portions of EDA H-modes. The inclusion of edge data points from ELM-free H-modes adds scatter to the data, but does not significantly alter the result.

Since rotation is observed to propagate from the edge inward, it is reasonable to expect that the change in toroidal rotation at the edge (inside the pedestal top) would exhibit similar behavior to the core. However, as can be seen in Fig. 4-13, the change in the edge rotation is nearly constant as a function of the change in plasma stored energy. A similar result is obtained when this is examined as a function of T_e, n_e, P_e and their gradients. The small amount of variation in the edge B^{5+} toroidal rotation shows that the velocity change at the edge of the plasma remains roughly constant regardless of the edge pedestal height or the observed change in the core rotation. In a purely diffusive system the rotation change at the top of the pedestal would equal the final change in the core leading to a flat velocity profile. This is clearly not the case on C-Mod. Therefore, an additional mechanism inside the top of the pedestal is needed to explain the remainder of the core velocity change. The residual stress [146] is one potential mechanism that could explain this behavior.

The height of the poloidal velocity peak, defined as the difference between the

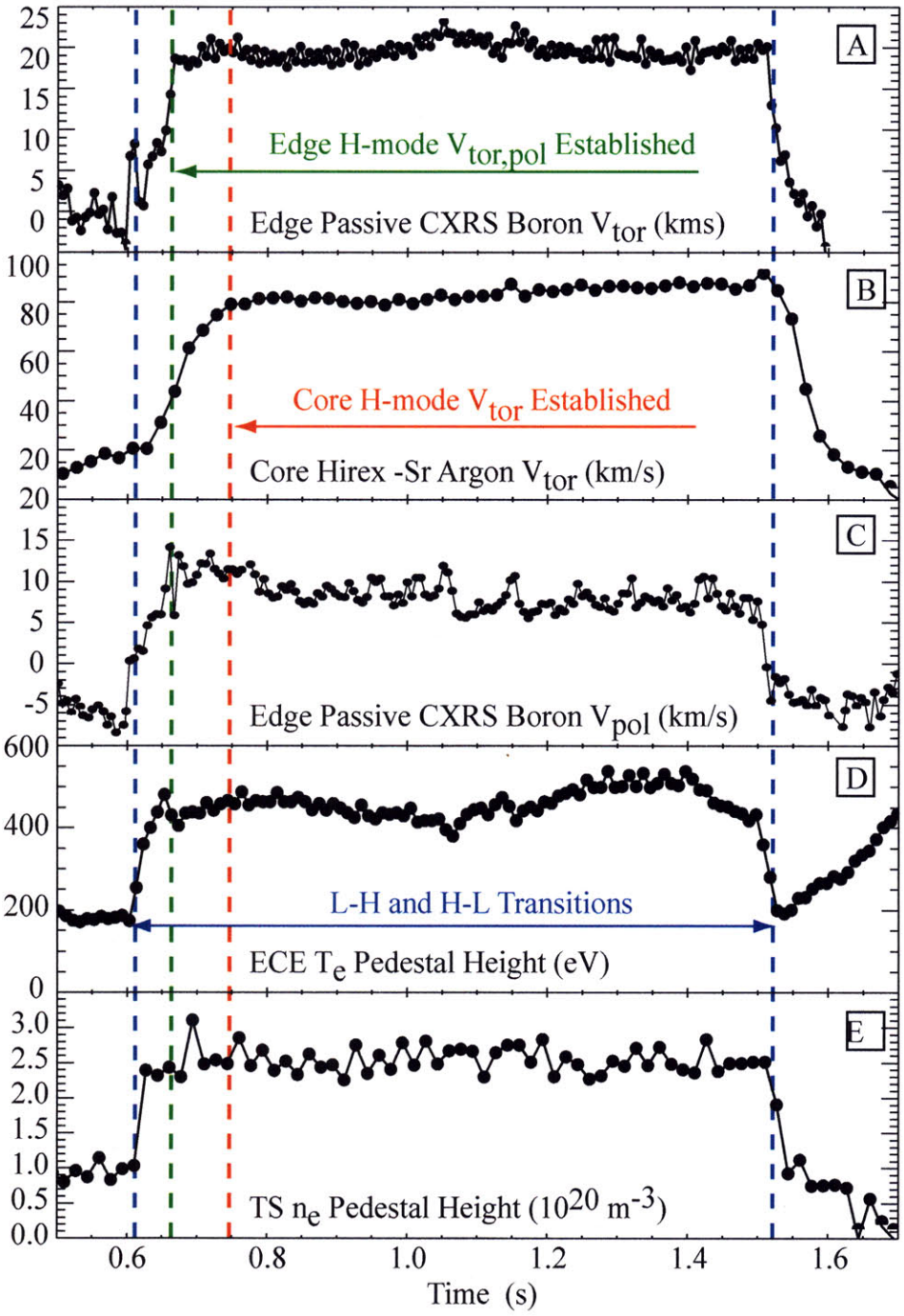

Figure 4-12: Evolution of the plasma spin-up during an L-H transition. A) Line integrated boron toroidal velocity at the top of the pedestal (R=88.5cm). B) Line integrated argon toroidal velocity in the core of the plasma. C) Line integrated boron poloidal velocity at the top of the pedestal D) Edge temperature pedestal evolution from the ECE diagnostic E) Edge density evolution from the edge TS system

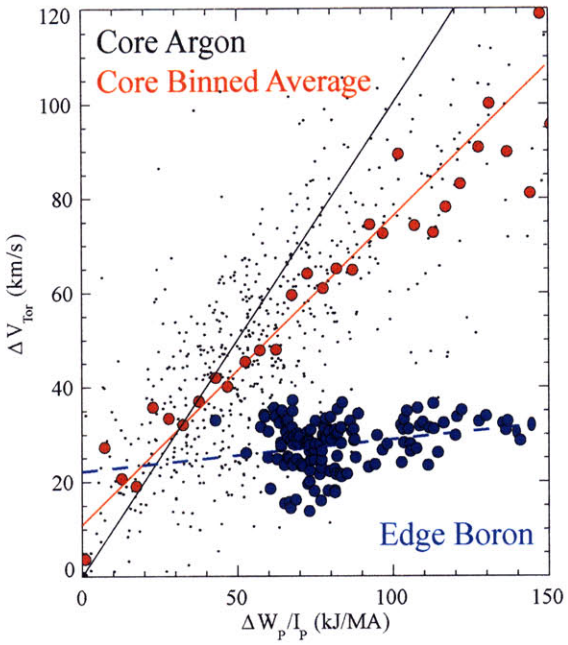

Figure 4-13: Change in toroidal rotation velocity between L-mode and H-mode as a function of the change in plasma stored energy normalize to plasma current

maximum H-mode peak velocity and the corresponding L-mode value, can also be examined as a function of plasma parameters. In EDA H-modes the magnitude of this peak shows little to no dependence on any of the edge pedestal parameters or their gradients. However, if data points from ELM-free H-modes are included then the velocity peak appears to scale with the edge temperature pedestal height (and gradient), see Fig. 4-14. The scatter in this data set is primarily the result of incomplete poloidal velocity peaks that result from the low signal levels. Also, the true maximum of the poloidal velocity peak can be improperly determined given that the width of the peak is of order the view size.

The boron density is typically 1-1.5% of the electron density and the n_B pedestal location is typically inside of the n_e pedestal by roughly 1cm. The boron temperature profiles are very similar in both shape and magnitude to the electron temperature profiles measured by the edge TS system. A comparison of these two profiles is shown in Fig. 4-15.

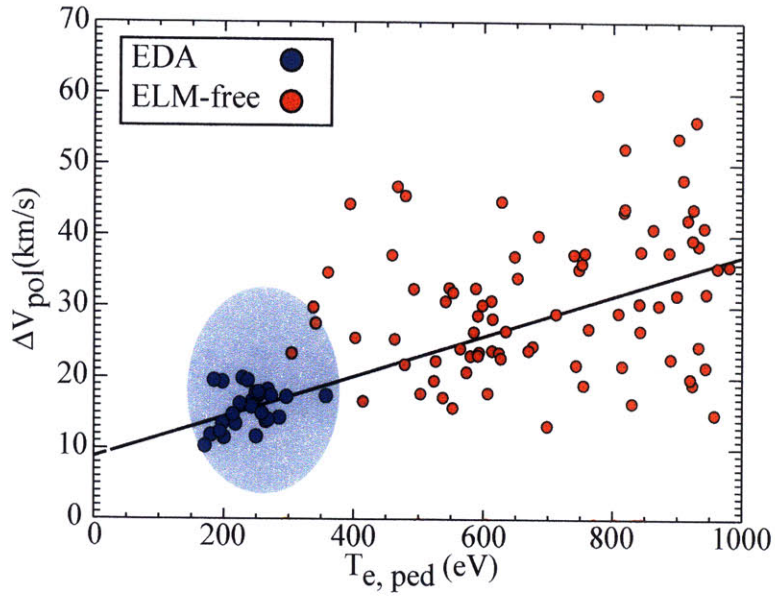

Figure 4-14: Maximum change in the edge poloidal velocity profile from L-mode to H-mode as a function of electron temperature pedestal height. Red data points are individual time frames of ELM-free H-modes. The blue data points are averages over the steady state portions of EDA H-modes and the shaded blue region illustrates the scatter in the EDA data

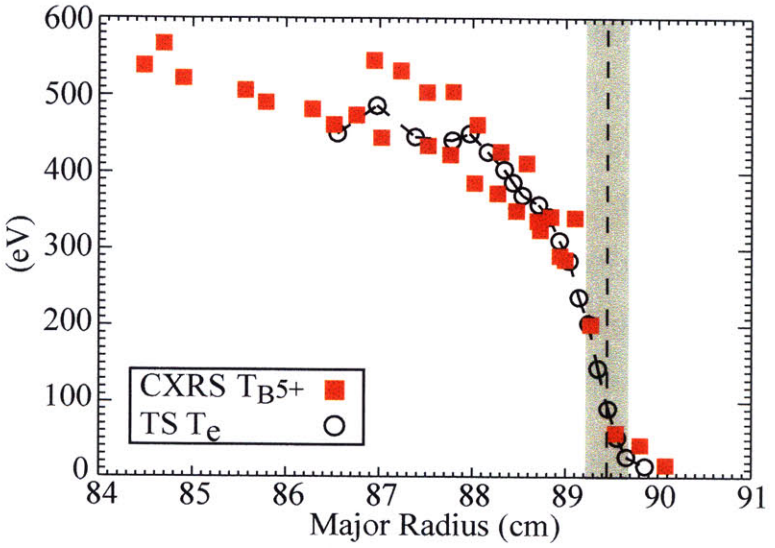

Figure 4-15: Comparison of the electron and boron temperature profiles in EDA H-mode plasmas (Shot=1080321020)

4.5 CXRS Results in I-mode Plasmas

The I-mode, discussed in section 1.2.3, is a newly developed operating regime on C-Mod that combines enhanced energy confinement with moderate particle confinement resulting in a low collisionality pedestal without ELMs. All I-mode plasmas are USN discharges with input power just below the threshold power for an L-H transition. The low particle confinement presents a problem for making CXRS measurements as the boron levels in the plasmas (and the active CXRS signal) are not enhanced significantly above their L-mode values. For this reason most of the active CXRS profiles presented in this section were obtained by averaging over multiple time frames. Active CXRS profiles averaged over a 250ms steady state portion of an I-mode discharge are shown in Fig. 4-16. For this discharge the signal on the toroidal periscope was too low to fit individual time frames. Instead, all of the frames in a given DNB pulse were summed to together to form one frame. This is why there are fewer data points in the toroidal velocity plot (Fig. 4-16B) than in the other profiles.

In I-mode plasmas the poloidal velocity forms a small peak in the electron diamagnetic direction at the edge of the plasma within a centimeter inside of the LCFS, see Fig. 4-16A. This peak is similar to those observed in H-mode plasmas, however the magnitude is typically smaller of order ~5km/s. On any given time frame the velocity peak is observed over 2-3 radial channels giving a FWHM of order 4-6mm. However, when averaging over multiple time slices the peak locations do not always align, giving the appearance of a broader structure (8-10mm). However, this broad peak could potentially be the result of error in the plasma position when averaging over long periods of time. The edge toroidal velocity increases in the co-current direction after the application of ICRF power and in the I-mode it remains co-current between 10 and 20km/s as shown in Fig. 4-16B.

In I-mode plasmas the edge temperature forms a clear pedestal very similar to those observed in H-mode plasmas, see Fig. 4-16C. In fact, the energy confinement in I-mode plasmas can equal that attained in similar EDA H-modes. This temperature pedestal is observed in both the ion and electron populations and is maintained steady

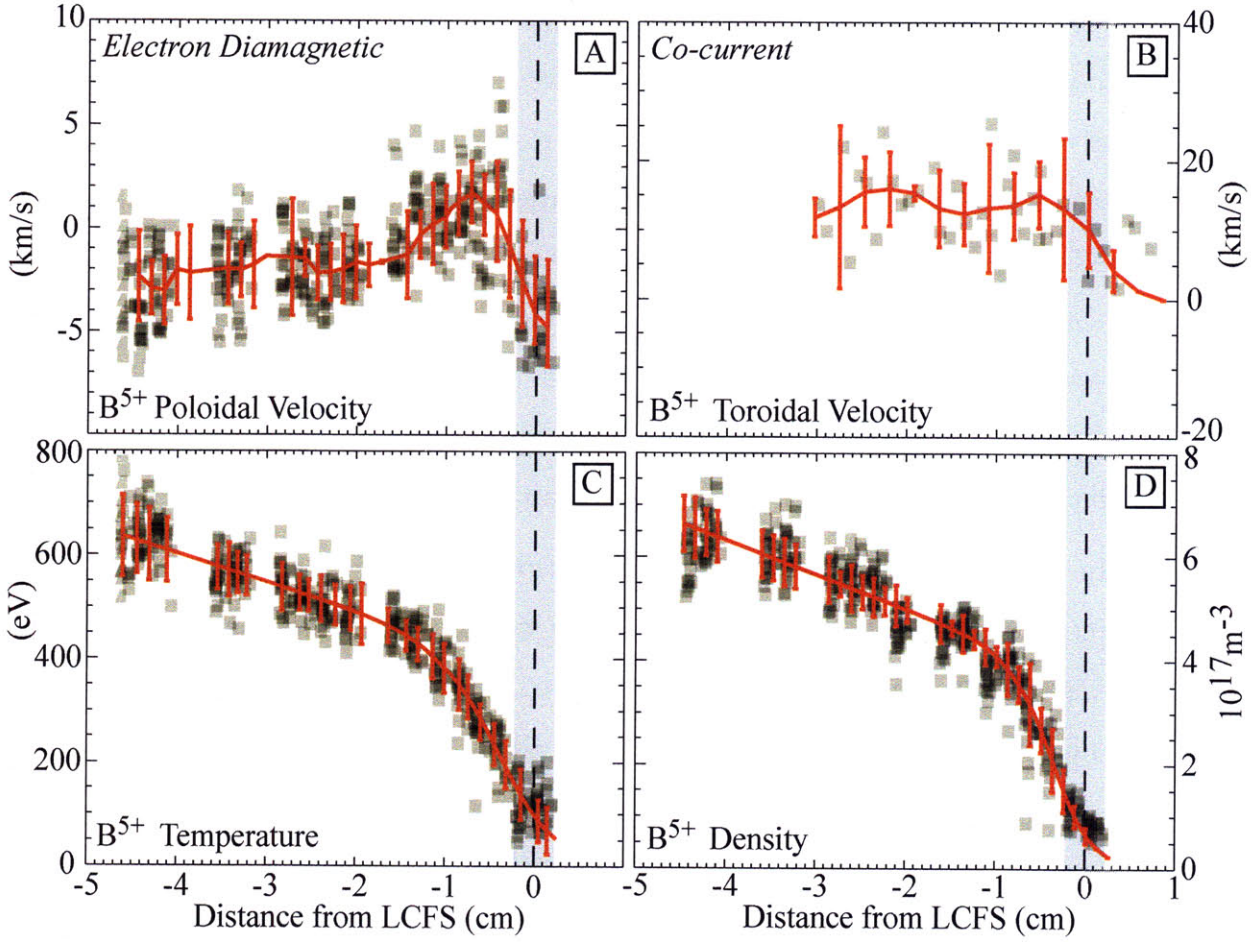

Figure 4-16: CXRS results in I-mode plasmas averaged over a 250ms time window (shot=1080415017)

state in I-mode plasmas. The edge boron density (Fig. 4-16D) increases modestly above its L-mode values (factor of ~2) after the application of ICRF power and remains fairly constant during the I-mode. This is very different than its behavior in H-modes plasmas. In H-mode the impurity particle confinement is greatly improved relative to its L-mode values and results in an order of magnitude increase in the impurity density. The shape and location of the boron density profile is also different in I-mode plasmas. The boron density forms a clear pedestal, as it does in H-mode plasmas, but the pedestal is located further out (radially) relative to the T_B profile. The differences in the density profile reflect both changes in the plasma transport as well as changes in the boron ionization profile that result from the presence of the temperature pedestal.

The I-mode develops smoothly from L-mode plasmas after the application of ICRF power; there is no apparent bifurcation in either the D_α time trace or the plasma density. Fig. 4-17 shows the temporal evolution of the edge plasma parameters as well as the core velocity and magnetic fluctuations during an L-I and I-H transition. Here the edge and core toroidal velocities (panels A and B) increase in the co-current direction after the application of the ICRF power and come to steady state values during the I-mode portion of the discharge (pink highlighted region). The edge rotation (poloidal and toroidal) is observed to increase before the core and reach its equilibrium value within ~50ms after the ICRF is turned on. The core rotation spins up more slowly, taking closer to ~100ms to reach its final value. The edge temperature profile also increases after the ICRF power, rising steadily during the L-mode portion of the discharge (100-150ms) and coming to a steady value of 400eV in the I-mode. This is to be compared this to the 20ms time scale for H-mode pedestal formation. At I-H transitions the height of the temperature pedestal is usually observed to increase further by roughly 10-20% and does so on a typical H-mode timescale. This is true of both the electrons and the boron temperature profiles. For the discharge shown in Fig. 4-17 the input power was kept constant in time. The details of the timescales and evolution of the edge parameters can depend on the amount of input power and whether or not the power is varied.

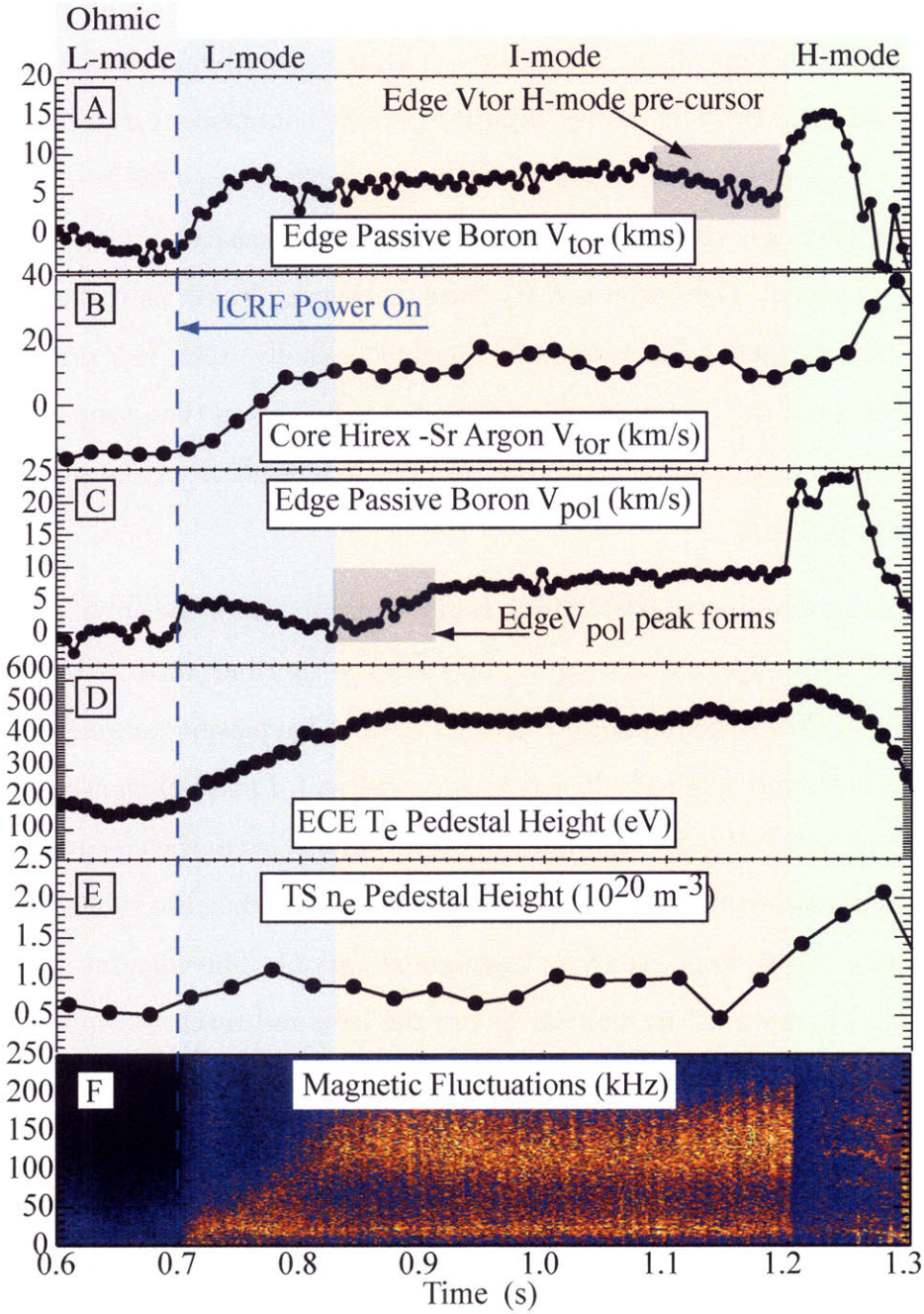

Figure 4-17: Plasma evolution during an L-I and I-H transition A. Line integrated boron toroidal velocity at the top of the pedestal (R=88.5cm). B. Line integrated argon toroidal velocity in the core of the plasma. C. Line integrated boron poloidal velocity at the top of the pedestal D. Edge temperature from the ECE diagnostic E) Edge density from the edge TS system F. Magnetic fluctuations BP3T-ABK (Shot=1080416021)

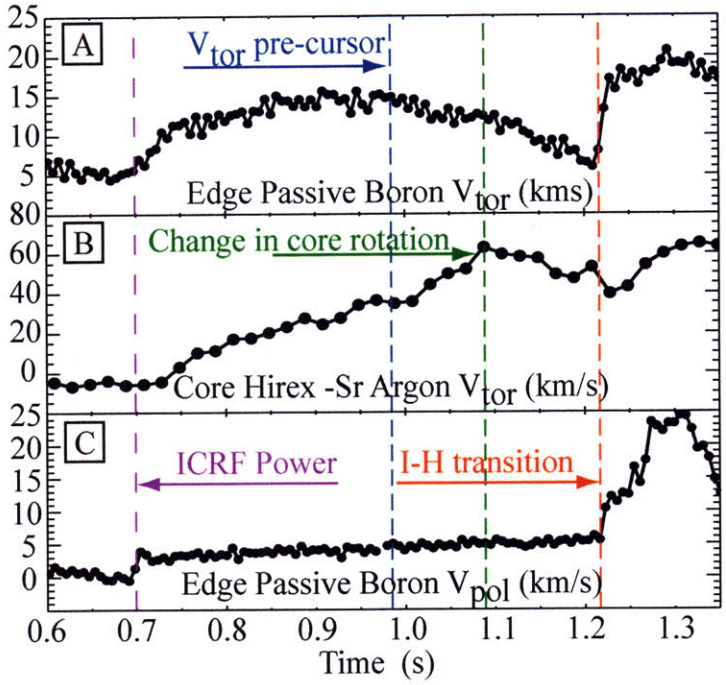

Figure 4-18: Toroidal velocity evolution in I-mode prior to H-mode transition (Shot=1080416018)

In I-mode discharges the toroidal rotation is observed to decrease in the counter-current direction prior to I-H transitions. This behavior has been observed in both the edge and the core toroidal rotation and is shown in Fig. 4-18. After the transition to H-mode the edge and core toroidal rotation are seen to increase again in the co-current direction and assume values that are consistent with the trends and scalings discussed in section 4.4. Radial profiles of the edge B^{5+} toroidal velocity evolution between L-mode, I-mode and H-mode are shown in Fig. 4-19. In the L-mode portion of this discharge the toroidal rotation profiles are co-current and nearly flat, consistent with the USN L-mode velocity results presented in section 4.2. The rotation increases co-current as the plasma heats up (green traces). But approximately 50ms before the I-H transition the edge rotation changes in the counter-current direction. The effect is strongest within 1 cm of the LCFS. The velocity at the LCFS remains pinned throughout all of this evolution. After the I-H transition, the toroidal rotation returns co-current to typical H-mode values. There are also changes to the poloidal rotation profile in the pedestal region during this time. However, the changes are much smaller

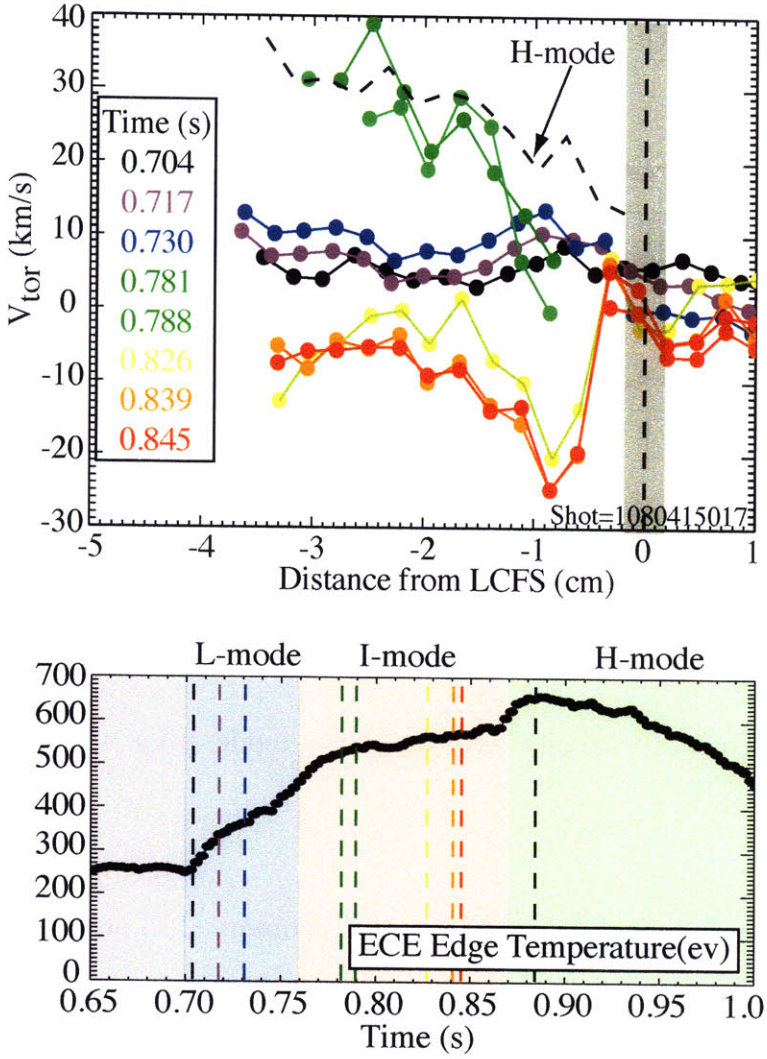

Figure 4-19: Radial profiles of a toroidal velocity evolution in I-mode prior to H-mode transition and corresponding time trace of the edge electron temperature from the ECE diagnostic

(a few km/s) than what is observed in the toroidal velocity and as a result, difficult to pull out of the noise.

Chapter 5

Edge Radial Electric Field Structure on Alcator C-Mod

In this chapter the first edge radial electric field profiles from the Alcator C-Mod tokamak will be presented. The structure and behavior of E_r will be explored in a variety of plasma regimes including L-mode, EDA H-mode, ELM-free H-mode and I-mode plasmas. All of the E_r profiles in this thesis, unless otherwise specified, were determined using data from the new edge CXRS diagnostic. As such, they represent the plasma behavior at the mid-plane on the LFS of the tokamak. When possible the CXRS determined E_r profiles will be compared to E_r measurements from other diagnostics. The C-Mod radial electric field profiles are qualitatively consistent with measurements made on other devices (see section 2.6). However, the E_r profiles on C-Mod are unique in that they form in plasmas that are free from any externally applied torque. Thus, they represent the 'natural' radial electric field inherent to the physics of a given plasma regime.

5.1 Calculation of the Radial Electric Field

The standard method for obtaining radial electric field profiles in fusion plasmas is to calculate them through the momentum or force balance equation [147],

$$m_i n_i \left(\frac{\partial \mathbf{V}_i}{\partial t} + \mathbf{V}_i \cdot \nabla \mathbf{V}_i \right) = -\nabla p_i - \nabla \Pi + e Z_i n_i \left(\mathbf{E} + \mathbf{V}_i \times \mathbf{B} \right). \tag{5.1}$$

Here the subscript i denotes species, m, n, and Z are the mass, density, and atomic number, $\mathbf{V}$ is the flow velocity, $\mathbf{E}$ and $\mathbf{B}$ are the electric and magnetic fields, p represents the diagonal terms in the pressure tensor and Π the off diagonal terms. In steady state and under the assumption that the radial velocity is negligible compared to the toroidal and poloidal velocities the radial component of Eq. 5.1 is

$$E_r = \frac{1}{n_i Z_i e} \frac{dP_i}{dr} + (\nabla \Pi)_r - V_{\theta,i} B_\phi + V_{\phi,i} B_\theta. \tag{5.2}$$

Additionally, if the viscous forces in the radial direction are assumed to be much smaller than the pressure gradient then the off diagonal contributions from the pressure tensor are negligible and one obtains the form for the radial electric field given in Eq. 1.1

$$E_r = \frac{1}{n_i Z_i e} \frac{\partial p_i}{\partial r} - V_{\theta,i} B_\phi + V_{\phi,i} B_\theta. \tag{5.3}$$

The three terms left that contribute to E_r are the diamagnetic ($\frac{1}{n_i Z_i e} \frac{dP_i}{dr}$), poloidal velocity ($V_{\theta,i} B_\phi$), and toroidal velocity ($V_{\phi,i} B_\theta$) contributions. To calculate E_r accurately, one needs to know the toroidal and poloidal magnetic fields as well as the temperature, density, and toroidal and poloidal velocity for a single species in the plasma. The toroidal magnetic field is known, the poloidal magnetic field is determined by the EFIT[12] reconstruction of the plasma and the new CXRS diagnostic on C-Mod provides simultaneous measurements of all the necessary profiles for the B^{5+} population in the edge pedestal region. In addition, experimental measurements of the edge boron distribution function indicate that it is Maxwellian, justifying the simplification of the pressure tensor to the gradient of the pressure for this species.

5.2 E_r in Ohmic L-mode Plasmas

In L-mode plasmas the edge radial electric field inside the LCFS is generally positive (radially outward), small in magnitude and exhibits very little shear outside of the noise in the measurement. Example L-mode E_r profiles from both USN and LSN discharges are shown in Fig. 5-1. The boron velocity components dominate the calculation of E_r. The poloidal velocity, although much smaller than the toroidal velocity, results in a sizable contribution due to C-Mod's large toroidal magnetic field. In a standard discharge B_ϕ at the low field side of the plasma is of order 4.2T (5.4T at the magnetic axis) while B_θ is only 0.7T (I_p=800kA). This means a 2km/s poloidal velocity gives an equivalent contribution to E_r as does a 12 km/s toroidal velocity. Additionally, small amounts of noise in the poloidal velocity result in large error bars on the total E_r profile. In L-mode plasmas both the toroidal and poloidal velocity components give positive contributions to the radial electric field at the edge of the plasma. The diamagnetic contribution is negative and acts to reduce the magnitude of the field by a few kV/m.

There is little structure to the E_r profile outside of the error bars. There is a slight trend towards more negative fields further into the plasma as a result of the toroidal velocity contribution, see section 4.2. However, this effect tends to get washed out by the noise from the poloidal velocity contribution. LSN and USN E_r profiles inside the LCFS are typically very similar with no major distinguishing features, except that in USN plasmas E_r exhibits a dependence on plasma density that is also observed through the toroidal velocity contribution. This dependence can be seen in the USN E_r profiles shown in Fig. 5-1B. Near the LCFS E_r decreases, approaches zero and in some cases changing sign. All three of the terms in Eq. 5.3 contribute to this. The toroidal velocity decreases in the counter-current direction in this region, the poloidal velocity begins to increase in the electron diamagnetic direction, and the pressure gradient term has a local minimum in this region.

The E_r profiles determined from CXRS data are consistent with the E_r measurements made in the plasma core. There, E_r is dominated by the toroidal rotation,

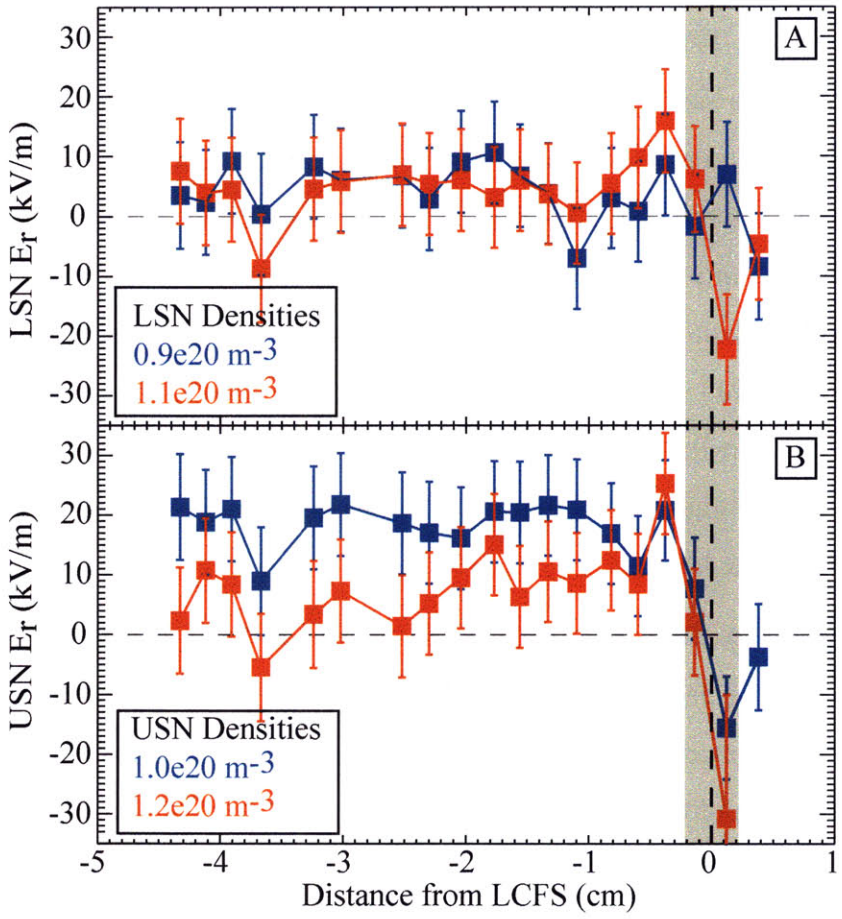

Figure 5-1: Radial electric field profiles in LSN and USN Ohmic L-mode discharges (Shots 1070627002, 008, 011, 018). The LCFS here corresponds to the 50eV point on the temperature profile.

which is typically in the counter-current direction in L-mode plasmas resulting in negative E_r profiles. Whether or not the CXRS based E_r profiles are consistent with the measurements made by the scanning probes is not clear. The scanning probes measure the plasma potential directly and then compute E_r as the negative gradient of the potential profile ($E_r = -\partial\Phi/\partial r$). According the LFS probe measurements the radial electric field near the LCFS is dependent upon topology and plasma density[8]. For low densities ($\bar{n}_e = 1 \times 10^{20} m^{-3}$) the LFS probe measurements indicate that E_r changes sign at the LCFS for both USN and LSN, being negative inside and positive outside [8]. At higher densities ($\bar{n}_e = 1.5 \times 10^{20} m^{-3}$) the LSN result does not change, but in USN the peak in the potential moves deeper into the SOL, indicating that the electric field at the LCFS (and into the SOL) should be negative. The CXRS based E_r profiles in Fig. 5-1 approach zero and sometimes become negative in the SOL. This could potentially be consistent with the probe measurements if the position of the LCFS were shifted radially outward by a few millimeters. In that case, E_r would be positive in the SOL, have a negative local minimum (E_r well) just inside the LCFS or just outside (USN high densities) and then become positive again in the plasma. More detailed analysis and comparison between the LFS scanning probe and CXRS profiles is required to determine the consistency of the data sets.

5.3 E_r in H-mode Plasmas

The structure of the edge radial electric field in C-Mod H-mode plasmas is qualitatively similar to the structure observed on other tokamaks (section 2.6). In the plasma core E_r is dominated by the toroidal rotation. This means that on devices that utilize neutral heating beams the direction of the core electric field is controlled by the direction of momentum input. On C-Mod, however, the intrinsic, H-mode, co-current, toroidal rotation means that the core electric field is always positive. The possible exception to this is if the internal temperature and/or density profiles are sufficiently peaked (internal transport barriers) then the contributions from the diamagnetic and poloidal velocity terms can become comparable in magnitude to the toroidal velocity

component, but negative. This is the situation that is always present at the edge of H-mode plasmas. In this region all three terms are of the same order and must be measured to accurately determine the total E_r profile. On most devices, including C-Mod, the poloidal velocity and the diamagnetic contributions at the edge are negative and create a negative E_r well just inside of the LCFS. In C-Mod the E_r well is observed to exist within 1cm inside of the LCFS and is both considerably narrower (~5mm) and deeper (< 300kV/m) than has been observed on other devices. This will be shown in the sections that follow.

5.3.1 E_r in ELM-free H-modes

ELM-free H-modes provide interesting cases for studying radial electric field behavior because of their inherently transient nature and continuously evolving plasma parameters. In these H-modes the E_r well is also observed to evolve as shown in Fig. 5-2A. The depth of the well behaves similarly to the plasma temperature and energy confinement in that it peaks early in the H-mode and then decreases as the H-mode evolves. For the ELM-free H-mode shown, the E_r well is initially over 300kV/m deep and reduces by more than 50% by the end of the H-mode. The E_r well center is always located within 1cm inside of the LCFS and typically aligns radially with the middle to top portion of the temperature pedestal. For the profiles shown, the FWHM of the well remains constant at roughly 4mm ±1mm, despite the dramatic changes in the edge pedestal profile (factor of 2 in n_e). This result seems to contradict any theories that suggest that the E_r well width should scale inversely with the plasma density (see sections 2.3.2 and 2.4). According to the BDT model, discussed in section 2.2, the quantity of interest with respect to plasma confinement is the **ExB** shear, ω_s. This quantity is shown in Fig. 5-2B and tracks with the depth of the radial electric field well. In the beginning of the H-mode the shearing rate is very large, of order -1.8x10^7Hz, but decays to 2-3 x10^6Hz by the end of the ELM-free H-mode.

All of the individual components used to determine the radial electric field also exhibit evolution during ELM-free H-modes. These components are shown in Fig. 5-3. The E_r well itself is composed of contributions from both the poloidal velocity

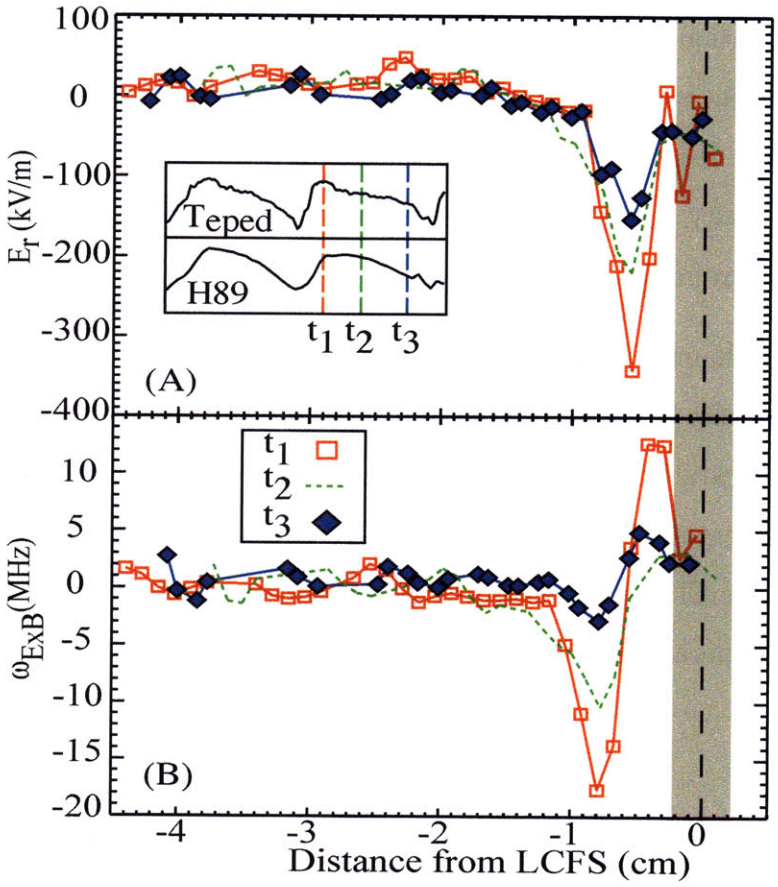

Figure 5-2: Evolution of the edge radial electric field profile and **ExB** shear rate in an ELM-free H-mode (Shot=1070726014)

and the diamagnetic components, which each form well-like structures in the pedestal region. The location of these wells overlap radially leading to an additive well depth and a total E_r well width that is wider than the individual components. The poloidal velocity is typically the larger of the two contributions. The toroidal velocity is the only positive contribution to E_r and in the pedestal region gives a fixed linear offset to the profile. The decay of the E_r well depth (and **ExB** shear rate) through the ELM-free H-mode is observed through the evolution of both the diamagnetic and poloidal velocity contributions, which decrease by 30 and 50%, respectively. The toroidal velocity component in the pedestal region remains fairly fixed over the entire duration of the ELM-free H-mode and thus does not contribute to the change. However, the toroidal velocity inside the pedestal region decreases as the plasma confinement degrades as shown in Fig. 5-3(c).

The largest change in the E_r well depth (~100kV/m) results from the decay of the poloidal velocity, which has already been observed to correlate with the electron temperature pedestal height, see Fig. 4-14. The diamagnetic component to E_r is also observed to decay and this behavior is less clear since the edge pressure is actually increasing during ELM-free H-modes. The diamagnetic term can be re-written in terms of the temperature and density inverse gradient scale lengths

$$\frac{1}{Zen_i}\nabla P_i = \frac{T_i}{Ze}\left[L_{n_i}^{-1} + L_{T_i}^{-1}\right]. \tag{5.4}$$

As noted in section 4.3, in ELM-free H-modes the boron inverse gradient scale length does not vary significantly despite the factor of 4 increase in the overall density pedestal height. The inverse temperature gradient scale length, however, decreases by a factor of two over the H-mode. From this it is clear that although the L_n^{-1} contribution is twice the L_T^{-1} contribution, the changes in E_r result from the edge temperature pedestal only.

The ELM-free H-mode results provide for some interesting observations. Within the paradigm of **ExB** shear suppression one would expect the reduction in cross field particle transport to be proportional to the level of **ExB** shear. However, in ELM-free

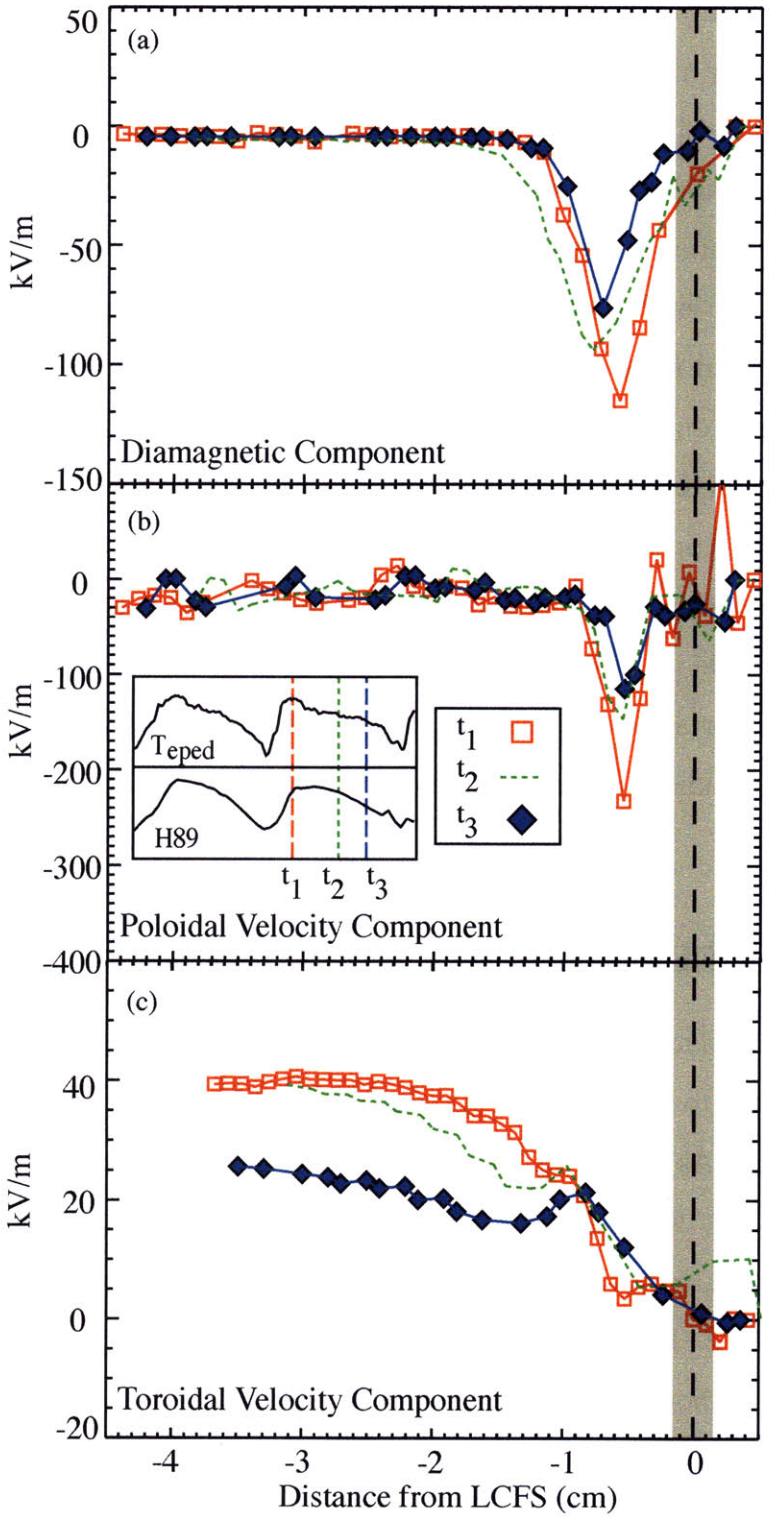

Figure 5-3: Individual B^{5+}component contributions to the total radial electric field profile in ELM-free H-modes (Shot=1070726014)

H-modes, the particle barrier is maintained over an order of magnitude variation in ω_s. There are a number of different explanations that are consistent with this observation. First, perhaps only a minimum level of shear is required to suppress particle transport and above that level the particle confinement is completely insensitive to E_r shear. Second, the relevant parameter to consider might be the cross-phase between the density and potential fluctuations, which, if out of phase, could prevent transport regardless of shear levels. And third, the mechanism controlling particle confinement could be decoupled from E_r altogether. Unfortunately, there is insufficient data to confirm or refute any of these hypotheses. In ELM-free H-modes the **ExB** shear correlates with the edge energy barrier and plasma confinement. This is consistent with **ExB** shear suppression. However, in this case the changes in the **ExB** shear are the *result* of changes in plasma confinement (via radiation) rather than the cause. As the impurities build up in ELM-free H-modes they increase the core radiation. When the radiated power approaches the input power the plasma begins to cool, reducing the height and gradient of the edge temperature barrier and as a result the E_r well depth and shear.

5.3.2 E_r in EDA H-Modes

Radial electric field measurements are more abundant in EDA H-modes than in ELM-free H-modes due to the relative ease with which CXRS measurements can be made in these plasmas. As a result EDA H-modes provide the opportunity to obtain some statistics on the E_r well structure. In EDA H-modes the radial electric field forms a deep negative well, relative to its L-mode values, the center of which is within 10mm inside of the LCFS. The E_r well width is consistently 5mm $\pm$ 1.5mm and on average -75kV/m deep, although wells as shallow as -30kV/m and as deep as -120kV/m deep have been observed in EDA H-mode discharges. At smaller minor radii the radial electric field is always positive and exhibits a smooth, slowly varying profile. Fig. 5-4A illustrates the general characteristics. Although variation in the E_r well depth has been observed on a shot to shot basis, the depth of the well in a given EDA H-mode remains constant as a function of time (provided the confinement is also

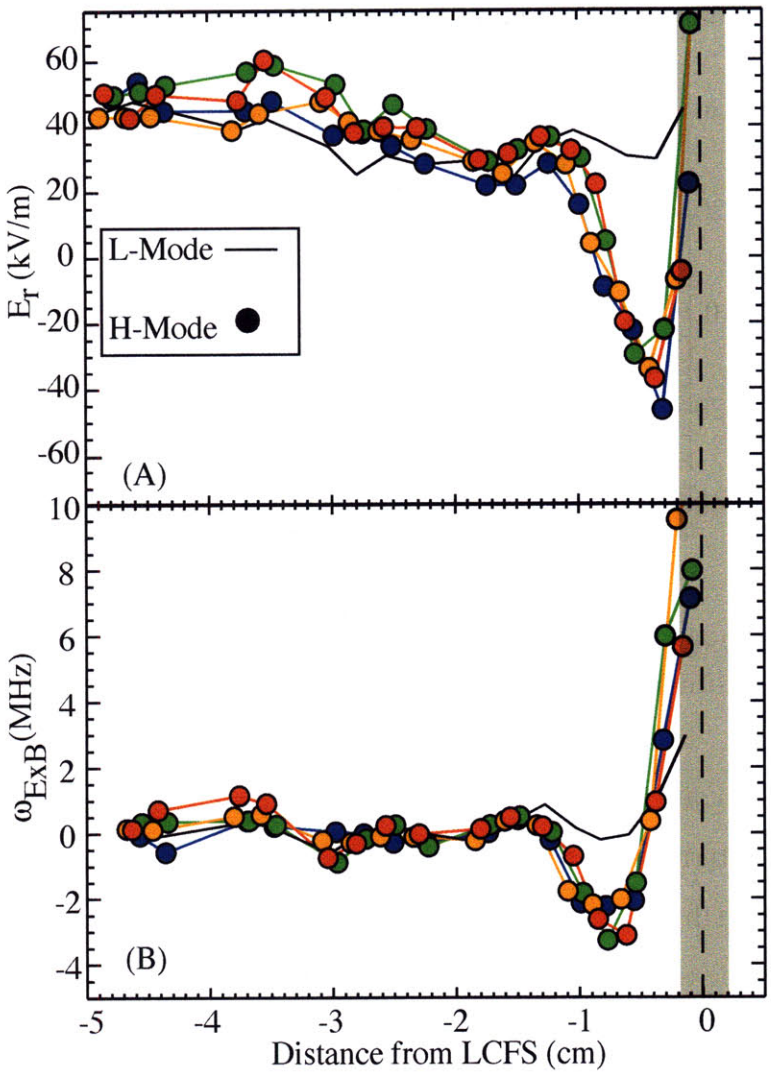

Figure 5-4: Radial electric field and **ExB** shear profiles in EDA H-mode plasmas (Shot=1080321020)

constant). In Fig. 5-4A E_r profiles from several different time slices within a single EDA H-mode are plotted together to illustrate the temporal constancy of the profile. The typical EDA E_r well yields an **ExB** shearing rate of order -3x10^{6}Hz. This also remains constant as a function of time as shown in Fig. 5-4B.

Generally, the relative contributions to the E_r well from the three components in Eq. 5.2 are similar from one EDA discharge to another. Fig. 5-5 displays an example of the various component profiles, which are qualitatively very similar to what is seen in ELM-free H-modes. The toroidal velocity contribution acts as a fixed positive offset to E_r, while the well itself is determined primarily by the poloidal velocity

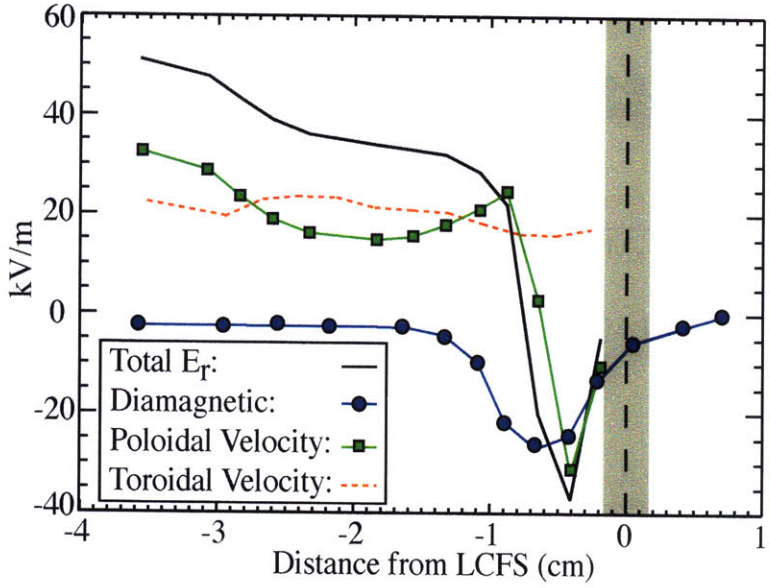

Figure 5-5: Individual B^{5+}component contributions to the total radial electric field profile in EDA H-modes

and diamagnetic contributions. The E_r well contributions from the diamagnetic and poloidal velocity terms tend to align well in location leading to an additive well depth. The E_r well depth due to the poloidal velocity profile is typically greater than that due to the diamagnetic term and considerably narrower. As a result, the poloidal velocity contribution tends to set the E_r well width and the **ExB** shearing rate. Inside the pedestal region the positive radial electric field is contributed to by a combination of co-current toroidal rotation and slightly ion diamagnetic poloidal flow. These two contributions far outweigh the slightly negative contribution from the diamagnetic component. In the core of the plasma the radial electric field remains positive as a result of co-current toroidal rotation, which is by far the dominant contribution.

The BDT model provides an expression to test whether or not the **ExB** shear is sufficient to suppress the plasma turbulence (Eq. 2.5). Unfortunately, the necessary turbulence measurements to make this comparison are not available on C-Mod. However, it is possible to compare the **ExB** shear rate to the maximum growth rate, γ_{Max}, of the edge instabilities. Estimates of the growth rates in the C-Mod pedestal region were obtained from a stability analysis using GS2[148], a linear, electromagnetic, gyrokinetic stability code[149]. GS2 assumes that the local gradient scale length is much

greater than the gyro radius and that the size of the fluctuations are small. These conditions are not met in the C-Mod pedestal, however, these runs represent the best available estimates of the growth rates. The code was run using fully developed EDA H-mode temperature and density pedestal profiles and resulted in a maximum growth rate of order $5x10^5$Hz. This is similar in magnitude to the **ExB** shearing rates observed in EDA H-modes. One should note that it is the L-mode instabilities that are theoretically suppressed by **ExB** shear enabling the transition to H-mode, and that the growth rates of pressure driven instabilities in L-mode plasmas will be less than those calculated for fully developed H-mode pedestal profiles. However, after the transition the instabilities must remain suppressed if the plasma is to remain in H-mode. Therefore, the comparison of the H-mode instability growth rates to the H-mode **ExB** shear rate is appropriate. The comparison of ω_s to γ_{Max} is based on plasma simulations, which have shown complete turbulence suppression when the condition $\omega_s > \gamma_{Max}$ is met [150, 151]. However, this rule is only a general guideline as the actual amount of shear needed to suppress the turbulence in the simulations varied by a factor of two both above and below the maximum turbulence growth rate [2].

On C-Mod core radial electric field profiles are available from the Hirex-Sr diagnostic. If there is sufficient signal then these profiles can extend out to the edge of the plasma and overlap with the E_r profiles determined using the new CXRS system. This enables a consistency check between these two diagnostics as E_r must be continuous across the plasma. A complete (core to edge) E_r profile from an EDA H-mode discharge is shown in Fig. 5-6. This profile demonstrates the level of agreement between the core and edge data and also illustrates the deepness and narrowness of the edge E_r well. This comparison has only been made for a handful of discharge. However, in these plasmas the core and edge E_r profiles are observed to agree to within the error bars of the measurement.

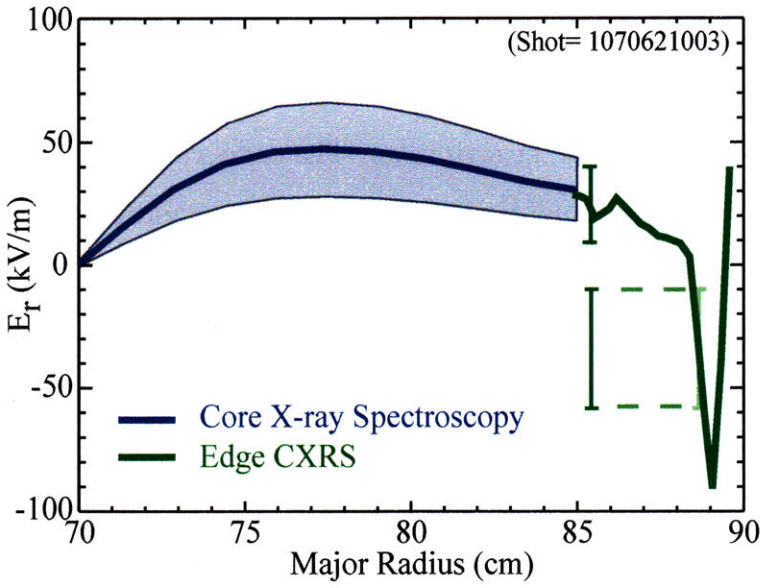

Figure 5-6: Full plasma radial electric field profile from combined core x-ray and edge CXRS diagnostics (shot=1070621003)

5.4 E_r in I-mode Plasmas

The radial electric field in I-mode plasmas is qualitatively similar to the profiles observed in the H-mode regimes, but smaller in magnitude as can be seen in Fig. 5-7. The I-mode E_r well is between 15 and 30 kV/m deep and forms at the edge of the plasma in the same region as the H-mode E_r well. The width of the well remains roughly 5mm leading to **ExB** shearing rates between 0.5 and 2MHz. This is less than typical EDA **ExB** shearing rates. In keeping with the **ExB** shear suppression theory, it is possible that in improved L-mode plasmas the level of **ExB** shear attained is approaching, but still less than, the critical value needed to make the transition to H-mode. As mentioned in chapter 4, I-mode plasmas can attain the same level of energy confinement as similar EDA H-modes and, as is clear from Fig. 5-7, they can do so with only half the edge E_r shear. This is suggestive of a critical shear requirement for the suppression of energy cross-field energy transport.

In I-mode plasmas all three components in Eq. (5.2) can contribute to the E_r well structure. This is different than in the H-mode plasmas, in which the toroidal velocity component acted as a fixed offset only. In I-mode plasmas, as discussed in section

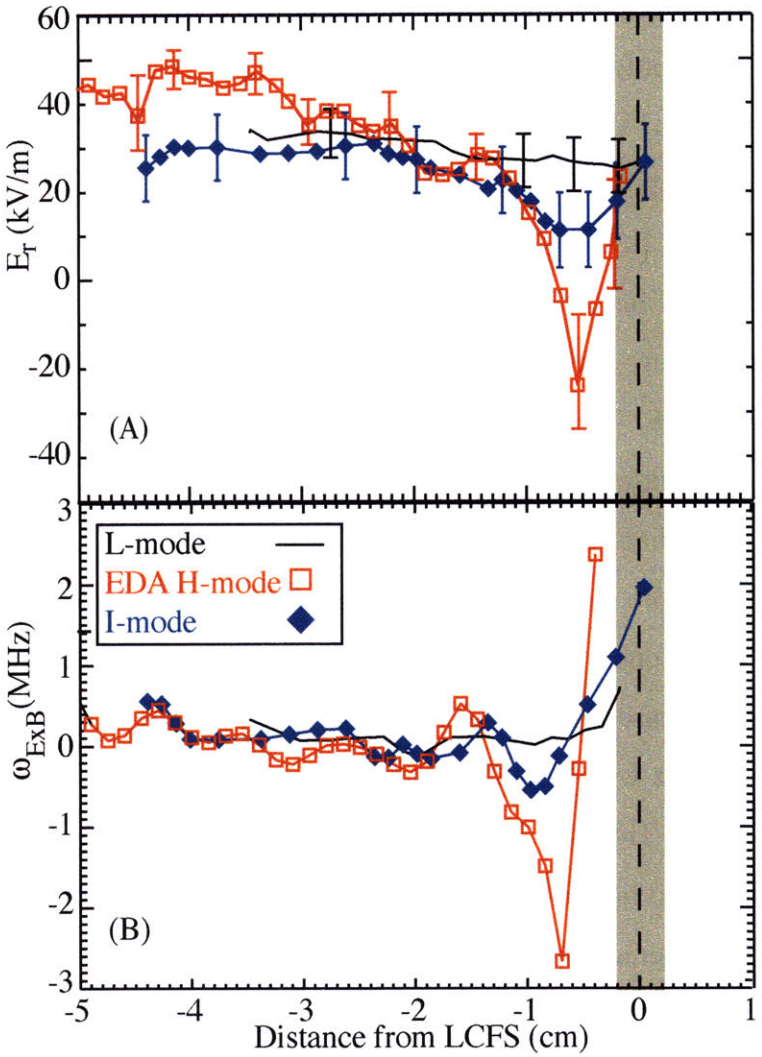

Figure 5-7: Comparison of radial electric field and **ExB** shear in EDA and I-mode plasmas

4.5, the toroidal velocity increases in the co-current direction after the application of ICRF, but is often observed to decrease in the counter-current direction prior to an I-H transition. In the first phase, the toroidal velocity behaves identically to its EDA H-mode counterpart. In the second phase, however, the counter-current decrease of the toroidal velocity at the edge can actually act to increase the **ExB** shear rate, perhaps helping to reach a critical transition point.

As I-modes have only been observed in discharges with the x-point in the unfavorable drift direction, this suggests that doing so alters edge conditions such that the particle and energy transport can be decoupled. The mechanism by which this happens is unknown. It is possible that operating in the unfavorable drift direction changes the dominant instability at the edge or alters the phase correlation between the density, temperature, and potential fluctuations [152] resulting in modified energy and particle transport. This could potentially occur as a result of changes in edge magnetic shear, SOL flows[8], or flows of the edge turbulent density fluctuations [153]. Alternatively, given that **ExB** shear is more effective at longer wavelengths, the observed I-mode transport could be explained if, in the unfavorable drift direction, the radial edge turbulent energy flux peaked at a higher poloidal wave number than the particle flux. In this case the same **ExB** shear would affect the two fluxes differently. It is also possible that I-mode is simply a phase through which every plasma passes on its way from L to H-mode regardless of topology, but in standard discharges it happens too quickly to be observed. In this case, something about the USN topology stabilizes this regime enabling it to exist steady state.

Chapter 6

Scalings of the H-mode E_r Well and Comparisons to Theory

The edge radial electric field is thought to play an important role in the dynamics of L-H transitions as well as in the sustainment of high confinement plasmas. As such, there are many theories that utilize E_r, or its shear, in their attempts to describe the physics that control these plasma regimes. As discussed in Chapter 2, some of these theories provide experimentally testable predictions for the structure of the edge radial electric field or at least scalings for the width of the H-mode E_r well (pedestal). In this chapter these predictions will be examined in light of the new C-Mod E_r data to see if they are consistent with the experimental observations. In addition, the structure of the E_r well will be explored as a function of plasma confinement and pedestal parameters and will also be used to infer information about the main ion population.

6.1 Scaling of E_r Well Width

Most of the theoretical works discussed in chapter 2 do not provide expressions for the full structure of the E_r well. Rather, they provide scalings for the pedestal width as a function of plasma parameters. A summary of the experimentally testable predictions discussed in chapter two is given in table 2.6.5. The width of the C-Mod E_r well in

EDA H-modes has been examined with respect to the different scalings listed in that table and the results of those comparisons are shown in Fig. 6-1. The measured width of the E_r well on C-Mod does not scale with any of the predictions outside of the uncertainty in the measurement. In fact, the width of the well shows very little variation in general. The full width half max (FWHM) of the well is on average 0.5cm with a standard deviation of 0.1cm. This is consistent with prior electron pedestal scaling studies on C-Mod, which found very little variation in the pedestal width over a wide range of plasma parameters [5]. Data points from ELM-free H-modes were not included in the study presented here due to the difficulty in obtaining accurate measurements of the FWHM of the well in those plasmas. However, in the ELM-free H-modes for which the full E_r profile was successfully determined, the well width was never observed to be greater than 5mm $\pm$1-2mm and so the inclusion of this data will likely not alter the results shown in Fig. 6-1.

Shaing and Crume proposed that the E_r well formed as a result of ion orbit loss at the edge of the plasma and that the width of the well should scale as the ion thermal velocity over the square root of the E_r shear (Eq. 2.10). It should be noted that this scaling is somewhat circular as the width and shear of the radial electric field are intimately connected. The radial electric field shear in the pedestal region changes dramatically as a function of radius. Thus to test this theory consistently across many C-Mod E_r profiles it was necessary to choose a fixed point on the E_r profile at which to make the comparison. The point of maximum E_r shear was chosen for this purpose and the ion thermal velocity was calculated at the same radial location. The results of this analysis are shown in Fig. 6-1 A; No correlation was found for the range of data available. In ELM-free H-modes very high shearing rates (10 times larger than in EDA H-modes) have been observed concomitant with 4-5mm FWHM E_r wells, which also does not support the scaling. However, if the E_r well widths were less than 3-4mm it would be below the ability of the diagnostic to discern.

Several different theories, including neutral penetration (Eq. 2.18) and pressure gradient models (Sec. 2.3.2), suggest that the E_r well width ought to scale inversely with the height of the edge density pedestal. This prediction has been examined

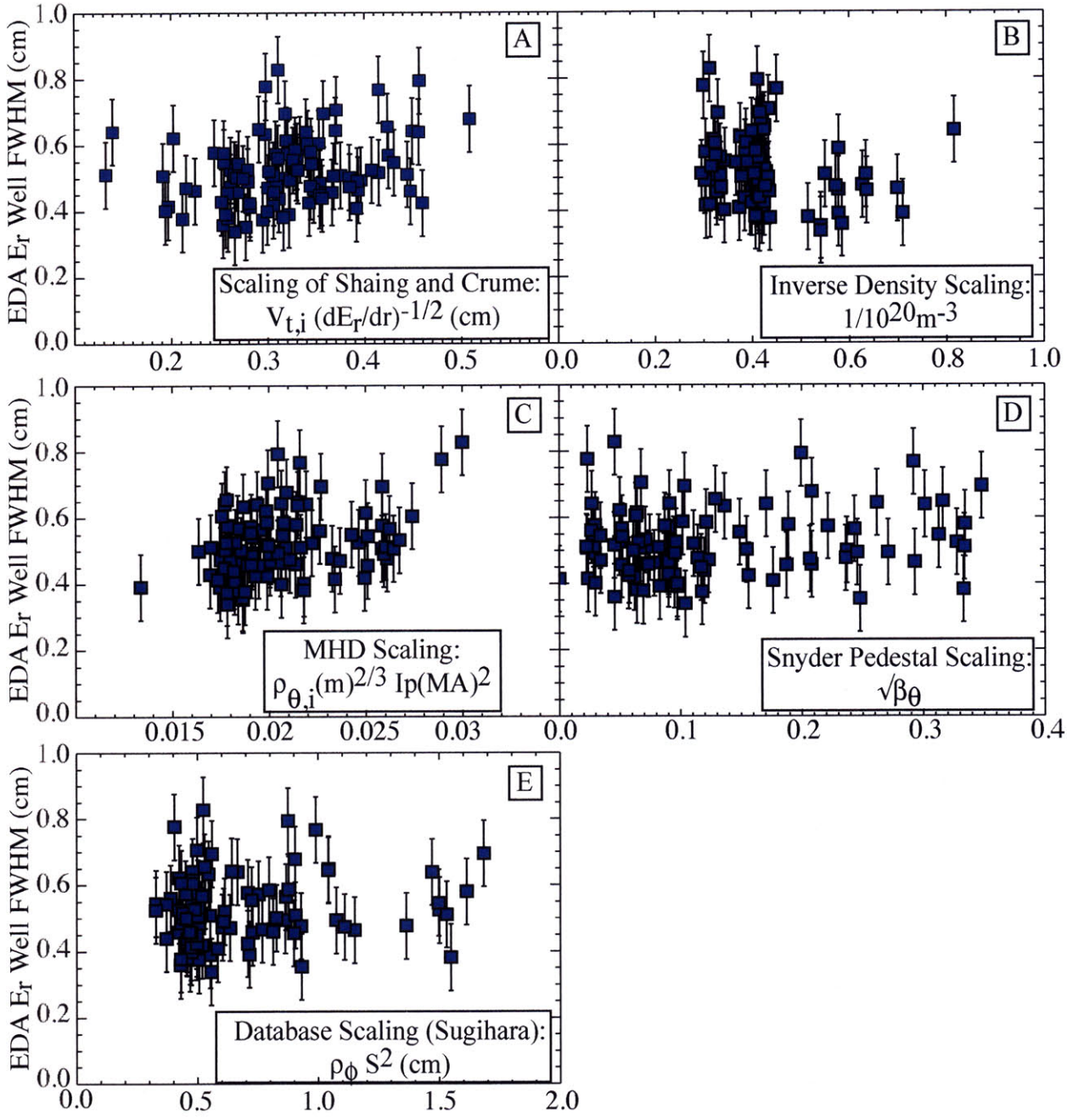

Figure 6-1: Scaling of E_r well width with the theoretical predictions discussed in chapter 2.

for a range of pedestal densities between 1 and 3.5e20 m^{-3} (6-1 B) and again no correlation with measured E_r well width was found. Width predictions have also been obtained by considering pedestal stability with respect to pressure and current driven instabilities (sec. 2.4). These have resulted in a number of different scalings including $\rho_{\theta_i} I_p^2$, $\sqrt{\beta_\theta}$, and $\rho_{\phi,i} S^2$. The relationships of the E_r well width to these parameters are shown in panels C-E of Fig. 6-1 and also yield no clear correlation for the range of data available. The MHD scaling ($\rho_{\theta_i} I_p^2$) was evaluated at the bottom of the E_r well (near the top of the T_e pedestal), while both the scaling in β_θ and magnetic shear were evaluated at the LCFS. The EFIT reported values of the magnetic shear at the LCFS were used in this analysis, which do not take into account the possible effects of bootstrap current on the shear profile.

The EDA H-mode database used for these comparisons does not include a wide range of plasma shapes, plasma currents (0.8 - 1MA) or pedestal temperatures (200-550eV). It is possible that with a larger data set more variation in the E_r well width could be obtained. However, this possibility is unlikely given that the electron pedestal width was found to be constant over a wide range of plasma parameters [5]. The available data suggests that the width of the E_r well on C-Mod is fixed within the uncertainty of the measurement, but without a broader range of plasma currents and shapes, potential scalings with the theoretical predictions can not be entirely ruled out. In addition, it should be noted that the measured E_r well widths have not been de-convolved from the instrumental width of the diagnostic's LOS (~3mm). If these widths add in quadrature then the actual width of the E_r well in EDA H-mode is closer to 4mm $\pm$1mm and the scatter in Fig. 6-1 could potentially be hiding millimeter level variation in the E_r well width. De-convolving the instrumental widths or obtaining higher resolution pedestal measurements would help clarify the results of these scaling analyses.

The E_r well width on C-Mod is significantly narrower than the widths observed on other (larger) devices. This suggests a potential scaling of E_r well width with machine size. As can be seen in Fig. 6-2, the published radial electric field structure data from several different devices [93, 92, 98, 100], with the exception of the JFT-2M

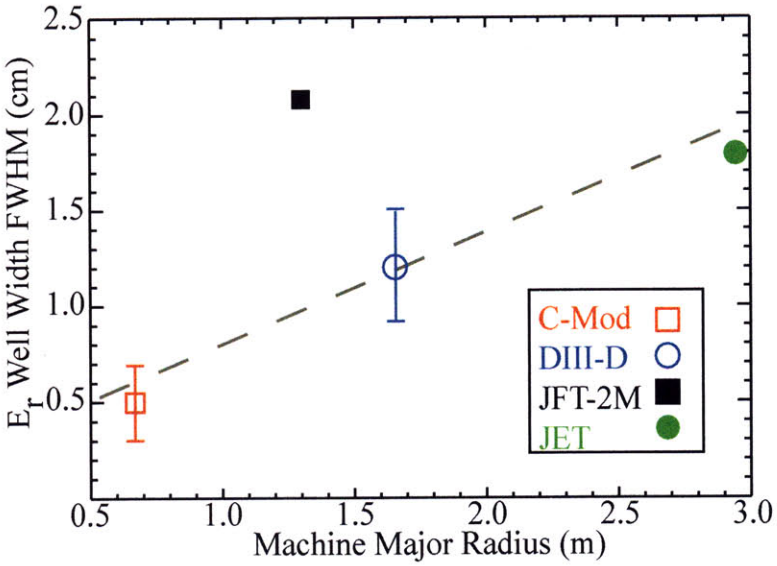

Figure 6-2: Width of the edge E_r well as a function of machine size.

data point, supports this supposition. These E_r well widths were obtained by fitting the data from these machines to a single Gaussian plus a polynomial background, which for the most part represented the data well. The JFT-2M data was not well represented by a single Gaussian. However, even by simple inspection the FWHM of this well is of order 2cm, which does not support the trend created by the other machines. The E_r well on JFT-2M was measured using a combination of passive and active spectroscopy from toroidally displaced diagnostics, which may have added considerable uncertainty to the measurement.

6.2 Scaling of E_r Well Depth

The relationship between the depth of the radial electric field well and plasma energy confinement has been explored and a clear correlation found between deeper H-mode radial electric field wells and higher energy confinement plasmas (H89). This correlation is shown in Fig. 6-3 and is in keeping with the paradigm of **ExB** shear suppression as the mechanism by which pedestals form and H-mode confinement is achieved. Within this framework deeper E_r wells provide stronger **ExB** shear, which gives an increased capacity for turbulence suppression, leading to higher pedestal

heights and improved plasma confinement, the latter due to 'stiff' core T_i profiles. In section 5.4 it was noted that I-mode plasmas can attain the same energy confinement as similar EDA H-modes, but do so with only half the edge **ExB** shear. This would seem to break the correlation between E_r well depth and energy confinement. However, as can be seen in Fig. 6-3 the I-mode observations (blue shaded region) do not affect the correlation, due to the large amount of scatter in the data. I-mode E_r profiles have only been determined for a handful of discharges and not for the highest H89 I-modes obtained. The blue shaded regions in figures 6-3 and 6-4 represent the range over which these profiles have been observed.

The correlation between the E_r well depth and plasma confinement is intriguing, but H89 is a global plasma variable and the physics of the H-mode would be better illuminated by a correlation between E_r and a local (pedestal) parameter. In Fig. 6-4 the depth of the E_r well is shown as a function of electron density (A), temperature (B), and pressure (C) at the top of the pedestal. E_r data has been obtained in H-mode discharges with peak pedestal densities between 1 and 3.5e20m^{-3}. Over that density range no scaling with density of the E_r well depth is observed in EDA H-modes and only a slight trend toward deeper E_r wells at lower pedestal densities is observed in the ELM-free H-mode data. The E_r wells from the I-mode plasmas do not overlap with any of the H-mode data as a function of plasma density.

In EDA H-modes only a limited range of pedestal temperatures (200-400eV) is accessible. This makes it difficult to see any scaling in the EDA data outside of the scatter. However, a much broader range of pedestal temperatures (200-1000eV) can be accessed in ELM-free H-modes. When this data is included in the analysis there is a clear correlation between the deeper E_r wells and higher pedestal temperatures. In Fig. 6-4 C the depth of the E_r well is shown as a function of the pressure at the top of the pedestal. Here, too, there is a correlation between higher pressure pedestals and deeper E_r wells, mainly as a result of the edge temperature. These results are also consistent with prior work on electron pedestal scalings in C-Mod. Although the electron pedestal widths are observed to remain fairly fixed regardless of plasma parameters or topology, the height and gradients of the electron pedestal are observed

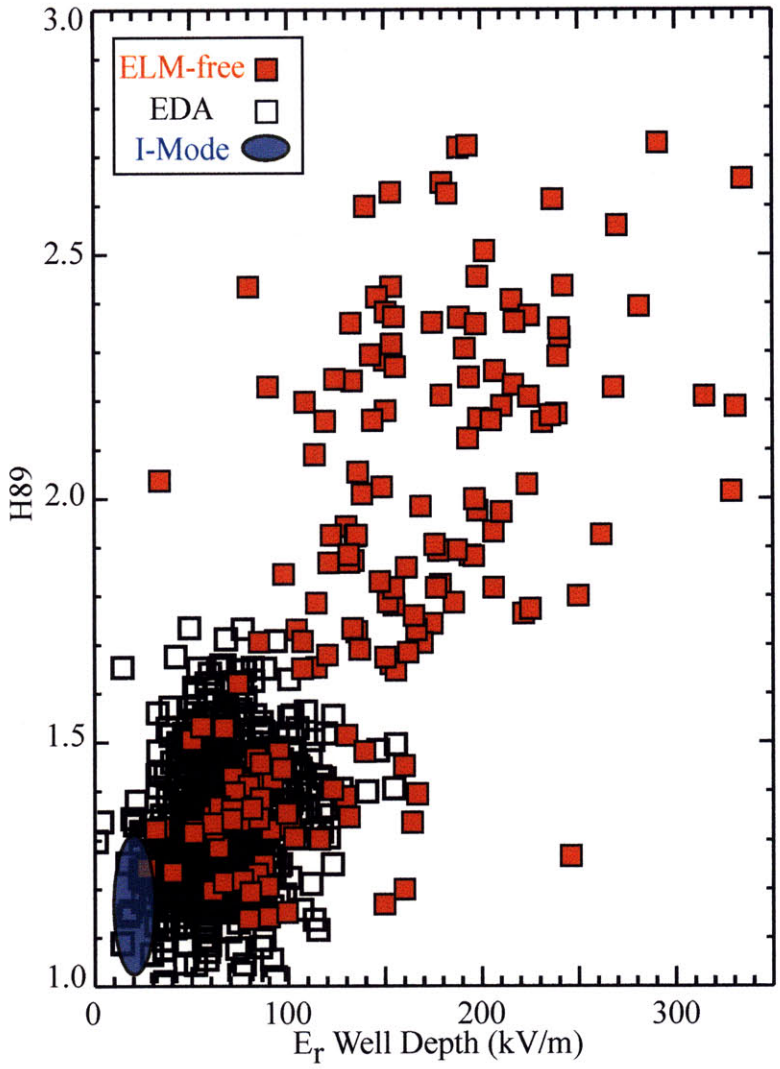

Figure 6-3: Correlation between E_r well depth and plasma confinement (H89) The red squares are from ELM-free H-mode discharges, the black squares are data points from EDA H-modes, and the blue shaded region indicates the range in which I-mode E_r wells have been observed.

to scale with plasma confinement [5].

6.3 Comparison to Neoclassical Theory

The results of section 6.2, namely, the correlation between deeper radial electric field wells and higher temperature and pressure pedestals, suggest that E_r theories that focus on these parameters should be compared to the experimental data. Neoclassical theory gives an expression for the gradient of the radial electric field in the Pfirsch-Schlüter regime that is primarily a function of temperature and pressure gradients (Eq. 2.21). This expression can be evaluated provided knowledge of the magnetic equilibrium, the ion and electron temperature and pressure profiles and a boundary condition for E_r, which is necessary to constrain the integration. On C-Mod all of this information is available with the exception of the main ion temperature and density profiles. However, based on the arguments made in section 4.1 both the boron and electron temperature profiles are good proxies for T_i and the main ion density profile can be estimated as $n_i = n_e - 5n_B$. Lastly, any point on the measured E_r profile can be used as the boundary condition for the integration.

Neoclassical theory is only valid on closed field lines, which means the calculated E_r profiles can only be compared to the measured data inside of the LCFS. In addition, the expression given in Eq. 2.21 is only valid in the Pfirsch-Schlüter (high collisionality) regime. Plasma collisionality is defined in terms of the ratio of the ion-electron collision frequency, ν_{ei} ($\sim n_i/T_e^{\frac{3}{2}}$), to the banana orbit bounce frequency, ω_b ($\sim \sqrt{v_{t,i}}$)). If a particle can complete a full banana orbit without experiencing a collision then the plasma is in a low collisionality regime, whereas if the particle collides then the plasma is said to be collisional. The collisionality parameter, ν^*, is defined by

$$\nu^* = \frac{\overline{\nu}_{ei}}{\omega_b \epsilon} \tag{6.1}$$

Here an additional factor of ϵ, the inverse aspect ratio, has been added in keeping with common practice. This form is popular because it gives the result that $\nu^* = 1$

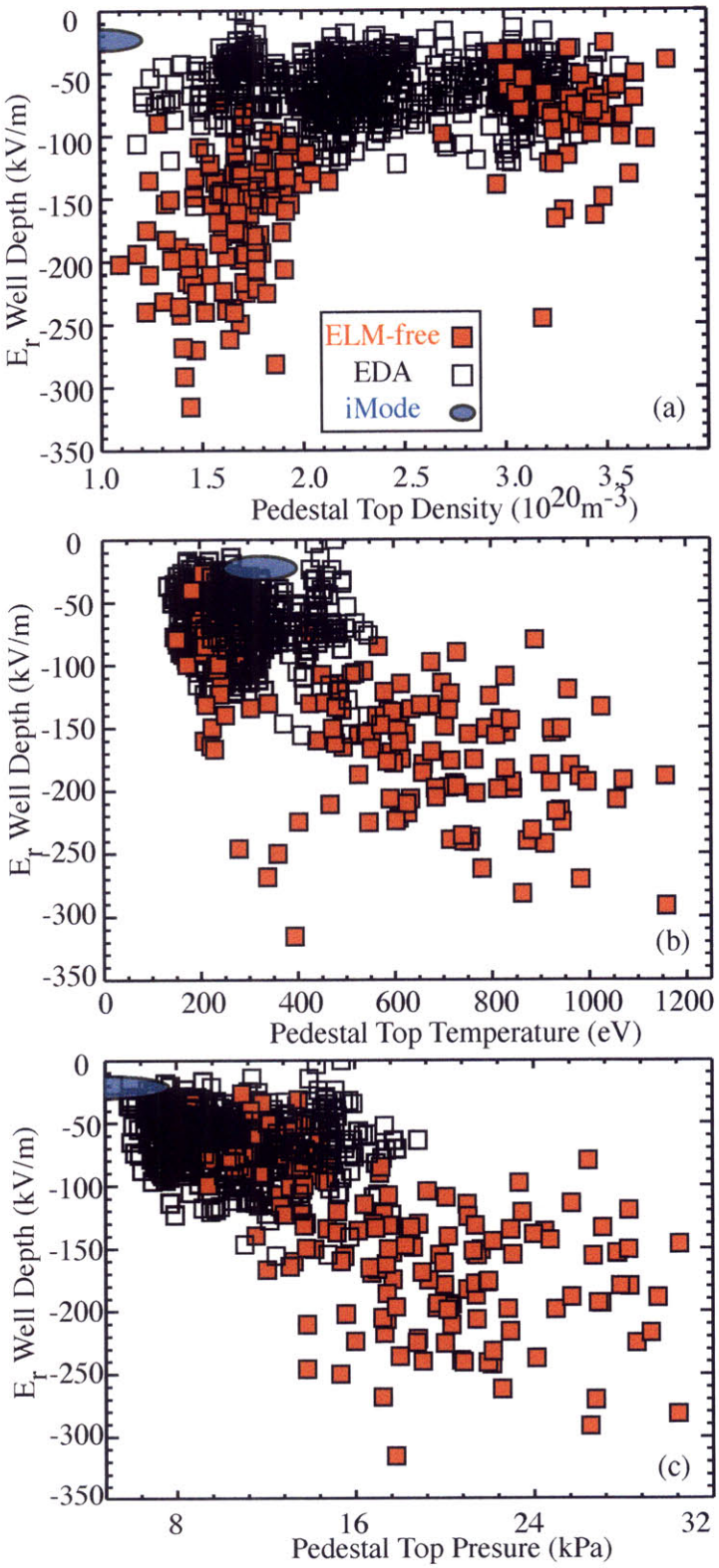

Figure 6-4: Depth of the radial electric field well versus electron pedestal parameters

marks the boundary between the plateau and the banana transport regime. By this definition the Pfirsch-Schlüter regime exists for $\nu^* > 5.3$. Profiles of ν^* from the four plasma operating regimes considered in this thesis are shown in Fig. 6-5. L-mode plasmas have the highest collisionality, followed closely by EDA-H-modes. I-mode plasmas, because of their low densities and elevated temperatures, are less collisional than both L-mode and EDA H-mode plasmas. The collisionality in ELM-free H-modes can vary significantly from shot to shot depending on the confinement obtained in each. In high energy confinement ELM-free H-mode discharges the collisionality can be very low enabling the banana regime to exist all the way out to the bottom of the pedestal. In lower confinement discharges, the collisionality can be very similar to EDA H-modes.

The dashed horizontal lines in Fig. 6-5 mark the boundary between the various neoclassical transport regimes. The regime of interest here (Pfirsch Schlüter) exists at the very edge of EDA and L-mode plasmas, and practically not at all in I-mode and ELM-free H-mode discharges. Therefore, a high collisionality EDA H-mode with good E_r profiles was selected to attempt the comparison to the neoclassically calculated E_r. This comparison will only be meaningful in a narrow band immediately inside of the LCFS.

To carry out the comparison between experiment and theory Eq. 2.21 was integrated using experimental temperature and density profiles as input parameters [154]. The profiles used for this purpose are shown in Fig. 6-6 A and B. The final comparison between the measured (red) and calculated E_r (green) profiles is shown in panel C [154]. The yellow highlighted area indicates the region in which the NC calculation is valid. For this calculation, T_i was assumed to be equal to T_e. However, the resultant E_r profile does not change significantly if T_i is instead chosen to equal T_B due to the similarity of the profiles. The boundary condition for this integration was chosen to match the measured and calculated values of E_r at the LCFS (i.e. the point at which the green and red curves cross). Altering this boundary condition does not change the shape of the calculated profile, only shifts its position along the vertical axis.

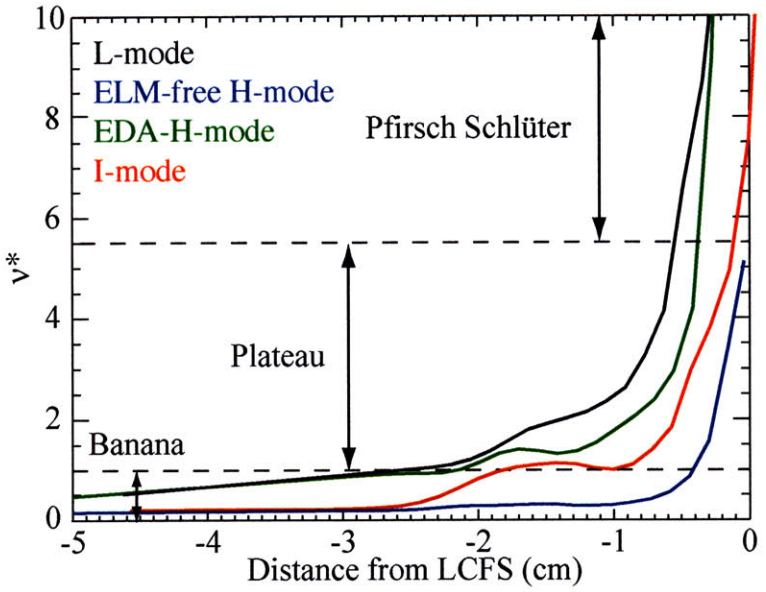

Figure 6-5: Radial profiles of ν^* from the four plasmas regimes considered in this thesis. The position of the LCFS for each discharge was determined using the power balance considerations discussed in section 4.1.1. (Shots = 1070627003 (L-mode), 1070621003 (EDA), 1070726014 (ELM-free), 1080415017 (I-mode))

There is no agreement between the measured E_r profiles and the NC calculation, not even in the region in which this comparison is suppose to be valid. Altering the boundary condition cannot improve the agreement, because the measured and calculated E_r profiles have opposite slopes in the Pfirsch-Schlüter regime. However, only a very few data points in the measured profiles are actually in the relevant regime and the temperature and pressure gradients are controlled by the profiles as a whole. Additionally, if at the edge either turbulence or the presence of neutrals is seriously effecting the transport of angular momentum then the expression used for the neoclassical electric field may not be applicable.

6.4 Comparison to Main Ions

Impurity ion profiles are employed to calculate E_r due to the relative ease with which they can be measured. However, the main ion population is the real species of interest as they control the plasma dynamics. Since the radial electric field is the same for all species, information about the main ion population can be inferred by comparing

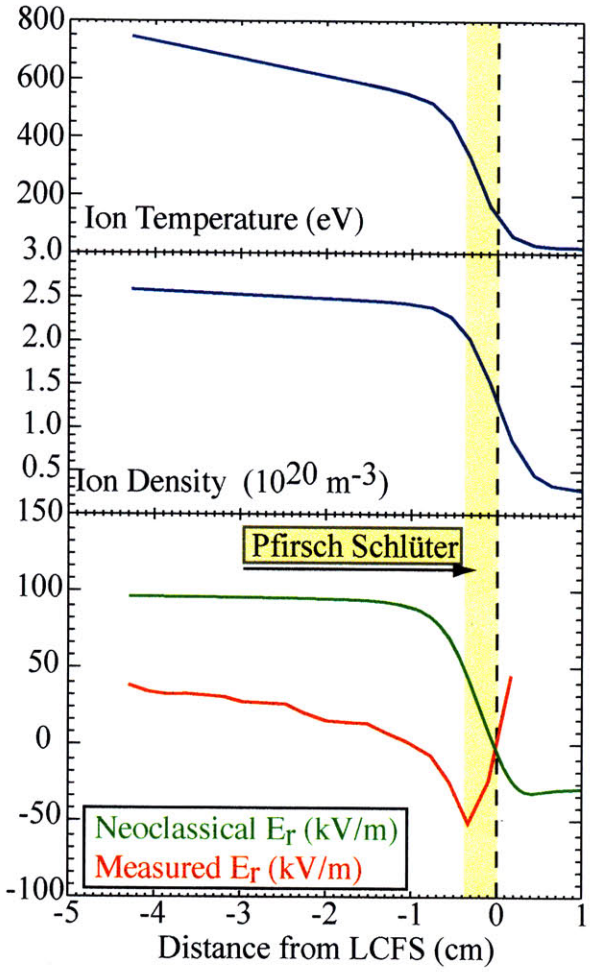

Figure 6-6: Comparison of a measured EDA E_r profile to the neoclassical calculation of E_r in the Pfirsch Schlüter regime. Panels A and B show the temperature and density profiles used to calculate E_r. Panel C shows the calculated (green) and measured (red) E_r profiles. The yellow highlighted area indicates the region in which the comparison is valid.

the total radial electric field to an estimate of the main ion diamagnetic contribution ($E_{\nabla P_i}$). This comparison can potentially yield information about the source or formation physics of the radial electric field as well as suggesting guidelines for creating self-consistent radial electric field profiles for modeling codes. Additionally, the difference between E_r and the main ion diamagnetic contribution provides a measure of the main ion flow perpendicular to the magnetic field, which is useful for comparing to theoretical predictions of main ion velocities.

As stated in section 6.3 and justified in chapter 4, either T_e or T_B can be used in place of T_i and n_i can be estimated from the electron and boron density profiles. From this $E_{\nabla P_i}$ can be estimated as

$$E_{\nabla P_i} = \frac{\nabla P_i}{n_i e} = \frac{\nabla \left(T_e(n_e - 5n_B)\right)}{(n_e - 5n_B)e}. \tag{6.2}$$

Fig. 6-7 shows a comparison between the total measured E_r profile and the main ion diamagnetic contribution in an EDA H-mode. Here the electric field has been averaged over the steady state portion of the H-mode to obtain a low noise, high resolution profile. The TS profiles used to calculate the main ion estimate were averaged over the same time period and pre-shifted to align the electron and boron temperature pedestals. The main ion diamagnetic estimate (blue) is remarkably similar to the total E_r profile (red) in shape, position, and depth, but is offset in magnitude by $\sim$ 30-40kV/m.

The similarities in shape indicate that the main ion pressure gradient is the dominant contributor to the radial electric field well in H-mode plasmas [155]. However, the offset in magnitude indicates that the main ions have some rotation perpendicular to the magnetic field in this region. This can be seen by rearranging Eqn.(5.2) and solving for the perpendicular velocity,

$$\vec{V}_{\perp i} = -\frac{\vec{B}}{B^2} \times \left(E_r - \frac{\nabla_r P_i}{n_i Z_i e}\right) \hat{r}. \tag{6.3}$$

From this the main ion perpendicular flow is inferred to be between -5 and -10km/s as shown in Fig. 6-8. One should note that the radial alignment of $E_{\nabla P_i}$

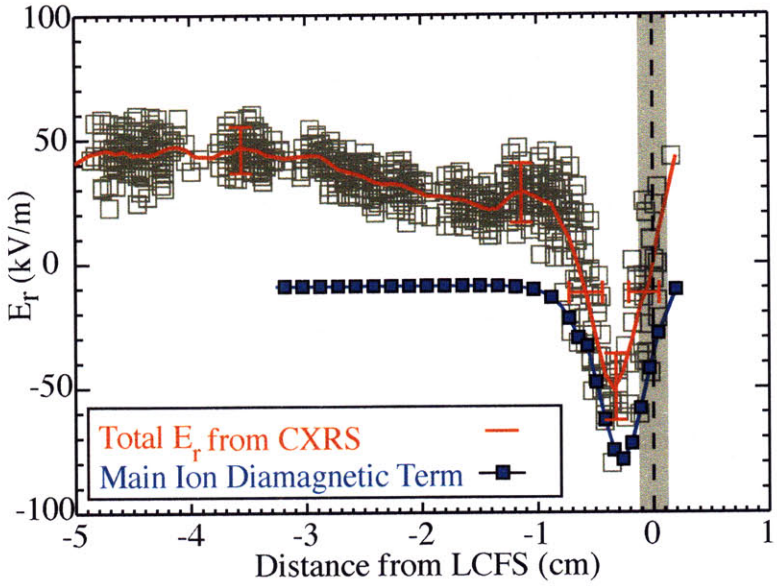

Figure 6-7: Comparison of the total E_r profile (red) averaged over the steady state portion of an EDA H-mode to an estimate of the main ion diamagnetic contribution to E_r (blue)

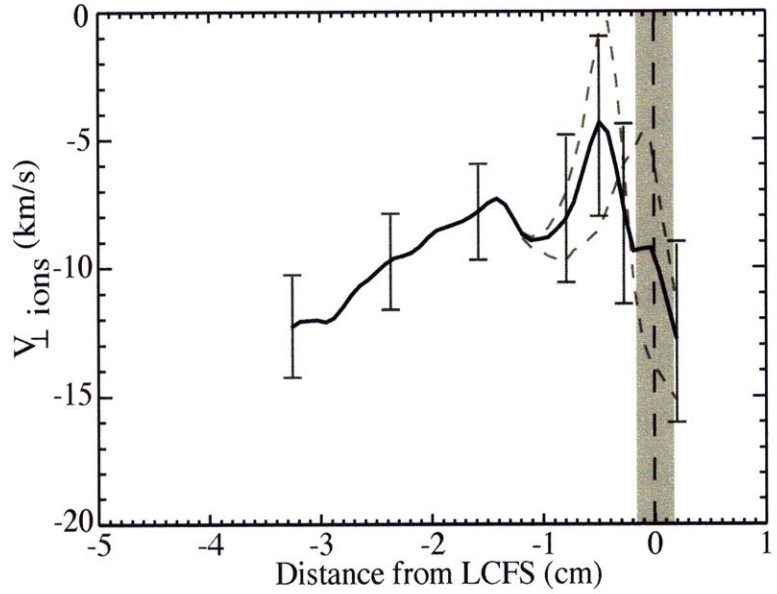

Figure 6-8: Main ion velocity perpendicular to the total magnetic field. The dashed lines indicate the changes to the velocity profile if the TS and CXRS radial calibrations are shifted by plus or minus 1mm.

with respect to E_r is subject to the rather arbitrary shift introduced to align the T_e and T_B profiles as well as to the radial uncertainties introduced when fitting the temperature and density profiles to tanh functions. These radial uncertainties are of order $\pm$ 2-3mm and can have dramatic effects upon the shape and magnitude of the inferred main ion perpendicular velocities. The dashed lines in Fig. 6-8 indicate the changes to the main ion perpendicular flow from a 1mm radial shift of the TS data in either direction. It is not possible to break down the main ion perpendicular rotation into toroidal and poloidal flows without making an assumption about the main ion flow parallel to the magnetic field.

The electron diamagnetic contribution to E_r can also be compared to the total field yielding information about the electron flow in the pedestal region. This comparison gives an electron perpendicular flow velocity of order 40km/s in the pedestal region. This is expected as the electrons must speed up to to satisfy $J \times B = \nabla P$ on a flux surface.

6.5 Alignment of E_r with Edge Electron Pedestals

The main ion diamagnetic contribution to E_r has been compared to the total radial electric field profile for several EDA H-modes from multiple run days. In all cases, the E_r well created by the main ion pressure gradient (from TS profiles) is similar in shape and depth to the total E_r field, but typically offset in magnitude and often slightly misaligned with the main ion diamagnetic contribution (1-2mm) outside of the total E_r well. The relative location of the E_r well with respect to the electron temperature and density pedestals as well as the location of the LCFS is dependent upon the shift of the TS data with respect to the CXRS data. This shift also affects the shape and magnitude of the inferred main ion perpendicular rotation profiles in the pedestal region. Inside the steep gradient region (at smaller major radii), the main ion rotation perpendicular to the magnetic field is consistently of order -10km/s.

Fig. 6-9 shows the alignment of the radial electric field to the electron pedestals and the LCFS for both shifted and unshifted profiles. If the TS profiles are left

unshifted then the main ion contribution to E_r is located outside the total E_r well by a half cm or more. This situation is shown in panels A-D. This alignment gives main ion perpendicular rotation at the LCFS of order -30km/s, which is implausible. Alternatively, if the TS profiles are radially shifted to align the T_e and T_B profiles, as discussed in section 4.1, then the diamagnetic contribution and the total E_r profile are usually brought into agreement within the error bars of the measurement, see Fig. 6-9 E-H. The resultant main ion rotation at the LCFS is reduced to -5 to -10 km/s. In this case the magnitude of the rotation is very dependent on the shape of the profiles in the SOL, the details of which are often not well captured by tanh fits to the data.

On C-Mod the electron density pedestal is typically narrower than the temperature pedestal and is located further outside by ~1mm [156]. When the TS profiles are shifted to align the T_e and T_B profiles the bottom of the E_r well aligns roughly with the strongest gradient location in both the electron temperature and pressure profiles, but is near the very top of the electron density pedestal (see Fig. 6-9 F - H). This means that the negative E_r shear exists in the middle to top of the energy barrier, while the density pedestal exists solely in the positive shear region. This is consistent with the previous observation that the E_r well depth correlates with the magnitudes of T_e and P_e at the pedestal top, but is independent of n_e. It is also reminiscent of the results from JFT2M, where the negative E_r shear was observed to correlate with the energy barrier and the bottom of the E_r well with the particle barrier [102]. Information on the relative location of the E_r shear with respect to the electron pedestals on other devices is, unfortunately, not available. However, on DIII-D at least the electron pedestals exhibit similar behavior to C-Mod; the electron density pedestal is typically narrower than the temperature pedestal and located further out radially [4].

The differences in radial alignment of the temperature and density barriers with respect to E_r and $\frac{dE}{dR}$ is potentially important as it may indicate the relevant physics controlling the formation and sustainment of the energy barrier versus the particle. Unfortunately, all of the profile alignment observations are subject to considerable

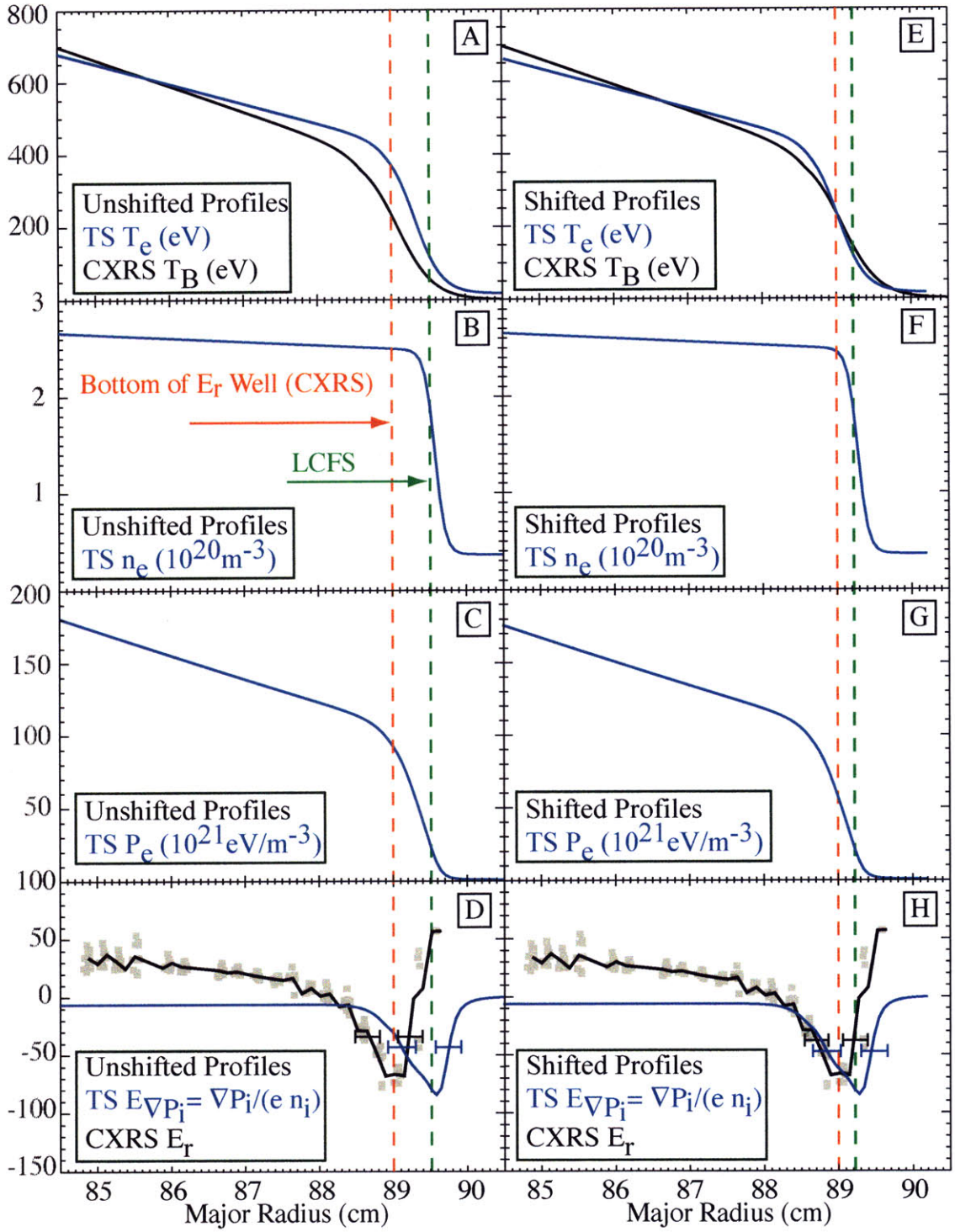

Figure 6-9: Radial alignment of E_r profiles with the electron pedestal parameters. In panels A-D the TS profiles have not been shifted from their EFIT reported positions. In panels E-H the TS profiles have been shifted by 2.5mm to align the maximum gradient region of the T_B and T_e profiles.

uncertainties in the relative locations of the TS electron profiles with respect to the CXRS measurements. Independent confirmation of the T_e profile alignment with T_B as well as a statistical analysis of the E_r well alignment is needed to substantiate these observations. The temperature profile alignment issue could potentially be resolved by running ohmic H-mode discharges and using the LFS scanning probes to make an additional measurement of the edge electron temperature profile.

Chapter 7

Summary and Directions for Future Work

The research described in this thesis has contributed to the characterization and understanding of the edge pedestal and its connections to particle and energy transport in fusion plasmas. Specifically, this work has focused on the role of the edge radial electric field and its shear in high confinement mode plasmas. It is well known that core plasma confinement is directly connected to, if not controlled by, the edge pedestal. A better understanding of pedestal physics and the interplay between E_r, turbulence suppression and pedestal formation should enable better control of edge transport and improve core confinement. This is especially important since future fusion devices, like ITER, will require H-mode confinement to meet their operational goals. The fundamental physics controlling edge transport remains elusive. However, through the dedicated efforts of the fusion community, both theoretical and experimental, a more complete picture is emerging. The new C-Mod CXRS diagnostic has enabled significant contributions to the study of pedestal physics to be made and many of these contributions have been highlighted in chapters 4-6 of this thesis. This chapter will summarize the key results presented in this work and will outline possible avenues for continued research.

7.1 High Resolution Pedestal Measurements

A new pedestal CXRS diagnostic has been designed, built, and implemented on the Alcator C-Mod tokamak. The C-Mod pedestal is very narrow, only between 2 and 6mm wide. This places a serious constraint on the spatial resolution of diagnostics attempting to measure plasmas parameters in this region. The edge CXRS diagnostic system is capable of measuring the pedestal characteristics utilizing both toroidal and poloidal views with 3mm radial resolution. To accomplish this the system's optics were designed to have 2mm spot-sizes at their focal points and the periscopes were positioned to make the LOS as tangent to magnetic flux surfaces as possible.

The spectra from the edge CXRS periscopes are analyzed by means of two fixed-grating Kaiser spectrometers coupled to two Photonmax charge coupled device cameras. The system is capable of handling up to 108 views and operates with 5ms integration time and a duty cycle of 6.4ms. This timing was found to be the fastest possible that still provided sufficient signal to make CXRS measurements in the pedestal region. However, with the installation of boron coated tiles in the diverter, the fractional boron density in the plasma may well increase, significantly improving CXRS signal levels and enabling faster integration times.

The data analysis for the CXRS diagnostic has been sufficiently developed to enable between shot analysis. However, there are still a number of improvements left to be done. The DNB attenuation code needs to be modified to include the effects of magnetic curvature and a detailed calculation of excited state fractions in the beam. Also, the passive fitting codes require improvement before the passive B^{4+} profiles can be inverted using tomographic techniques, and the active CXRS data analysis using the background poloidal periscope is not yet reliable.

7.2 Impurity Ion Pedestal Characteristics

The new CXRS diagnostic has enabled detailed pedestal measurements of the B^{5+} temperature, density and toroidal and poloidal velocity profiles to be made in a wide

variety of plasma regimes. The measured rotation profiles connect the SOL and core measurements and, as discussed in Ch. 4, are consistent with both. The L-mode flows, both toroidal and poloidal, exhibit a wealth of complex and intriguing behavior, only a small amount of which was presented in this thesis. The CXRS rotation measurements have also contributed to a variety of momentum transport studies and explorations of flow inversion phenomena [157] that were not included in this work. As plasma rotation and momentum transport are essential pieces to the plasma confinement puzzle, the CXRS diagnostic will continue to play an important role in these areas.

The measured boron temperature profiles from the toroidal and poloidal periscopes agree well in all of the plasma regimes considered indicating that the boron velocity distribution at the plasma edge is isotropic. The CXRS T_B profiles are observed to agree well with the TS T_e profiles in both shape and magnitude over a wide range of collisionalities. This is different from other machines, where the impurity ion temperature pedestal in H-mode plasmas is higher in magnitude than the electron pedestal and considerably less steep [4]. It is left as future work to explore further the agreement between the electron and impurity ion temperature profiles in C-Mod plasmas as a function of collisionality. This study would be especially enlightening if it were performed using matched discharges across multiple devices.

In H-mode plasmas the boron density is observed to increase by a factor of 10-40 above its L-mode values. This is indicative of the superior particle confinement in H-mode plasmas as compared to L-mode. The increase in boron density also means that CXRS measurements in H-mode plasmas are more abundant and more reliable than in L-mode. In H-modes both the boron temperature and density profiles form clear pedestals, similar to what is observed in the electron channel. The edge toroidal rotation increases in the co-current direction at the onset of H-mode confinement and the poloidal rotation in the pedestal region increases in the electron diamagnetic direction forming a narrow peak (3-4mm) just inside of the LCFS. Inside the pedestal region the poloidal rotation remains flat and small in magnitude.

The fast time resolution of the CXRS diagnostic enables the temporal evolution of

the edge parameters to be studied during L-H transitions. All of the edge parameters (T_B,n_B,$V_{B,\phi}$,$V_{B,\theta}$) are observed, within the resolution of the measurement (5ms), to begin their evolution at the same time. However, the typical time scales for them to complete their evolution and come to steady state values are different, see Fig. 4-12. The boron temperature and density pedestals form first, typically within 20ms after the L-H transition. This is consistent with the formation time for the electron temperature and density pedestals. The edge toroidal and poloidal velocity both require of order 50ms to reach an equilibrium and the core velocities don't come to a steady state until 130ms after the transition. This sequence of events does not identify an L-H transition "trigger". But, it does suggest that after the L-H transition the temperature and density pedestal evolution is the dominant mechanism driving the edge flows, which in turn then propagate into the core of the plasma. Most of the temporal evolution analysis shown in this work has made use of the passive B^{4+} profiles. Future work will include inverting the passive data to obtain localized B^{4+} profiles. Additionally, the data from the background poloidal periscope can be utilized to obtain active CXRS measurements of the temperature, density, and poloidal velocity during L-H transitions.

The change in the core toroidal rotation from L-mode to H-mode is observed to scale linearly with the change in the plasma stored energy and the height of the edge pedestal. The change in the edge toroidal rotation, inside of the pedestal, was examined with respect to this scaling and was found to remain constant regardless of the change in the pedestal height. This result is shown in Fig. 4-13 and implies that the momentum transport in the plasma is not purely diffusive; some additional mechanism for generating toroidal angular momentum must be present inside of the pedestal region. The change in the pedestal poloidal velocity was also examined as a function of plasma parameters and a correlation was found with the edge temperature pedestal height (Fig. 4-14). This is consistent with the idea that impurity ion flows are driven, in part, by main ion temperature gradients [142, 143, 144].

The CXRS diagnostic has been useful for studying I-mode plasmas. In this regime the boron density does not increase significantly above its L-mode values while the

boron temperature increases and forms an H-mode-like pedestal. The most interesting CXRS observations are in the toroidal and poloidal velocity behaviors. The edge poloidal velocity forms a small peak in the electron diamagnetic direction just inside of the LCFS. The peak is similar to the H-mode peak, but smaller and magnitude and potentially broader. The toroidal velocity increases in the co-current direction after the application of ICRF power, just as it does in H-mode plasmas, but prior to I-H transition, it decreases in the counter-current direction and has even been observed to change sign. The I-mode represents an intriguing regime for fusion research as particle and energy transport appear to be sufficiently decoupled that H-mode like energy confinement can exist without a strong particle barrier. Understanding the underlying physics controlling this behavior would be advantageous to developing reactor relevant plasma regimes and understanding pedestal physics.

7.3 Structure of the Edge Radial Electric Field and Comparisons to Theory

In this thesis the data from the new edge CXRS diagnostic was used to examine the structure of the edge radial electric field in a variety of plasma operating regimes. In Ohmic L-mode plasmas E_r is positive near the LCFS and becomes more negative with distance into the plasma. This is consistent with core observations of negative radial electric fields in L-mode plasmas. However, it is unclear whether or not the CXRS results are consistent with the LFS probe measurements of E_r. This is in part due to the complexity of the observations as a function of plasma density and magnetic topology and in part due to the uncertainty in the radial alignment of the measurements from these diagnostics. A more careful and detailed comparison between the probe measurements and the CXRS profiles is required to determine whether or not the two sets of data are consistent.

In H-mode plasmas the radial electric field is positive in the core, but forms a deep negative well, relative to its L-mode values, just inside of the LCFS. The well is

on average 5mm ±1mm wide (FWHM) and is dominated by the contributions from both the B^{5+} diamagnetic and poloidal velocity terms. These terms are typically of the same order, though the poloidal velocity contribution is usually the larger of the two and considerably narrower. As a result, the poloidal velocity contribution sets the width of the E_r well and the **ExB** shear rate. This is true in both EDA and ELM-free H-modes. In EDA H-modes the E_r well depth is on average 75kV/m deep although wells as shallow as 30kV/m and as deep as 120kV/m have also been observed. Typical **ExB** shear rates in EDA H-modes are of order -3×10^6Hz. In ELM-free H-modes the E_r well depth can be much deeper, up to 300kV/m, leading to an **ExB** shear rate of up to -2×10^7Hz. These results are qualitatively consistent with the observations made on other machines, see section 2.6. However, the C-Mod E_r wells are unprecedented in depth and the narrow C-Mod well widths, in comparison to results from other tokamaks, suggest a scaling with machine size as illustrated in Fig. 6-2.

There are a number of theories that give predictions for how the width of the E_r well ought to scale. These predictions are summarized in table 2.6.5 and were compared to the experimentally measured E_r well widths in Ch. 6, see Fig. 6-1. No significant variation of the E_r well width was observed with any of the predicted scalings. In fact, very little variation of the E_r well width is observed in general. This is consistent with prior pedestal width scaling studies done on C-Mod, which found very little variation in the pedestal width over a wide range of plasma parameters [5]. The results of the comparisons shown in Fig. 6-1 could be made more conclusive by expanding the scope of the E_r data-set to include a wider range of plasma currents and magnetic topologies (i.e. higher triangularity discharges) and by de-convolving the instrumental width from the measurement.

The structure of the edge radial electric field has also been compared to NC predictions in the PS regime, see Fig. 6-6. Here, again, no agreement between theory and experiment was found. The disagreement between the measured and calculated E_r profiles is potentially explained by the fact that the measured E_r profiles do not fully exist in the transport regime for which the the NC expression was derived.

Alternatively, if either turbulence or neutrals is effecting the transport of angular momentum at the edge, then the NC expression used for this comparison (see Eq. 2.21) may not apply. This comparison could be re-examined if E_r data was obtained in higher collisionality H-mode plasmas or if the effects of the edge neutral population on the NC predictions could be characterized.

7.4 Connections to Confinement and Transport

The physics that controls the suppression of edge turbulence and the formation of the edge energy and transport barriers is not well understood. However, clues to the underlying mechanisms can be found by studying the relationship between E_r, the edge pedestal height and plasma confinement. The depth of the radial electric field well, or alternatively the magnitude of the E_r shear (constant width), shows a strong correlation with improved plasma energy confinement, see Fig. 6-3. It also correlates well with the edge electron temperature and pressure pedestal heights (and gradients). It is not, however, very sensitive to variation in the edge electron density pedestal height. These results are shown in Fig. 6-4 and are an indication that the energy and particle transport have different relationships to E_r, with energy transport more directly linked to E_r.

The behavior of the radial electric field in ELM-free and I-mode plasmas supports this assertion. In ELM-free H-modes the depth of the E_r well is observed to correlate with the edge temperature pedestal and plasma energy confinement, but not with the edge density pedestal, see section 5.3.1. In fact, in these plasmas the height and gradient of the electron and impurity density pedestals continue to increase linearly even after the depth of the E_r well and the magnitude of the E_r shear begin to decay. In I-mode plasmas significant levels of **ExB** shear are observed concomitant with H-mode-like energy confinement, but L-mode-like particle confinement (section 5.4). These observations support a correlation between E_r and the edge energy barrier and suggest that there is a critical level of **ExB** shear required to suppress particle transport, but above that level the particle confinement is completely insensitive to

E_r and its shear. Alternatively, the relevant parameter to consider might not be E_r or its shear, but rather the cross-phase between the turbulent fluctuations which, if out of phase, could prevent transport regardless of shear levels.

Lastly, the position of the radial electric field well and its shear have been examined with respect to the location of the edge electron temperature and density pedestals, see section 6.5. The bottom of the E_r well aligns roughly with the strongest gradient location in both the electron temperature and pressure profiles, but is near the very top of the electron density pedestal. This means that the negative E_r shear exists in the middle to top of the energy barrier, while the density pedestal exists solely in the positive shear region. Similar results have been seen on other devices [102], which suggests that this feature may be a fundamental characteristic of tokamak H-mode pedestal structure. This result is potentially important as it may indicate the relevant physics controlling the formation and sustainment of the energy barrier versus the particle barrier.

Future work on this topic could include a statistical study of the alignment of the H-mode radial electric field profile and its shear with respect to the edge electron temperature and density profiles. This study would be especially meaningful if the information could be compared across multiple devices. Also, edge transport studies would benefit immensely from further study and characterization of I-mode plasmas. High time resolution measurements of E_r in these plasmas provide the means to address the question of whether or not there is a critical level of **ExB** shear that is required for the formation of an H-mode density pedestal. Lastly, measurements of the cross-phase of the turbulent fluctuations in the pedestal could give considerable insight into the physics of this region. On C-Mod this could be attempted by using edge scanning probes in Ohmic H-mode discharges.

Bibliography

[1] H. Biglari *et al.* Phys. Fluids B, 2:1, 1990.

[2] K. H. Burrell. Phys. Plasmas, 4:1499, 1999.

[3] M. Greenwald *et al.* Nucl. Fusion, 37:793, 1997.

[4] R. J. Groebner *et al.* Fusion Sci. Technol., 48:1011, 2005.

[5] J. W. Hughes *et al.* Fusion Sci. Technol., 51:317, 2007.

[6] J. E. Rice *et al.* Nucl. Fusion, 44:379, 2004.

[7] J. E. Rice *et al.* Plasma Phys. Control. Fusion, 50:124042, 2008.

[8] B. LaBombard *et al.* Nucl. Fusion, 44:1047, 2004.

[9] Y. B. Kim, *et al.* Phys. Fluids B, 3:384, 1991.

[10] N. P. Basse *et al.* Fusion Sci. Technol., 51:476–507, 2007.

[11] J. W. Hughes *et al.* Rev. of Sci. Instrum., 72:1107, 2001.

[12] L. Lau *et al.* Nucl. Fusion, 25:1611, 1985.

[13] J. E. Rice and E. S. Marmar. Rev. Sci. Instrum., 61:2573, 1990.

[14] A. Ince-Cushman *et al.* Rev. Sci. Instrum., 79:10E302, 2008.

[15] M. Greenwald *et al.* Plasma Phys. Control. Fusion, 42:A263–A269, 2000.

[16] M. Greenwald *et al.* Phys. Plasmas, 6:1943, 1999.

[17] M. Greenwald *et al.* Fusion Sci. Technol., 51:266, 2005.

[18] I. H. Hutchinson, *et al.* Plasma Phys. Control Fusion, 41:A609–A616, 1999.

[19] A. E. Hubbard *et al.* Phys. Plasmas, 14:056109, 2007.

[20] F. Ryter *et al.* Plasma Phys. Control. Fusion, 40:725, 1998.

[21] R. M. McDermott *et al.* Phys. Plasmas, 16:056103, 2009.

[22] F. Wagner *et al.* Phys. Rev. Lett., 49:1408, 1982.

[23] K. H. Burrell and the Doublet-III Operations and Neutral Beam Groups. Control. Fusion and Plasma Phys. (ECA, Linnich), 1:11, 1983.

[24] S. M. Kaye *et al.* Nucl. Matter, 121:115, 1984.

[25] T. Ohkawa, *et al.* Phys. Rev. Lett., 51:2101, 1983.

[26] F. Wagner *et al.* Phys. Rev. Lett., 53:1453, 1984.

[27] F. L. Hinton. Nucl. Fusion, 25:1457, 1985.

[28] F. Wagner *et al.* Nucl. Fusion, 25:1490, 1985.

[29] C. M. Bishop. Nucl. Fusion, 26:1063, 1986.

[30] N. Ohyabu *et al.* Nucl. Fusion, 26:593, 1986.

[31] T. S. Hahm and P. H. Diamond. Phys. Fluids, 30:133, 1987.

[32] K. C. Shaing. Phys. Fluids, 31:2249, 1988.

[33] K. C. Shaing *et al.* Comments on Plasma Phys. and Control. Fusion, 12:69, 1988.

[34] K. C. Shaing *et al.* Plasma Phys. and Control. Nucl. Fusion Research, 2:13, 1988.

[35] P. W. Terry. Rev. Mod. Phys., 72:109, 2000.

[36] T. Chiueh *et al.* Phys. Fluids B, 2:1, 1990.

[37] T. S. Hahm. Phys. Plasmas, 1:2940, 1994.

[38] T. S. Hahm and K. H. Burrell. Phys. Plasmas, 2:1648, 1995.

[39] A. S. Ware *et al.* Plasma Phys. Control. Fusion, 38:1343, 1996.

[40] B. A. Carreras. IEEE Transactions on Plasma Science, 25:1281, 1997.

[41] A. J. Wootton, *et al.* Phys. Fluids B, 2:2879, 1990.

[42] B. A. Carreras, *et al.* Phys. Plasmas, 2:2744, 1995.

[43] K. H. Burrell *et al.* Plasma Phys. Control. Fusion, 31:1649, 1989.

[44] R. J. Groebner *et al.* Phys. Rev. Lett., 64:3015, 1990.

[45] K. C. Shaing and E. C. Crume. Phys. Rev. Lett., 63:2369, 1989.

[46] K. C. Shaing *et al.* Phys. Fluids B, 2:1492, 1990.

[47] J. Kim *et al.* Plasma Phys. Control. Fusion, 36:A183–188, 1994.

[48] K. C. Shaing. Plasma Phys. Control. Fusion, 36:A75, 1994.

[49] R. R. Weynants, *et al.* Plasma Phys. Control. Fusion, 40:635–639, 1998.

[50] K. C. Shaing. Phys. Fluids B, 4:290, 1992.

[51] S. Itoh and K. Itoh. Phys. Rev. Lett., 60:2276, 1988.

[52] T. E. Stringer. Phys. Rev. Lett., 22:1770, 1969.

[53] A. B. Hassmam *et al.* Phys. Rev. Lett., 66:309, 1991.

[54] P. H. Diamond and Y. B. Kim. Phys. Fluids B, 3:1626, 1991.

[55] F. L. Hinton. Phys. Fluids B, 3:696, 1991.

[56] J. A. Snipes *et al.* Plasma Phys. Control. Fusion., 38:1127, 1996.

[57] H-Mode Database Working Group. Proc. 21st EPS Conference on Control. Fusion and Plasma Phys. (Montpellier), 18B Part 1:334, 1994.

[58] H. Weisen *et al.* Plasma Phys. Control. Fusion, 38(8):1137, 1996.

[59] S. J. Fielding *et al.* Plasma Phys. Control. Fusion, 38(8):1091, 1996.

[60] A. E. Hubbard *et al.* Phys. Plasmas, 8:2033, 2001.

[61] M. A. Malhov and P. H. Diamond. Phys. Plasmas, 15:122301, 2008.

[62] F. L. Hinton and G. M. Staebler. Phys. Fluids B, 5:1281, 1993.

[63] P. H. Diamond *et al.* Phys. Rev. Lett., 72:2565, 1994.

[64] B. A. Carreras *et al.* Plasma Phys. Control. Fusion, 36:A93, 1994.

[65] B. A. Carreras *et al.* Phys. Plasmas, 1:4014, 1994.

[66] B. A. Carreras *et al.* Phys. Plasmas, 2:2744, 1995.

[67] A. E. Hubbard. Plasma Phys. Control. Fusion, 42:A15, 2000.

[68] J. W. Hughes. PhD Thesis, Massachusetts Institute of Technology, Cambridge MA, 2005.

[69] J. W. Connor *et al.* Phys. Rev. Lett., 40(6):396–399, 1978.

[70] P. B. Snyder *et al.* IAEA Meeting Publications, 2008.

[71] M. Sugihara *et al.* Nucl. Fusion, 40:1743, 2000.

[72] R. J. Groebner *et al.* Phys. of Plasmas, 9:2134, 2002.

[73] M. A. Mahdavi *et al.* Phys. of Plasmas, 10:3984, 2003.

[74] F. L. Hinton and S. K. Wong. Phys. of Fluids, 28:3082, 1985.

[75] J. W. Connor *et al.* Plasma Phys. Control. Fusion, 29:919, 1987.

[76] P. J. Catto *et al.* Phys. of Fluids, 30:2784, 1987.

[77] P. Catto. Personal Communication, 2009.

[78] M. N. Rosenbluth *et al.* Plasma Phys. and Control. Nucl. Fusion Research, 1:495, 1971.

[79] R. D. Hazeltine. Phys. of Fluids, 17:961, 1974.

[80] H. A. Classen *et al.* Phys. of Plasmas, 7:3699, 2000.

[81] P. J. Catto and A. N. Simakov. Phys. of Plasmas, 12:012501, 2005.

[82] S. K. Wong and V. S. Chan. Phys. of Plasmas, 14:112505, 2007.

[83] S. K. Wong and V. S. Chan. Phys. of Plasmas, 12:092513, 2005.

[84] S. K. Wong and V. S. Chan. Phys. of Plasmas, 14:122501, 2007.

[85] R. J. Taylor *et al.* Phys. Rev. Lett., 63:2365, 1989.

[86] R. J. Groebner *et al.* Proceedings of the 16th European Conference on Control. Fusion and Plasma Phys., 1989.

[87] K. H. Burrell *et al.* Phys. Fluids B, 2:1405, 1990.

[88] R. J. Groebner *et al.* Rev. Sci. Instrum., 61:2920, 1990.

[89] R. J. Groebner. Phys. Fluids B, 5:2343, 1993.

[90] K. H. Burrell *et al.* Phys. of Plasmas, 1:1536, 1994.

[91] R. A. Moyer *et al.* Phys. of Plasmas, 2:2397, 1995.

[92] P. Gohil *et al.* Nucl. Fusion, 38:93, 1998.

[93] K. H. Burrell *et al.* Plasma Phys. Control. Fusion, 46:A165, 2004.

[94] A. R. Field *et al.* Nucl. Fusion, 32:1191, 1992.

[95] W. Herrmann, and the ASDEX Team. Rev. Sci. Instrum., 69:3165, 1998.

[96] W. Herrmann *et al.* Plasma Phys. Control. Fusion, 40:683, 1998.

[97] J. Schirmer *et al.* Nucl. Fusion, 46:S780, 2006.

[98] N. C. Hawkes *et al.* Plasma Phys. Control. Fusion, 38:1261, 1996.

[99] Y. Andrew *et al.* EPL, 83:15003, 2008.

[100] K. Ida *et al.* Phys. Rev. Lett., 65:1364, 1990.

[101] K. Ida, *et al.* Phys. Fluids B, 4:2552, 1992.

[102] K. Ida *et al.* Fusion Sci. Technol., 49:122, 2006.

[103] K. Ida *et al.* Plasma Phys. Control. Fusion, 45:1931, 2003.

[104] K. Ida *et al.* Plasma Phys. Control. Fusion, 36:A279, 1994.

[105] K. Ida *et al.* Phys. Plasmas, 1:116, 1994.

[106] T. Ido *et al.* Plasma Phys. Control. Fusion, 42:A309, 2000.

[107] Y. Miura *et al.* Nucl. Fusion, 41:973, 2001.

[108] T. Ido *et al.* Phys. Rev. Lett., 88:055006, 2002.

[109] Y. Miura, and the JFT-2M group. Nucl. Fusion, 37:175, 1997.

[110] R. C. Isler. Plasma Phys. Control. Fusion, 36:171–208, 1994.

[111] I. H. Hutchinson. Principles of Plasma Diagnostics Second Edition. Cambridge UniveRev. Sci. Instrum.ty Press, Cambridge, United Kingdom, 2002.

[112] R. C. Isler. Physical Review Letters, 38:1359, 1977.

[113] D. H. Sampson. J. Phys. B: At. Mol. Opt. Phys., 10:749, 1977.

[114] R. M. Pengelly and M. J. Seaton. MNRAS, 127:165, 1964.

[115] R. J. Fonck, *et al.* Physical Review A, 1984.

[116] Kaiser Optical Systems, Inc. Ann Arbar, MI. http://www.kosi.com.

[117] S. C. Barden. Volume-phase holographic gratings and their potential for astronomical applications. AURA and NSF.

[118] R. E. Bell. Review of Scientific Instruments, 75:4158–4161, 2004.

[119] Barr Associates Inc., Westford, MA. http:/www.barrassociates.com.

[120] K. Marr. Guide to the Alcator C-Mod CXRS diagnostic. Internal Document: PSFC,MIT, 2008.

[121] R. S. Granetz. Personal Communication, March 2009.

[122] I. O. Bespamyatnov *et al.* Rev. Sci. Instrum., 79:10F315, 1984.

[123] C. F. Barnett. Controlled Fusion Atomic Data Center, Oak Ridge, Tennessee 37831-6372, 1990.

[124] I. D. Williams *et al.* J. Phys. B: At. Mol. Phys., 15:1377–1389, 1982.

[125] S. Suzuki *et al.* Plasma Phys. Control. Fusion, 40:2097–2111, 1998.

[126] I. O. Bespamyatnov. Personal Communication, 2009.

[127] I. O. Bespamyatnov and W. L. Rowan. Rev. Sci. Instrum.., 77:10F123, 2006.

[128] I. H. Hutchinson. Plasma Phys. Control. Fusion, 44:71–82, 2002.

[129] D. J. Griffiths. Introduction to Quantum Mechanics. Prentice Hall Inc., Upper Saddle River, NJ 07458, 1995.

[130] A. Blom. JET Joint Undertaking Report JET-IR, 1999.

[131] A. Blom and C. Jupén. Plasma Phys. Control. Fusion, 44:1229–1241, 2002.

[132] J. D. Hey *et al.* Proc. 20th Eur. Phys. Soc. Conf. Control. Fusion and Plasma Phys., Lisbon, 17, 1993.

[133] A. Blom. Physica Scripta., Vol. T120:90–98, 2005.

[134] M. L. Reinke, 2009. Personal Communication.

[135] M. von Hellermann. Plasma Phys. Control. Fusion, 37:71–94, 1995.

[136] I. H. Hutchinson. Statistical uncertainties in line shift and width interpretation. Internal document: PSFC, MIT, 2005.

[137] http://www.psfc.mit.edu/~rachmcd/profile_align_procedure.jpg, 2009.

[138] S. Wukitch. Personal Communication, 2009.

[139] A. Ince-Cushman. PhD Thesis, Massachusetts Institute of Technology, Cambridge, MA, 2008.

[140] P. C. Stangeby. The Plasma Boundary of Magnetic Fusion Devices. Taylor and Francis Group, 270 Madison Ave NY, NY 1006, 2000.

[141] B. LaBombard. T_e at the separatrix in C-Mod. Internal Document: PSFC, MIT, 2000.

[142] Y. B. Kim *et al.* Phys. Fluids B, 3:2050, 1991.

[143] P. Helander. Phys. Plasmas, 8:4700, 2001.

[144] P. J. Catto and A. N. Simakov. Phys. Plasmas, 13:052507, 2006.

[145] T. Putterich *et al.* Phys. Rev. Lett., 102:025001, 2009.

[146] P. H. Diamond *et al.* Nucl. Fusion, 49:045002, 2009.

[147] K. Ida. Plasma Phys. Control. Fusion, 40:1429–1488, 1998.

[148] W. Dorland *et al.* Phys. Rev. Lett., 85:5579, 2000.

[149] H. Yuh *et al.* Stability analysis of C-Mod with gyrokinetic code GS2. American Physical Society, 42nd Annual Meeting of the APS Division of Plasma Physics, 2000.

[150] R. E. Waltz *et al.* Phys. Plasmas, 2:2408, 1995.

[151] R. E. Waltz *et al.* Phys. Plasmas, 1:2229, 1995.

[152] A. S. Ware *et al.* Plasma Phys. Control. Fusion, 38:1343–1347, 1996.

[153] C. Fenzi *et al.* Phys. of Plasmas, 12:062307, 2005.

[154] A. Simakov. Personal Communication, 2009.

[155] G. Kagan and P. J. Catto. Plasma Phys. Control. Fusion, 50:085010, 2008.

[156] J. W. Hughes *et al.* Phys. Plasmas, 9:3019, 2002.

[157] A. Bortolon *et al.* Phys. Rev. Lett., 97:235003, 2006.